Theory of terahertz intervalence band polaritons and antipolaritons.

FARAGAI, Inuwa Aliyu.

REFERENCE

THEORY OF TERAHERTZ INTERVALENCE BAND POLARITONS AND ANTIPOLARITONS

By

Inuwa Aliyu Faragai

A thesis Submitted in partial fulfilment of the requirement of

Sheffield Hallam University

for the Degree of Doctor of Philosophy

November 2014

CONTENTS

LIST OF TABLES

LIST OF FIGURES

Declaration

I hereby declare that this thesis is my own work and confirm that the work has not been previously submitted for the award of any qualification to any institution or any organization.

I hereby declare that part of the work in this thesis has been published in refereed scientific journals, conference proceedings and in book chapter(see list of author's publication)

Signature

Date

Dedication

All thanks be to God for giving me the ability to carry out this research work.

I dedicate this work to my late father

ACKNOWLEDGMENT

All thanks be to God for given me the ability to carry out this research work.

I would like to sincerely thank my supervisory team who worked greatly with me to ensure successful a completion of this work. My special thanks go to my director of studies Prof. M. F. Pereira, for his kind supervision, advice, criticisms and useful suggestions. My thanks also go to my second supervisor Dr. Ian Halliday. I would not forget Dr. Tim Spencer for his technical assistance.

My special regards go to the members of my family. First, I would like to thank my mother who scarified all her time to stay with my wife and children during my study period. Secondly, I have to thank my wife Zahra'u for her patience throughout this period and for taking care of our children. My appreciation also goes to all my brothers, sisters and my cousin (Baban Zainab) for their good gestures and support.

Thanks also to My Phd collogues: Nikita, Chijioke, Abubakar, madugu, Ma'aruf and others for their contributions in one way or the other.

THIS WORKS IS SPONSORED BY KANO STATE UNIVERSITY OF SCIENCE AND TECHNOLOGY WUDIL, KANO. NIGERIA. UNDER THE TETFUND INTERVENTION PROJECT.

I also acknowledge the work of COST ACTION/MP1204 for given us the opportunity to participate in the series of conferences and events they organised.

ABSTRACT

The work presented in this thesis is a theoretical investigation of the interaction of terahertz (THz) radiation with intersubband excitations in microcavities leading to THz polaritons and antipolaritons. The approach is based on the dielectric function formalism. The dielectric constant is derived from an optical susceptibility evaluated with Non Equilibrium Many Body Green's Functions (NEGF), which is then adjusted to a Lorentzian fit. Finally, the resulting expression is included in the wave equation describing the propagating electric field in the medium. This model is applied to $GaAs/Al_{0.3}Ga_{0.7}As$ multiple quantum wells embedded in a micro-cavity. The energy dispersion relations leading to THz polaritons and antipolaritons are obtained and investigated for different carrier densities and cavity configurations.

Recently, intersubband based THz polariton emitters and THz quantum cascade lasers are attracting major research interest due to their great importance in applications such as THz imaging, spectroscopy as well as in security control for detection of biological and hazardous materials and medical diagnosis. The coupling of THz radiation with intersubband transitions in semiconductor microcavities can lead to further tunability and improved quantum efficiency for THz devices. Here we propose a simple geometry and used a simplified modelling technique to investigate the interactions of transverse electric (TE-Mode) polarized THz cavity modes with intervalence band excitations. The model is applied to single and multiple transition problems and combinations of many body effects and scattering mechanism are included in the input dielectric constant.

LIST OF AUTHOR'S PUBLICATIONS/PRESENTATIONS

PUBLICATIONS

1. I A Faragai and M F Pereira, THz valence band polaritons and antipolaritons, Proc. SPIE 9199, Terahertz Emitters, Receivers, and Applications V, 91990H (September 5, 2014); DOI:10.1117/12.2061794.

2. I A Faragai and M F Pereira Jr, The relevance of dephasing in THz Valence band polariton dispersion relations, Optical and Quantum Electronics;Accept for Publication 2 July, (2014). DOI:10.1007/s11082-014-9982-3.

3. I A Faragai and M F Pereira, THz intervalence band antipolaritons, JOP: Conference Series **526** (2014). DOI:10.1088/1742-6596/526/1/012006

4. I A Faragai and M F Pereira, The relevance of dephasing in THz intervalence band antipolariton dispersion relations (2014). IEEE Xplore. DOI: 10.1109/ICTON.2014.6876654

5. I A Faragai and M F Pereira Jr, Intervalence THz Antipolaritons, NATO Science for Peace and Security Series B: Physics and Biophysics, Springer Publications, Book Chapter, (2014).

6. I A Faragai and M F Pereira, Interactions of valence band excitations and terahertz TE-polarized cavity modes, Opt. Quant. Electronics, Vol. 46 pp. 527-531, (2014). DOI:10.1007/s11082-013-9780-3.

7. M F Pereira Jr and I A Faragai, Coupling of THz radiations with intervalence band transitions in microcavities, OPTICS EXPRESS 3439 Vol. 22, Issue 3, pp. 3439-3446 (2014). DOI:10.1364/OE.22.003439.

8. M F Pereira and I A Faragai,THz intervalence Band Polaritons and Antipolaritons, ICTON 2013 Mo. B5.5, IEEE (2013).

PRESENTATIONS

1. M F Pereira and I A Faragai, many body effects in THz intersubband polariton, UK seconductor conference, Sheffield Hallam university, (2014). Poster presentation.

2. I A Faragai and M F Pereira, Intervalence bands transverse-electric mode THz polaritons/antipolaritons, UK Semiconductors conference, Sheffield Hallam university, (2013). Oral presentation.

3. I A Faragai and M F Pereira, Valence intersubband excitations coupled with TE-mode polarized THz radiations, PR13 International conference on photorefractive effects, materials and devices, 4-6 Sept. 2013. Winchester, UK. (Poster-presentations)

4. I A Faragai and M F Pereira, Interaction of Light and valence band excitations in semiconductor micro cavity at terahertz frequencies, International conference on THz and Mid Infrared Radiation and Applications to cancer Detection Using Laser Imaging, 10-11 October, 2013, Sheffield UK. (Poster-presentations)

CHAPTER 1
GENERAL INTRODUCTION AND MOTIVATION

1.1 Introduction

The interaction of light with material excitations has been extensively investigated for many years and continues to attract strong research interest. This study began in atomic physics [1] and molecules, and then later in semiconductor systems and lead to successful applications in photonics, optoelectronics and allows many physical phenomena to be investigated.

Depending on the system under consideration, photonic modes and the material excitations can resonantly interact and new eigenstates called polaritons are formed. Thus polaritons are the result of light-mater interaction having a dual character characterized by an anticrossing behaviour [2]. Example of polaritons include: exciton-polaritons(due to coupling of light and excitons), Phonon-polaritons (due to interaction of optics phonon and photons), surface plasmon polariton (due to coupling of surface plasmons and photons) and intersubband cavity polaritons (due to coupling of confined photonic modes and intersubband transitions in a microcavity).

The findings presented in this thesis, are based on an application of microscopic theories of the interaction of electromagnetic radiation, specifically the terahertz (THz) region, and intersubband excitations in semiconductor quantum wells embedded in a microcavity. Its well known that a microcavity can potentially alter the optical properties of a semiconductor structure such as; spontaneous emissions and/or absorptions of electrons, atoms, holes or related quasi-particles. This is because the increased confinement of the electromagnetic field drastically affects its density of states [3,4]. Furthermore, the concept of antipolaritons describes the coupling of radiation and intersubband transitions in an inverted (gain) medium [5,6].

Intersubband transitions have delivered remarkable applications. Photonic

devices such as quantum cascade Lasers (QCLs) [4, 7, 8], quantum well infrared detectors (QWIP) [9, 10] and terahertz polariton emitters [11, 12] are among the successful applications.

1.2 A review on relevance of studying intersubband transitions

Progress in the study of intersubband transitions in quantum confined structures such as: quantum wells, wires and dots has significantly changed the field of optoelectronics, where devices operating in the mid and far infrared regions have been demonstrated. Among the recent achievements is the implementation of THz quantum cascade lasers (THz QCLs), THz photodetectors and THz Polariton emitters. All these devices are based of quantum engineering of intersubband transitions. Below we review relevant previous works based on intersubband transition in the THz domain.

1.2.1 THz quantum cascade lasers

The THz QCls is a unipolar semiconductor laser which emits radiation in the THz region due to intersubband transitions. Thus, unlike the conventional interband lasers, which are bipolar and photon emission is achieved due to electron-hole pair recombinations, QCLs utilise electrons in the conduction band or holes in the valence band to achieve laser emission. The first mid-infrared QCls was demonstrated in 1994 by Jerome Faist [13] at Bell laboratories. Since then, interest in the field increases, and advance in its technology lead to the advent of THz semiconductor quantum cascade lasers [14–16]. Its an open controversy that THz QCLs is the only solid-state THz sources that can deliver average optical power output level far above a milliwatt which is essential for THz imaging, and deliver continuous wave (CW) operation for frequency stability desired in high resolution THz spectroscopic [14]. The first THz QCL has been demonstrated by Köhler et al in a cooperation between Scuola Normale, Pisa and Cambridge university [15].

A typical QCL has three regions of interest: the injector, the active and the collector regions. Of particular interest is the ability to control the wavelength of the emitted radiation by varying the quantum well width making up the superlattices. This is because the confined electronic or hole states in the conduction or valence bands depend on the dimension of the quantum wells. Figure 1.1 below shows a typical structure of conduction band THz quantum cascade laser [21]. Note however that, different design approaches have been reported [6-21] in the design of the active region in order to achieve population inversion, which is the key to laser emission.

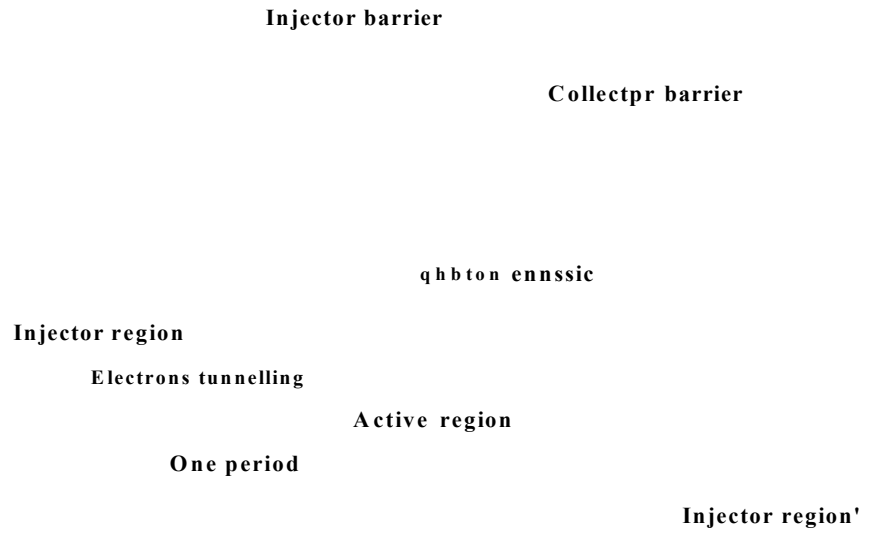

Figure 1.1: Schematic view of the conduction band diagram of four-level THz QCLs showing three regions of interest: the injector, the active and the collector regions based on the design described in REf. [21]

1.2.2 THz polariton emitters and quantum well photo detectors

Terahertz spectroscopy is based on the detection of THz radiation generated by a given source after it interacts with samples to be analysed. Recently new sources and detectors based on intersubband transitions have been developed, such as polariton emitters [11] and quantum well photodetectors. These device have strong potential for applications in spectroscopy, imaging and improved data transmission

in communications. Ultra-strong coupling of THz radiation with intersubband transitions which can further improve the applicability of polaritonic devices in an L-C resonator has been reported [24].

Furthermore, reflectivity experiments have demonstrated that THz intersubband polariton tuning is possible by electrical gating, in which the carrier density is modulated [12]. This increases the frequency range under which these devices can operate. Furthermore, different approaches have been considered to improve the efficiency and geometric designs for polaritonics, e.g. the use of optical couplers: surface-plasmon-polariton, micro-cavity coupler and 1D grating couplers [25]. This technique can increase the coupling strength as well as allowing coupling to normal incident THz radiation. In addition, beyond the usual GaAs structures, THz electroluminescence has been reported from THz QCL structures based on InAs/AlSb with a sharp spectral feature at 4.0 THz [26], widening the range of materials suitable for intersbubband THz applications.

1.3 The Electromagnetic spectrum and the Terahertz gap

The Terahertz (THz) gap refers to the range of the electromagnetic spectrum between microwave and infrared regions from 0.3 to 10 THz (1 THz = 10^{12} Hz . THz spectroscopy takes advantage of the fact that many substances undergo rotational and vibrational transitions in the terahertz to mid-infrared (TERA-MIR) frequencies. Therefore, THz can offer robust methods for controlling these individual transitions in a range of molecules, which are relevant for a large number of applications [27–31].

Several materials such as: plastics, papers and textiles show a reasonable optical transparency to the THz range of the electromagnetic spectrum. This is because they are non or less conducting and perhaps moist free thereby limiting the absorption of the radiation. Owing to this interesting quality, a number of industrial, medical and military applications can be offered. Chemical, biological, radiological or nuclear (CBRN) agents, explosives, and illegal drug substances, and

can be readily detected by merely sampling their characteristic absorption spectra at THz frequencies. In fact this is of particular interest in materials studies for enhanced quality assurance/material integrity and also in customs inspections and security in general. THz photons are not energetic enough to ionise molecules, and therefore can be harmless to living biological tissues. This characteristic advantage can be employed in medical diagnostics in humans, such as in the precise detection of tumours on the surface of human skin through THz imaging [32-35]. This is in contrast to conventional X-rays which are known to have long term harmful effects on humans upon exposure. Consequently THz radiation has a large potential for the diagnostics of diseases by breath analysis. It is also very interesting for satellite and spacecraft communication, since there is no absorption in space in contrast to the high absorption in the atmosphere due to water vapour. Figure 1.2 show the THz range in the electromagnetic spectrum.

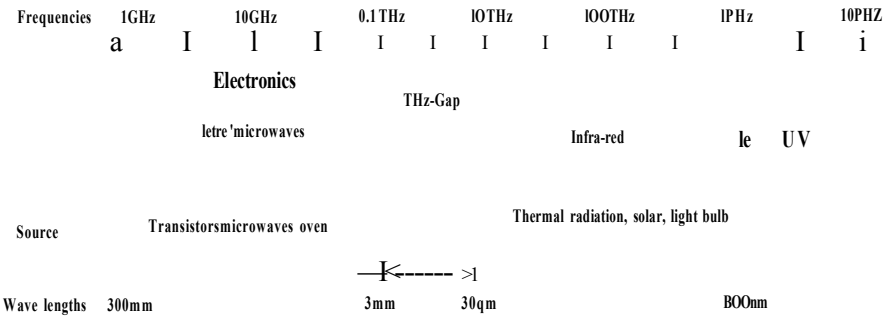

Figure 1.2: Schematic diagram indicating the THz gap filling the frequency range between Photonics and Electronics areas of application in the electromagnetic spectrum. Note: Not to scale

THz radiation is emitted from almost every object with tempereture around 10 Kelvin. However, THz emission at this temperature is very week [36]. There are many commercial and non-commercial sources of the THz radiation which include: optically pumped THz lasers, frequency mixers, semiconductor THz emitter and THz quantum cascade lasers (QCLs) [37,38]. Further details on terahertz and its applications can be found in literature [39,41,43-45].

1.3.1 Applications of Terahertz waves

We look below briefly on some fields where THz radiation is applicable:

1. THz Spectroscopy and Imaging

   Terahertz time domain spectroscopy (THz-TDs) has application in Chemistry and Biochemistry, security, imaging in medicine, communications as well as manufacturing processes [39–41]. The system involves directing subpicoseconds THz-pulses using an ultrashort near infrared pulsed laser at the surface of a sample to be analysed, and therefore becomes transmitted, reflected or absorbed after they interact. With the used of a second femtosecond laser pulse, the emitted radiation is then detected and analysed. THz radiation generates images of samples that are opaque in both visible and infra red regions. However, its application (in THz-TDs) is limited to very thin samples or samples with low absorbance. This is due to difficulty to distinguish the coherently generated THz pulses resulting from the samples and that caused by the driven lasers. The spectroscopic or imaging techniques of THz-radiation have the potential to improve the quality and uniformity of pharmaceutical products such as: 3D-chemical mapping [42], tablet coating and chemical fingerprint.

   The fact that THz-radiation can penetrate greatly into many materials such as polymers, clothing , fabrics, paper, cardboard, wood and so forth, makes THz-imaging to be more advantageous.

2. Security and safety

   Another fascinating application of terahertz technology is in advancing security and safety [46]. This is because THz penetrates through fabrics, wood and plastics materials. Thus, it is useful for surveillance, including security screening, to uncover concealed weapons on a person. These applications combined with THz Imaging Technology can potentially be used for societal safety such as in airport for passengers screening. Moreover, because THz radiation is non ionising, its low energy impacts has no harmful effects on human tissues and

organs, hence making it suitable to replace X-rays in medical imaging.

3. Telecommunications

   Because THz radiation has limited transmission in water, and the atmosphere contains a huge amount of water vapour, its uses in telecommunication for distance transmission is limited. However it can potentially be used in high altitude telecommunications i. e. above the altitude where large absorption of the radiation is less due to little concentration of moisture(e.g.in satellite communication). However, in recent research, wireless data transmission rate as fast as 3 Gigabits per second (twenty five times faster than the current standard Wi-Fi) is reportedly recorded using resonant tunnelling diode [47] to generate THz-waves, a proposal to be used as bandwidth for data transmission to enhance future telecommunication.

1.3.2 Maxwell's equations

The input to our model equations for the polariton and antipolariton problems is based on the dielectric formalism. To get insight into physical information contained in the optical responses of the system, $\epsilon(\omega)$, a review of propagation of electromagnetic wave in a non-conducting dielectric medium is in order. The basics to it is the wave equation which is derived from Maxwell's Equations. In the absence of free charges and current densities Maxwell's equations in free space have the form;

$$\begin{aligned} \nabla \cdot D &= 0 \\ \nabla \cdot B &= 0 \\ \nabla \times \mathbf{E}(r,t) &= -\frac{\partial \mathbf{B}(r,t)}{\partial t} \\ \nabla \times \mathbf{H}(r,t) &= \frac{\partial \mathbf{D}(r,t)}{\partial t} \end{aligned} \tag{1.1}$$

where $\mathbf{D}$ and $\mathbf{B}(r,t)$ are the electric and magnetic displacement fields vectors respectively. The electric displacement vector $\mathbf{D}$ is related to macroscopic optical polarization $\mathbf{P}$ according to $\mathbf{D} = \varepsilon_o \mathbf{E}(r,t) + \mathbf{P}(r,t)$. At optical frequencies and for a semiconductor material, the magnetic displacement, $\mathbf{B}$, become $\mathbf{B} = \mu_o \mathbf{H}(r,t)$.

Here ε_o and μ_o represent respectively the permittivity and permeability of free space.

1.4 Theories of polaritons and antipolaritons

Modern epitaxial growth techniques such as molecular beam epitaxy (MBE) used in the growth of a semiconductor crystal allow the confinement of electrons and holes in the crystal. In this process, quantum wells, wires and dots are created. Next, we briefly discuss polaritons in bulk and quantum wells, highlighting the main differences. This short discussion is meant to frame our work in the context of the large polariton field.

1.4.1 Exciton polaritons in bulk semiconductors

The valence and and conduction bands of a semiconductor are separated by an energy gap, E_g. At absolute zero temperature, the valence band in a semiconductor is completely full with electrons and the conduction band is empty. However, through optical pumping, electrons can be excited from ground state (zero level) in the valence band to excited states in the conduction band, thereby leaving behind a hole forming a bound state due to coulomb interaction. This electron-hole pair is called an exciton. In a bulk semiconductor, excitons can be strongly coupled with EM-radiation forming exciton-polaritons.

On the basics of semiclassical theory, the energy dispersion relation for the bulk polariton state can be derived from the combination of the wave equation and a classical Lorentzian optical dielectric function based on damped simple Harmonic oscillator model

$$\epsilon(\omega) = \varepsilon_o \left[1 + \omega_p \sum_{i,j} \frac{f_{i,j}}{\omega_{i,j} - \omega - 2i\gamma_{i,j}\omega} \right], \tag{1.2}$$

where $f_{i,j}$, is the oscillator strength due to the dipole interaction of interband transitions, $\gamma_{i,j}$ is a phenomenological damping constant, $\omega_{i,j}$ is the transition frequency between states i and j and $\omega_p = Ne^2/m_o\varepsilon_o$ is the plasma frequency (i.e. frequency at which the collective excitations respond rapidly with respect to a small change

in electric field). The letter N represents the number of free carriers (electrons or holes) per unit volume occupying a certain subband. The constants e, m_o, and ε_o stand for the charge, mass of electrons and vacuum dielectric constant respectively.

The dispersion relations for the exciton polariton can be derived as;

$$c^2k^2 = \omega^2\epsilon(\omega) \tag{1.3}$$

for transverse eigenmodes and correspondingly;

$$\epsilon(\omega) = 0 \tag{1.4}$$

for the longitudinal eigenmodes, where $\epsilon(\omega)$ is the optical dielectric function of bulk excitons without ionization continuum. For the transverse eigenmodes, using Equation 1.2 in Equation 1.3 and taking $\gamma = 0$ we obtain

$$k^2c^2 = \omega^2\varepsilon_o\left(\frac{\omega - \omega_{12} - \Delta_{LT}}{\omega - \omega_{12}}\right), \tag{1.5}$$

where $\Delta_{LT} = \omega_p f_{12}$ is called the longitudinal-transverse splitting. Equation 1.5 gives polariton without spatial dispersion and damping. However if the exciton energy is included by replacing the transition frequency $\omega_{12} = \omega_{12} + \hbar K^2/2M^*$ in Equation 1.5 and the effect of damping is considered as well, we obtain polariton with spatial dispersion and damping. Where M^* is the exciton effective mass. For details see for example [48]. In Figure 1.3 a schematic diagram for exciton polariton is depicted. The effect of damping will be discuss in details in the next chapters for the case of intesubband polariton and antipolariton. It will be shown that, significant damping make the polariton character to disappear, only photon's dispersion remained.

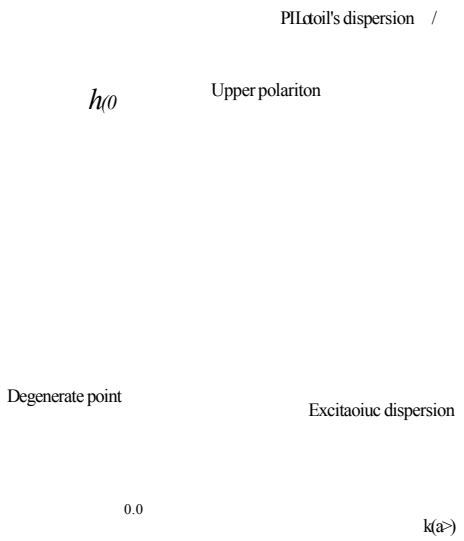

Figure 1.3: Schematic diagram of exciton polaritons in bulk material, indicating the long wavelength limit (dispersion approaches zero, as ft→ *0).*

1.4.2 Microcavity quantum well polaritons

In a quasi-two dimension structures such as quantum wells, the translational movement of both electrons and holes are restricted to two spatial directions. The effect of quantum confinement results in the formation of subband levels for either the conduction band or valence band as the quantum well thickness becomes comparable to the de Broglie wavelength. In a semiconductor, quantum wells are formed by sandwiching a semiconductor material with lower band gap between two layers of higher band gap semiconductor material. Figure 1.4 represents a schematic of GaAs quamtum well with AlGaAs as barrier.

The coupling strength of light-matter interaction can be enhanced if the photonic environment is modified. This can be achieved if the electromagnetic field is confined, analogous to quantum confinement of electrons in a quantum well structure. A semiconductor microcavity is an optical resonator through which light-matter interaction can be controlled. Reflectivity from microcavity resonators can also be achieved using a stack of photonic crystals with repeated alternate layers of

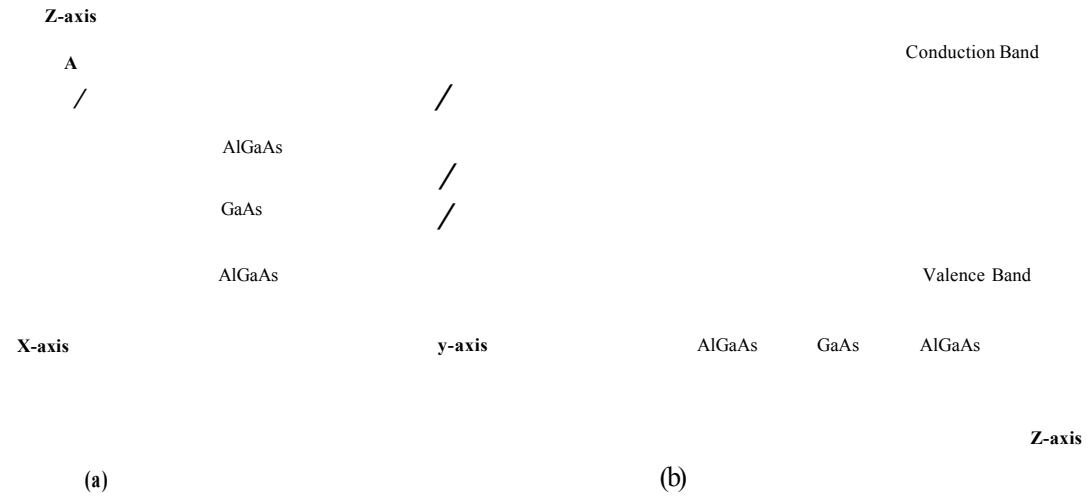

Figure 1-4-' Schematic (a) of GaAs/AlGaAs quantum well structure (b) band gap-diagram

two semiconductor materials having different refractive index, forming what is called a distributed Bragg reflector or simply between semiconductor-air interface due to total internal reflection. The cavity, typically a few microns in width, is designed to ensure that photonic modes in the crystal form a standing wave with their nodes at the center of the cavity. In order to achieve that, the cavity length should be an integral multiple of half the wavelength of the incident, $Lc = nX/2$, where n is an integer.

For a quantum well embedded in a microcavity, the polariton dispersion Eq. 1.3 for the transverse eigenmodes becomes modified due to the confined electric fields in the cavity and now reads:

$$c2 \quad {}^{,2}_{[c\|\| +} \quad {}^{*\ 2\ '}_{[\ ]} = uj2e\{oj)1 \qquad (1.6)$$

where $k\|\|$ is the wave number parallel to layer's growth direction and L stand for cavity length. Thus, in contrast to bulk polaritons, the dispersions for the microcavity have finite frequency in the long wavelength range (i.e as $kii \text{ — } >0$).

1.4.3 Intersubband cavity polaritons and antipolaritons

The coupling of cavity modes with intersubband excitations generates a new type of hybrid light-matter Hamiltonian. The experimental observation of intersubband polaritons was reported for the first time with reflection measurement [77] after the theoretical prediction by Asheng Liu in his paper titled 'Rabi splitting of the optical intersubband absorption line of multiple quantum wells inside a Fabry-Prot microcavity' [52]. The resultant energy dispersions in both two papers presented by the authors are based on the interaction of confined cavity modes and intersubband excitations in an absorbing media. Intersubband antipolaritons however, introduce new features due to amplified gain media (inverted media) [5,6]. Contrary to the case of polaritons, the two antipolaritons branches repelled each other. In the following chapter, analytical expressions for cavity intersubband polariton and antipolariton are derived and simple numerical calculations are also presented.

1.5 Aims and objectives

Most work on intersubband polaritons focuses on inter-conduction band transitions, with TM polarization. In this work we summarize our contributions to the field extending the study to polariton and antipolariton based on inter-valence band transitions with TE-polarization. The aims and objectives of the research include:

- To apply a dielectric model based on nonequilibrium Green Function (NEGF) to investigate the coupling of transverse electric (TE) modes polarized THz radiation and intervalence band transitions in $GaAs/Al_{0.3}Ga_{0.7}As$ multiple quantum wells embedded in microcavity.

- To explore simple geometrical designs for the cavity that allows coupling of inplane polarized cavity modes with the valence band excitations.

- Compare and contrast the relevance of valence band based design that allows the coupling with both TE and TM cavity modes.

1.6 Thesis outline

This thesis has the following structure. The first two chapters position the work in respect to the current state of the art of the field and introduce basics concepts required to understand the original work presented next, making this a self contained manuscript. Beside that, analytical expressions for the cavity polaritons and antipolaritons are derived and preliminary results from numerical approximations are presented.

In chapters 3 and 4, polariton and antipolariton dispersion relations for single and multiple resonances are derived. Numerical results are given for cavities containing $GaAs/Al_{0.3}Ga_{0.7}As$ multiple quantum wells . The influences of dephasing, changing cavity parameter and scattering mechanisms are all considered in these two chapters. Furthermore a comparison of results for TE and TM modes polaritons and antipolaritons closes the chapters. A general conclusion and future work are presented in chapter 5.

CHAPTER 2
BASICS OF INTERSUBBAND POLARITONS AND ANTIPOLARITONS

2.1 Introduction

The results shown in this manuscript are based on the dielectric approach. An analytical expression for the dielectric is obtained from a fit to the optical susceptibility obtained using nonequilibrium many body Green's function techniques. The energy dispersion relations for the polaritons/antipolaritons are derived analytically from the resulting expression for the dielectric constant and secular equation for the cavity modes. Full approaches are given in the later chapters.

In this chapter, analytical expressions of intersubband cavity polaritons and antipolaritons are derived and a simple numerical approach is also presented. However before that it is important to review some relevant optical processes related to intersubband transitions in quantum wells.

2.2 Optical transitions

In semiconductors and or quantum wells in particular, two different optical transitions occurs: Interband and intersubband optical transitions processes. The former can be direct or indirect process involving contribution of optical phonon, while the later is always a direct process. Both processes involves photons emission or absorption depending on which band or subband is excited. In the case of direct interband transition, both energy and crystal momentum are conserved ($k_\nu = k_c$). In other words, the transition occurs between valence and conduction bands states if both the momentum of the electrons and holes are the same in the Energy-momentum (E-K) diagram. For the case of indirect transition, the phonon wave number q has been included in conservation of the crystal momentum ($k_\nu = k_c \pm q$).

2.2.1 Interband transitions in quantum wells

In semiconductor quantum wells, optical transitions occur between valence and conduction bands due to photon emission or absorption. This are called interband or band to band transitions. Interband transitions can be direct transitions as shown in Figure 2.1 for direct band gap materials and in some cases it is an indirect transition involving contribution from optical phonon as it occurs in indirect band gap materials like silicon and germanium. Due to optical confinement of the electron and hole states in quantum well growth direction, restriction due to selection rule apply. Thus interband transition selection rules [54,55] allow only transition between valence and conduction subbands with same parity.

Figure 2.1: Schematic band diagram structure for a GaAs quantum well with AlAs as barrier material. The arrows indicate possible interband transitions between quantum well states due to interband selection rules.

At this point its important to define one more useful parameter which describes the strength of any optical transition known as oscillator strength. For interband transitions it has the form;

$$f = \frac{2m}{m_0 \hbar \omega_{ij}} \left| \langle i | \hat{L} \cdot \hat{r} | j \rangle \right|^2 \qquad (21)$$

where m_0 is the free electron mass, i and j are the initial and final states with energies E_i and E_f respectively, $\hbar\omega_{ij} = E_f - E_i$ and r) is the polarization vector and

r is the dipole matrix element.

2.2.2 Intersubband transitions in quantum wells

In a quantum confined structure such as a quantum well, optical transitions are observed between confined states within the same band (either conduction or valence band) and are referred as intersubband transitions. Progress in Physics of intersubband transitions in two dimensional structures and device applications such as quantum cascade lasers and infrared photodetectors has been recorded and continued to be explored especially with recent applications in intersubband THz QCls and THz emitters [56]. Figure 2.2 describes schematically intersubband transitions in GaAs (AlGaAs) quantum well (barrier) between first two subbands of a conduction band labelled n = 1 and n = 2 accomplished with photon (a) absorption and (b) emission.

Figure 2.2: Schematic diagram showing the process of intersubband transitions between confined quantum states in QWs (a) Absorption process and (b) emission process.

Intersubband transitions selection rule applied to quantum well conduction band requires that only polarized electric field perpendicular to the incident layer (TM-mode) can be coupled with the material excitations. This has an implication on device fabrication and system implementation which necessitate the use of complex geometry to experimentally perform optical absorption measurement [2,9].

However band mixing between heavy holes and light holes within valence band, allows coupling to both in-plane (TE) and out-plane polarized (TM) polarized electric fields. Thus, devices based on intervalence subband transitions [59, 60] have been demonstrated.

Within the frame work of a single particle approach and using the effective mass approximation, the wave function in a quantum well cam be written as the product of Bloch wave u_ν and envelope wave function f_{ν_i};

$$\psi_{\nu_i}(r) = u_\nu(r) f_{\nu_i}(r), \tag{2.2}$$

where ν is the band index (either conduction or valence band) and i is a quantum number ($i = 1, 2, ...$), representing quantum states within the same band. The envelope wave function f_{ν_i}reduced to plane wave approximation into a form

$$f_{\nu_i}(r, z) = \frac{1}{\sqrt{A}} e^{i(k_{||} \cdot r)} \varphi_{\nu_i}(z), \tag{2.3}$$

where A is the sample area, $k_{||} = k_x, k_y$ is the in-plane wave vector, $r = x, y$ is the position component for the in-plane wave and φ_{ν_i} is the slowly varying envelop functions. The envelope wave function appearing in Eq. 2.3 and the corresponding energy eigenvalue E_{ν_i} for a given subband i can be obtained by solving well known one-dimensional Schrödinger equation in the form [61];

$$\frac{p^2}{2m^*} \varphi_{\nu_i}(z) + V(z) \varphi_{\nu_i}(z) = E_{\nu_i} \varphi_{\nu_i}(z), \tag{2.4}$$

where m^* is spatial dependent effective mass, $V(z)$ is the potential energy in the QW, and z is considered as the growth direction of the QW. To allow for continuity of the envelop wave function at the boundary between the well and barrier layers, an additional boundary condition has to be imposed together with solution of Eq. 2.4 which implies that at the interfaces where $z = \pm d/2$, d being the well's width,

then:

$$\begin{aligned} \varphi_{\nu_i}(z=-d/2) &= \varphi_{\nu_i}(z=+d/2) \\ &\text{and} \\ \frac{1}{m^*}\frac{d^2}{d^2z}\varphi_{\nu_i}(z=-d/2) &= \frac{1}{m^*}\frac{d^2}{d^2z}\varphi_{\nu_i}(z=+d/2). \end{aligned} \tag{2.5}$$

For a symmetric QW, the envelope wave function is found to vary accordingly as; $\varphi_{\nu i}(z)$ has even parity for all odd states ($i = 1, 3, 5....$) and $\varphi_{\nu i}(z)$ having odd parity for even states ($i = 2, 4, 6....$). Further details can be found in relevant text books [61] and articles [57, 62] which treat intersubband transitions in QW structures in more details form.

2.2.2.1 Oscillator strength of intersubband transitions

For intersubband transition, the dimensionless oscillator strength for transition between different subbbands i and j of a conduction band is define as;

$$f_{ij} = \frac{2}{m^*\hbar\omega}|\langle i|e\cdot\vec{z}|f\rangle|^2, \tag{2.6}$$

where z is the dipole matrix element considering the QW growth direction. This oscillator strength obeys sum rule as it involves transition between initial states i to all final physical states j, according to;

$$\sum_j f_{ij} = 1 \tag{2.7}$$

2.2.2.2 Intersubband dipole matrix elements

The dipole matrix element $e \cdot \vec{z}$ of intersubband transitions can be evaluated using Eqs.(2.3) and (2.4) as;

$$\begin{aligned} |e \cdot \vec{z}| &= \langle u_\nu(r)|u_\nu(r)\rangle \int f_{\nu_j}(r) f_{\nu_i}(r) dr \\ &= 1 \int\int \frac{1}{\sqrt{A}} e^{i(k'_{||}\cdot r)} \frac{1}{\sqrt{A}} e^{i(k_{||}\cdot r)} \varphi^*_{\nu_j}(z) e \cdot \vec{r} \varphi_{\nu_i}(z) dr dz \\ &= \delta_{k'_{||}k_{||}} \int \varphi^*_{\nu_j}(z) e \cdot \vec{z} \varphi_{\nu_i}(z) dz \end{aligned} \tag{2.8}$$

for transition between state i and j. Here $k_{||}$ is the in-plane wavevector(k_x, k_y).

2.3 Analytical expression: cavity polariton/antipolariton

The basis to our nonequilibrium many body problem is generating the optical constants. In this approach a fully microscopic theory that gives rise to analytical expression for the dielectric constant leading to the polaritons and antipolaritons dispersion is presented. We then used the Maxwell's equations presented in the last chapter to derive the required wave equation that gives rise to a secular equation connecting cavity modes and the dielectric constant. The optical susceptibility and the optical polarization [63] are related by the equation,

$$P(\omega) = E(\omega, t)\chi(\omega), \tag{2.9}$$

where $E(\omega, t)$ is a propagating electric field and $\chi(\omega)$ is the optical constant (optical susceptibility).

Consider the geometry shown in Figure 2.3 as it appeared in [77]. The propagating electric field is assumed to be in z-direction and has the form for simplicity;

$$\overrightarrow{E} \cdot \widehat{Z} = E\cos(\pi/2 - \theta_2) = E\sin\theta_2 \tag{2.10}$$

and using Snell's law, $n\sin\theta = n_1\sin\theta_1 = n_2\sin\theta_2$, the angle in the cavity and the

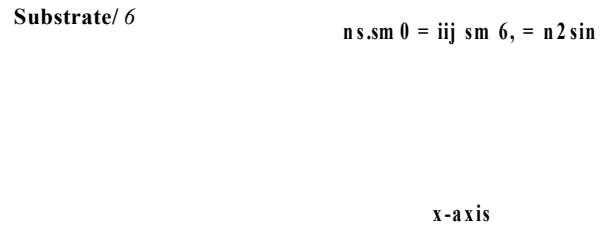

Figure 2.3: Cartoon of a microcavity leading to confinement of incident radiation in the cavity core due to total internal reflection between the low refractive index AlAs and air boundary as proposed in Ref. [77]

incident angle in the substrate *9* are related. Using wave equation a secular equation for the propagating electric field in the cavity core is formulated as;

$$\text{fqj} = \frac{ofl}{} esinO = — Si \sin\#i = \frac{ofl\ ofl}{} e_2 \sin\#2, \qquad (2\text{-}11)$$

where n'ni ancl n_2 are respectively the refractive indices for the substrate, cladding and cavity core. Because the cavity core consists of multiple quantum wells, the effective dielectric constant of the cavity core, *£eff = e2* is evaluated as;

$$£eff = Lc \sum_{3=1}^{N} Ljcj \qquad (2.12)$$

is thebackgrounddielectric constant due to well and barrier in thecavity core. *Lc —YliLi Lj* is thecavity width summing over *j = 1 to N* layers within the cavity core. The full dielectric constant with the contribution of effective dielectric constant

of the medium are connected with the optical susceptibility by the equation;

$$\varepsilon(\omega) = \varepsilon_{eff} + 4\pi\chi(\omega). \tag{2.13}$$

The analytical expression for the optical susceptibility is derived through a many body Keldysh Green's function Refs. [35,83] which reads:

$$\begin{aligned}[\hbar\omega - \check{e}_{\lambda\lambda'}(k) + i\Gamma_{\lambda\lambda'}]\,\chi_{\lambda\lambda'}(k,\omega) &- [f_\lambda(k) - f_{\lambda'}(k)]\sum_{k'} \check{V}^{\lambda\lambda'}_{k-k'}\chi_{\lambda\lambda'}(k',\omega) \\ &= \wp_{\lambda\lambda'}\,[f_\lambda(k) - f_{\lambda'}(k)]\,, \end{aligned} \tag{2.14}$$

where $\check{e}_{\lambda\lambda'}(k)$ is the transition energy between subbands λ, λ', renormalized by the intersubband shift [105–108] written as,

$$\check{e}_{\lambda\lambda'}(k) = \underbrace{e_{\lambda\lambda'}}_{\text{transition energy}} + \underbrace{\sum_{\lambda\lambda'}(k)}_{\text{intersubband shift}}\,. \tag{2.15}$$

The transition energy, is the energy difference between the coupled subbands, and $\sum_{\lambda\lambda'}(k)$ (intersubband shift) is due to many body interaction.

$$e_{\lambda\lambda'}(k) = e_\lambda(k) - e_{\lambda'}(k) \tag{2.16}$$

$$\begin{aligned}\sum_{\lambda\lambda'}(k) &= \sum_{k'} f_\lambda(k) V\begin{pmatrix}\lambda\lambda\lambda\lambda \\ k-k'\end{pmatrix} - \sum_{k'} f_{\lambda'}(k) V\begin{pmatrix}\lambda'\lambda'\lambda'\lambda' \\ k-k'\end{pmatrix} \\ &- \sum_{k'}[f_\lambda(k) - f_{\lambda'}(k)]\, V\begin{pmatrix}\lambda\lambda'\lambda'\lambda \\ k-k'\end{pmatrix}, \end{aligned} \tag{2.17}$$

where $V\binom{\lambda\lambda\lambda\lambda}{k-k'}$ is the Coulomb's contribution which is due to electron-electron, electron-hole and hole-hole interactions.

The Coulombs term in Eq.(2.14), $\check{V}^{\lambda\lambda'}_{k-k'}$, contains the exchange correlation

and the depolarization shift,

$$\check{V}^{\lambda\lambda'}_{k-k'} = \underbrace{V\begin{pmatrix}\lambda\lambda\lambda'\lambda'\\ k-k'\end{pmatrix}}_{exchange\,correlation} - 2\underbrace{V\begin{pmatrix}\lambda\lambda'\lambda'\lambda\\ 0\end{pmatrix}}_{\text{depolarization shift}}. \tag{2.18}$$

However, in many cases, there is a strong compensation between the intersubband shift and the exchange correlation and the dominating term contributing to the many body correction is the depolarization term. Thus if only the depolarization term is kept in Eq. 2.14, then we can rewite Eq. (2.14) as

$$\begin{aligned}[\hbar\omega - e_{\lambda\lambda'} + i\Gamma_{\lambda\lambda'}]\,\chi_{\lambda\lambda'}(k,\omega) \;&+\; 2V\begin{pmatrix}\lambda\lambda'\lambda'\lambda\\ 0\end{pmatrix}[f_\lambda(k) - f_{\lambda'}(k)]\sum_{k'}\chi_{\lambda\lambda'}(k',\omega)\\ &= \wp_{\lambda\lambda'}\,[f_\lambda(k) - f_{\lambda'}(k)]\end{aligned} \tag{2.19}$$

At this point, it is convenient to introduce simplified notations:

$$\begin{aligned}\Delta E_{\lambda\lambda'} &= \hbar\omega - e_{\lambda\lambda'} - i\Gamma_{\lambda\lambda'}\\ \delta n_{\lambda\lambda'} &= \underbrace{f_\lambda(k) - f_{\lambda'}(k)}_{\text{occupation difference}}\\ V_0^{\lambda\lambda'\lambda'\lambda} &= V\begin{pmatrix}\lambda\lambda'\lambda'\lambda\\ 0\end{pmatrix},\end{aligned} \tag{2.20}$$

while the symbols $\wp_{\lambda\lambda'}$ and $\Gamma_{\lambda\lambda'}$ represent the intersubband dipole moment and carrier scattering terms respectively. Furthermore, the following assumptions are considered here to further simplify the problem.

1. Same effective mass in each subband for all transitions.
2. The dipole moment does not depends on k-value, and
3. Scattering terms are independent of wave vector and frequency.

Thus, with the above assumptions and simplified notations, our equation for the susceptibility function can be reduced to;

$$\frac{1}{\Omega}\Delta E_{\lambda\lambda'}\chi_{\lambda\lambda'}(k,\omega)\wp_{\lambda'\lambda} + \frac{2}{\Omega}\mathrm{V}_0^{\lambda\lambda'\lambda'\lambda}\delta n_{\lambda\lambda'}\wp_{\lambda'\lambda}\sum_{k'}\chi_{\lambda\lambda'}(k',\omega) = \frac{1}{\Omega}\left|\wp_{\lambda\lambda'}\right|^2\delta n_{\lambda\lambda'} \tag{2.21}$$

Here we have multiplied both sides by $\frac{1}{\Omega}$ and $\wp_{\lambda'\lambda}$. By summing over k, Eq. 2.21 can be written as

$$\sum_k \frac{1}{\Omega}\Delta E_{\lambda\lambda'}\chi_{\lambda\lambda'}(k,\omega)\wp_{\lambda'\lambda}+\sum_k \frac{2}{\Omega}V_0^{\lambda\lambda'\lambda'\lambda}\delta n_{\lambda\lambda'}\wp_{\lambda'\lambda}\sum_{k'}\chi_{\lambda\lambda'}(k',\omega)=\sum_k \frac{1}{\Omega}\left|\wp_{\lambda\lambda'}\right|^2\delta n_{\lambda\lambda'}. \tag{2.22}$$

Due to spin degeneracy, the population difference $\delta n_{\lambda\lambda'}$ has the form

$$\delta N_{\lambda\lambda'} = 2\sum_k \delta n_{\lambda\lambda'}(k) \tag{2.23}$$

Introducing $\chi_{\lambda\lambda'}(\omega) = \frac{1}{\Omega}\sum_{k'}\wp_{\lambda'\lambda}\chi_{\lambda\lambda'}(k',\omega)$, where Ω is a sample volume as in the case of interband transitions, the above Eq.(2.21) becomes,

$$\Delta E_{\lambda\lambda'}\chi_{\lambda\lambda'}(\omega)+\delta N_{\lambda\lambda'}\,V_0^{\lambda\lambda'\lambda'\lambda}\,\chi_{\lambda\lambda'}(\omega)=\frac{1}{\Omega}\left|\wp_{\lambda\lambda'}\right|^2\,\delta N_{\lambda\lambda'}/2. \tag{2.24}$$

The analytical expression for the full optical susceptibility is then obtained from Eq. 2.24, $\chi(\omega)=\sum_{\lambda\neq\lambda'}\chi_{\lambda\lambda'}(\omega)$,

$$\chi(\omega) = -\sum_{\lambda\neq\lambda'}\frac{1}{d_\omega}\frac{\left|\wp_{\lambda\lambda'}\right|^2\delta\eta_{\lambda'\lambda}}{\Delta E_{\lambda\lambda'}+\delta\varrho_{\lambda\lambda'}}, \tag{2.25}$$

where $\delta\eta_{\lambda\lambda'} = -\delta n_{\lambda'\lambda}/S$ is the population density difference between subbands $(\lambda,\lambda' = 1,2,3...)$. S is the sample area and d_ω represents the width of the well's material. In Eq. 2.25, $\delta\varrho_{\lambda\lambda'}$ substituted $\delta N_{\lambda\lambda'}V_0^{\lambda\lambda'\lambda'\lambda}$ which appeared in Eq. 2.24.

Using the relation $\epsilon(\omega)=\epsilon_b+4\pi\chi(\omega)$, the optical dielectric function is obtained.

$$\epsilon(\omega) = \varepsilon_b - 4\pi\sum_{\lambda\neq\lambda'}\frac{1}{d_\omega}\frac{\left|\wp_{\lambda\lambda'}\right|^2\delta\eta_{\lambda'\lambda}}{\Delta E_{\lambda\lambda'}+\delta\varrho_{\lambda\lambda'}} \tag{2.26}$$

and with Eq. 2.26 and Eq. 1.3, substituting k^2 with $k_{||}^2+k_\perp^2$ we obtain the following dispersion relation.

$$c^2(k_{||}^2+k_\perp^2) = \omega^2\left(\varepsilon_b - 4\pi\sum_{\lambda\neq\lambda'}\frac{1}{d_\omega}\frac{\left|\wp_{\lambda\lambda'}\right|^2\delta\eta_{\lambda'\lambda}}{\Delta E_{\lambda\lambda'}+\delta\varrho_{\lambda\lambda'}}\right), \tag{2.27}$$

where $k_{||}^2 + k_{\perp}^2$ are wave vectors parallel and perpendicular to the growth direction of the quantum well due to electric field confinement in the microcavity.

2.4 Numerical calculations and approximations

For simplicity, we consider the energy levels of a heavy holes confined in an infinite potential well. The well and barrier materials are GaAs and AlGaAs respectively. The transition energy between the first two subbands, neglecting depolarization shift effect is

$$E_n = \frac{\hbar^2}{m^*}\frac{n\pi^2}{d_\omega^2} \tag{2.28}$$

where m^* is the effective mass, n is integer and d_ω the well width. For a 10nm quantum well and using heavy holes effective mass $(\mathrm{m}^*_{hh}) = 0.45$ [64, 65]

$$\begin{aligned} E_{HH_1} &= \frac{\hbar^2}{2m^*_{HH_1}}\frac{\pi^2}{d_\omega^2} \approx 8.3594meV \\ E_{HH_2} &= \frac{\hbar^2}{2m^*_{HH_2}}\frac{2\pi^2}{d_\omega^2} \approx 33.4378meV \\ \Rightarrow \Delta E_{2,1} &= 33.4378 - 8.3594 = 25.0783meV \end{aligned} \tag{2.29}$$

This corresponds to a transition wavelength $\lambda = 1.24/\Delta E \approx 49.45$ micron or equivalently 6.06 THz.

The transition dipole moment is evaluated directly by considering the eigenfunctions for the two states; $\psi_n(z) = A\sin(k_z z)$ and $\psi_n(z) = A\cos(k_z z)$ for even and odd state respectively. These are obtained from general form of the eigenfunction, $\psi_n(z) = A\sin(k_z z) + B\cos(k_z z)$, which satisfies Schrödinger equation for one dimensional for infinite barrier problem;

$$H\psi = E\psi, \tag{2.30}$$

where A and B are normalization constants. By applying boundary conditions [66, 67], we found $A = \sqrt[2]{L_z}$, $B = 0$ for even state and vice versa for odd state. To

summarize, the equation for the transition dipole matrix element has the form

$$\wp_{2,1} = \langle\psi_2(z)|e.z|\psi_1(z)\rangle. \tag{2.31}$$

Evaluating the integral above, taking limits from $-L_z/2$ to $+L_z/2$, then Eq. (2.31) reduces to;

$$\begin{aligned} \wp_{2,1} &= -\frac{16eL_z}{9\pi^2} \\ &= 2.5nm \end{aligned} \tag{2.32}$$

for the 10 nm quantum well. Here e is electronic charge.

More accurate soulution including band coupling between conduction band electron, heavy and light holes using k.p theory (section 2.4). In the context of this numerical approximation, here we assumed a carrier density $\delta_n = 1.5 \times 10^{11} cm^{-2}$ and calculated $\Delta^{'}$ using Eq. 2.27 as;

$$\begin{aligned} \Delta^{'} &= \frac{-4\pi}{\varepsilon_\infty}|\wp^2_{\lambda\lambda'}|^2\delta_\eta \\ &= \frac{-4 \times (3.14)^2}{10.89} \times |2.5nm|^2 \times 1.5 \times 10^{11} cm^{-2}. \end{aligned} \tag{2.33}$$

Figures. 2.4a and 2.4b show the polariton and antipolariton dipersions obtained with these approximation. The cavity length is approximately 18.4μm containing 165 quantum wells. In the next chapters, results using full analytical expressions for the energy dispersions of the polariton and antipolariton problems are presented for single and multiple transitions with full nonequilibrium many body problem. The influence of dephasing and other relevance parameters such as cavity length, quantum well width and barrier height are considered and analysed. The results presented here are based on simple numerical approximations.

The results present in Figure 2.6 (a) and (b) show the influence of changing the carriers density in the polariton and antipolariton dispersions respectively. In both cases the two branches are pulled far apart as the carrier density increases (details

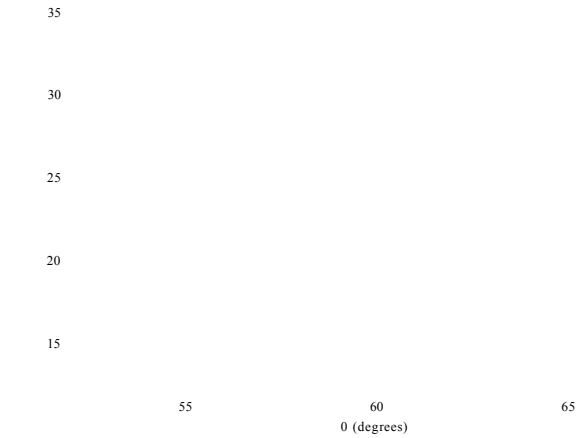

(a)

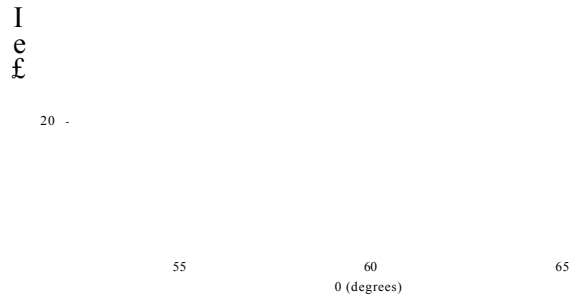

(b)

Figure 2.4: Microcavity polariton (a) and antipolariton (b) obtained using a numerical approximation with transitions between the first two valence subbands. The population difference between subbands are ±1.5 x 10^{11} cm^{-2} *corresponding to absorption or gain leading to polariton or antipolariton respectively. The result is TE-mode polarized in the Infrared range.*

is given in the Figure caption). The combined effects of changing the carrier density is shown in Figure 2.7.

In order have a quantitative idea on the optical absorption for this transition, the intersubband optical absorption **ck(u;)** is related to the optical susceptibility shown

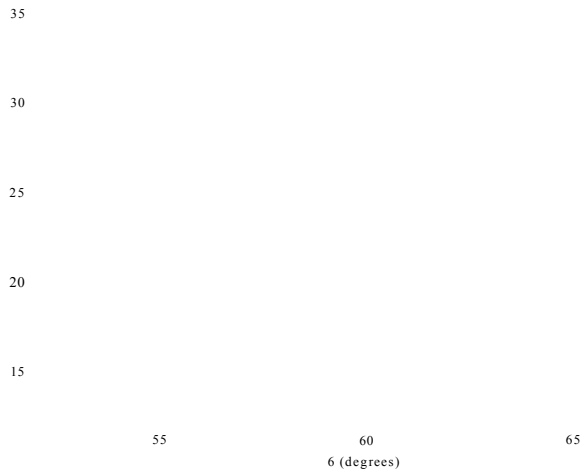

Figure 2.5: Combination of microcavity polariton and antipolariton from numerical calculation for a 10 nm GaAs/Alo^GaojAs multiple quantum wells.

in Eq. 2.25 by the relation [68];

$$a(w) = \frac{}{cnb} /m \text{ x } M , \tag{2.34}$$

where nb is the background refractive index and c is the speed of light in the medium. We computed the intersubband optical absorption for the transition between the HH_1 to HH2 and as presented in Figure 2.7 with increasing dephasing (7 = 0.1, 0.2, 0.4 and 0.6 meV) respectively. Note that for the polaritons/antipolaritons problem in this simple approach, the dephasing is completely neglected (7 = O.OraeF). Figure 2.7 clearly shows that absorption peak diminishes and more broadening is obtained with large dephasing (i. e. $7 = 0.6meV$ in this case).

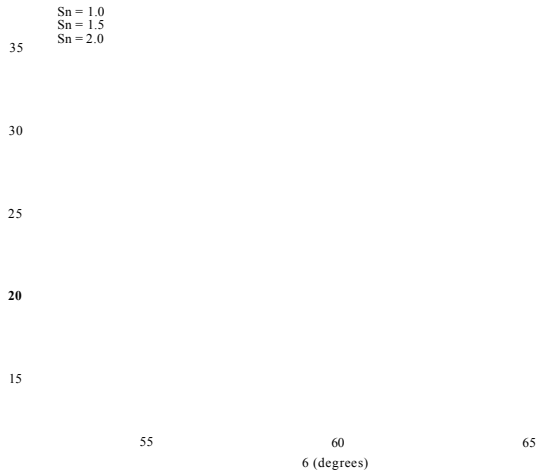

(a)

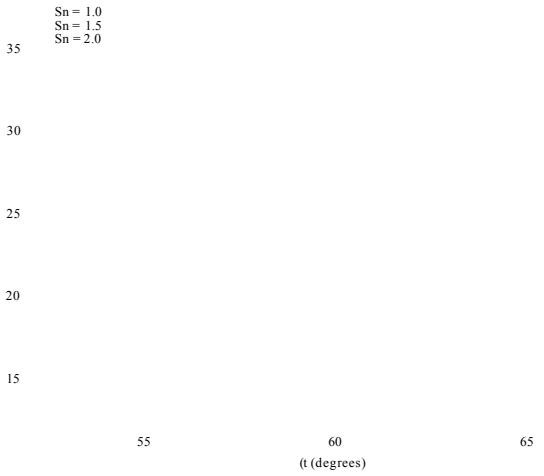

(b)

Figure 2.6: Microcavity polaritons (a) showing the influence of changing population density. As the population density difference increases from 6n — 1.0, 1.5 to 2.0, x10 11cm~2 (red to blue), the separation between the branches also increases leading to a large splitting between the two polaritons branches. In the case of antipolariton (b), the density increased to a more negative values Sn = —1.0, —1.5 to —2.0, x10^ra-2 and this lead to less stability of the two branches.

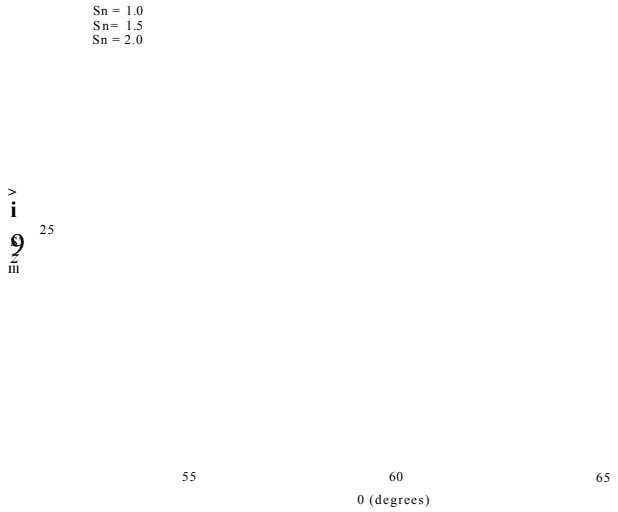

Figure 2.7: Combination of polaritons and antipolaritons for different population densities.

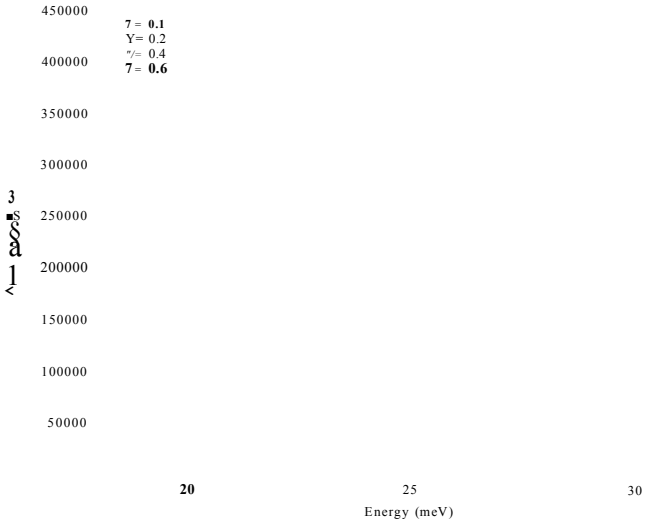

Figure 2.8: Intersubband optical absorption for the transition between HH1 - HH2 in GaAs/AlGaAs QWs computed using Eq. (2.34) for difference dephasing values as indicated. It can be seen clearly that there is shrinkage in the absorption spectrum as the dephasing increases (from red to orange).

2.5 Conclusion

In conclusion, this chapter served as a stepping stone for the studies that follow. A review of polaritons and antipolaritons is presented, an analytical expression for the cavity polaritons/antipolaritons is derived and a simple numerical approach is applied which lead to the energy dispersion relations for the polararitons/antipolaritons in the THz range. The result also indicates that the polaritons and antipolaritons character can be controlled by changing population density difference between the coupled subbands. To further gain insight into the understanding of the optical absorption process in the medium, we have evaluated the optical absorption at different dephasing conditions which shows that as the dephasing increases, the energy broadening increases while the absorption peak is reduced. This is very significant for controlling the population density occupancy in a given subband.

CHAPTER 3
VALENCE BAND POLARITONS AND ANTIPOLARITONS

3.1 Introduction

In this chapter we derive analytical expressions leading to the energy dispersion relations for valence band polaritons and antipolaritons. We consider the case of a single transition between the first two inter-valence subbands applied to GaAs/AlGaAs multiple quantum wells. We propose a simple geometry that allows the coupling at terahertz frequencies between TE-mode polarized microcavity modes with QWs inter-valence band excitations.

Starting from non-equilibrium many body solution to the optical response we investigate the influence of dephasing mechanism, and its consequences for polaritons and antipolaritons dispersion relations with varying quantum wells widths, populations density between the coupled subbands and increasing cavity length.

Intersubband polaritons have been studied in the context of inter-conduction band transitions with transverse electromagnetic (TM) mode polarization [59, 73]. However inter-valence band based design allow photon emission or absorption normal to the surface [60].

In the next chapters we show results for intervalence band transitions that allow THz polaritons and antipolaritons in the TE and TM mode cases. However before that, a brief introduction of K.P theory is given below.

3.2 The k.p theory

The k.p theory has been widely used and found successful in calculating the band structure and optical properties of semiconductors. Using perturbation theory

and in the frame work of Luttinger-Kohn and or Kane models, k.p can be used to extrapolate the band structure of a solid semiconductor in particular over the Brillion zone. This can easily be achieved if the eigenfunctions and energy eigenvalues of the material are known at the $\Gamma-$point (where the band extrema of the conduction band minima and valence band maxima coincide). In one band electron picture, the k.p method can be derived from Schrödinger equation. Neglecting spin orbit interaction, the Hamiltonian equation can be written as;

$$\left[\frac{p^2}{2m} + V(r)\right] \psi_{n,k} = E_{n,k}\psi_{n,k}, \tag{3.1}$$

where V(r) is the periodic crystal potential and m is the free electron mass. The Bloch wave function $\psi_{n,k}$ in Eq. 3.1 can be written according to Bloch theorem

$$\psi_{n,k} = e^{ik.r}u_{n,k}(r), \tag{3.2}$$

where $u_{n,k}(r)$ is Bloch lattice function with the periodicity of lattice. Substituting Eq. 3.2 into Eq. 3.1 gives the following equation,

$$[H_o + H^p]\, u_{n,k}(r) = E_{n,k}u_{n,k}(r), \tag{3.3}$$

where $H_o = \frac{p^2}{2m} + V(r)$ is the unperturbed Hamiltonian and $H^p = \frac{\hbar^2 k^2}{2m} + \frac{\hbar}{m}k \cdot p$ is the perturbation Hamiltonian. At gamma (Γ) point i.e. $k = k_o = 0$, Eq. 3.3 reduces to the form in Eq. 3.1

$$\left[\frac{p^2}{2m} + V(r)\right] u_{n,o} = E_{n,k}u_{n,o}(r). \tag{3.4}$$

The above Eq. 3.4 can easily be solved compared to Eq. 3.1, because of the periodic nature of the Bloch lattice function, the solution of which form a complete and orthogonal set of basis function. Thus, once $E_{n,o}$ and $u_{n,o}$ are known, we can calculate the energies and waves functions at some other k-values at the vicinity of Γ-point. The analysis is called k.p due to the terms proportional to power of $k \cdot p$. The result of which are energy eigenvalues ($E_{n,k}$) and eigenfunctions $u_{n,k}$ as expansion

of $E_{n,o}$ and $u_{n,o}$ at $k = 0$ respectively. Neglecting spin orbit interaction, the results obtained using non-degenerate perturbation theory for the energy eigenvalues and the eigenfunctions are [69];

$$u_{n,k} = u_{n,o} + \frac{\hbar}{m} \sum_{m \neq n} \frac{\langle u_{n,o}|k \cdot p|u_{m,o}\rangle}{E_{n,o} - E_{m,o}} u_{m,o}$$

and

$$E_{n,k} = E_{n,o} + \frac{\hbar^2 k^2}{2m} + \frac{\hbar^2}{m^2} + \sum_{m \neq n} \frac{|\langle u_{n,o}|k \cdot p|u_{m,o}\rangle|^2}{E_{n,o} - E_{m,o}} \tag{3.5}$$

In a more general form, energy eigenvalues can be re-written as;

$$E_{n,k} = E_{n,o} + \frac{\hbar^2 k^2}{2m^*} \tag{3.6}$$

where m^* is the electrons(holes) effective mass given by

$$\frac{1}{m^*} = \frac{1}{m} \left[1 + \frac{2}{mk^2} \sum_{m \neq n} \frac{|\langle u_{n,o}|k \cdot p|u_{m,o}\rangle|^2}{E_{n,o} - E_{m,o}} \right] \tag{3.7}$$

which can be used to calculate the effective mass of the non-degenerate band. Thus, the dispersion relation obtains using k.p is parabolic in k, as long as k is small or the term $|E_{n,k} - E_{m,o}|$ is much smaller than the band edge gap with the band extrema at $k = 0$. More realistic results could be obtain by considering the case of degenerate band in a valence band which are treated in relevant articles [69–71] and textbooks [63, 72]

3.3 Main equations and mathematical model

The polaritons and antipolaritons energy dispersion relations presented in the following section are based on the dielectric function formalism. The full optical susceptibility stems from a self consistent evaluation of many body Green function [84, 85, 87, 89]. The incident angle θ is used as reference angle for the THz polaritons and antipolaritons problem as shown in the proposed geometric structure of Figure 3.1, and can be obtained experimentally by turning the incident angle

around the normal and comparing with the extrema on the reflection or transmission spectra as in Ref. [77] .

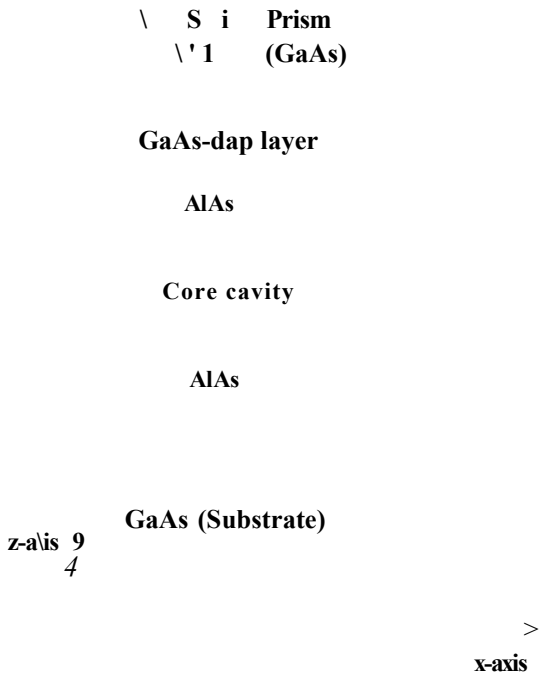

Figure 3.1: Cartoon of the proposed geometric structure showing the directions of the propagating electric fields for TE-polarized THz radiation. The low refractive index AlAs below and above the active region confines the electric fields due to total internal reflection. 6 and 6s are the incident and core cavity angles respectively.

The first step in the numerical method is the calculation of the nonequilibrium many body optical response of the quantum wells in the cavity core. The formalism is the same as those found in Refs. [84,85] with the main difference that here the system is globally out of equilibrium but the electrons are assumed to be independently thermalised within only one subband with occupation functions characterised by temperatures. These can be extremely different from the lattice temperature, similarly to the case of electrons in conduction-band based QCLs as found in microprobe photoluminescence experiments in quantum cascade lasers [86]. The total number of electrons in each subband can be controlled in practice by optical pump-

ing, selective doping or a combination of both methods. Significantly, this formalism can be applicable to both intersubband [78, 79] and interband [80–82] cases.

The scheme used to obtain the full solution for the susceptibility can be summarized as follows: The first step is the solution of the 8 band k · p Hamiltonian. The Green's functions and self-energies are expanded using eigenstates and eigenvalues of this Hamiltonian. Next, by assuming thermalised electrons in each subband, the full Nonequilibrium Green's functions scheme [88, 89] is simplified and reduces to the self-consistent evaluation of chemical potentials and self-energy matrix elements [84]. Finally, the local optical susceptibility and thus the dielectric function given by matrix numerical inversion of the integro-differential equation are obtained from the carriers Green's function in linear response. Thus, the green functions equations with contribution beyond the Hartree-Fock in the limit $t_1 = t_2 = t$ can be written as [90];

$$\hbar\left(\frac{\partial}{\partial t} + i\left(e_\nu - e_\mu\right)\right) G^{<}_{\nu\mu}(k,t) + \left(G^{<}_{\mu\mu}(k,t) - G^{<}_{\nu\nu}(k,t)\right) \times \left\{\vec{\wp}_{\nu\mu}\cdot\vec{E}(t) + \sum_{\vec{k}'} G^{<}_{\nu\mu}(k',t)\tilde{V}\begin{pmatrix}\nu\mu\\ \vec{k}-\vec{k}'\end{pmatrix}\right\} = I_{\nu\mu}. \quad (3.8)$$

Here the Hartree contribution is given on the left hand side of the above equation and correlation terms beyond Hartree Fock is included on the right hand side. $\tilde{V}$ is the Coulomb potential and includes the depolarization terms while $\vec{\wp}$ account for the the dipole matrix element. Furthermore, the correlation term on the right hand side of 3.8 has the form,

$$I_{\nu\mu}(k,t) = \sum_{\lambda}\int_{-\infty}^{t} dt'\left[\Sigma^{<}_{\nu\mu}(k,tt')G^{>}_{\lambda\mu}(k,tt') + \sigma^{>}_{\nu\lambda}(k,tt')G^{<}_{\lambda\mu}(k,tt') - (>\Leftrightarrow<)\right]. \quad (3.9)$$

Detailed evaluations of the correlations terms can be found in [84] including self energy $\Sigma^{</>}$ and depolarizations shifts. Upon projecting the classical electric fields $(\vec{E})$ along the dipole moment, the susceptibility function can be extracted from its

Fourier transform component in the frequency domain, $\chi(k,\omega) = -i\hbar G^{<}_{\nu\mu}(k,\omega)/E$ and are given by,

$$\chi(\omega) = \frac{2}{V}\sum_{\mu\neq\nu,\vec{k}} \wp(k)\chi(k,\omega). \tag{3.10}$$

The full optical susceptibility is then numerically calculated and adjusted using the simple formula in Eq. 3.11.

$$\chi(\omega) = -\frac{1}{4\pi}\frac{\Lambda}{\omega - \omega_1 + i\delta}. \tag{3.11}$$

The imaginary parts of the optical susceptibility is obtained from nonequilibrium many body solutions (NEGF) and its adjusted Lorentzian fits (with and without Rotating wave approximation) are depicted in Figures 3.2a and 3.2b for 1-2 and 2-1 transitions corresponding to absorption and gain regime respectively. In Figure 3.2a, the population density difference between the coupled subbands is $\Delta N = \pm 2.0 \times 10^{11} cm^{-2}$ corresponding to absorption/gain regime. In other words for for the 1-2 transition, the first (top) valence subband is assumed to be fully occupied and the second subband considered empty (unoccupied) and vice-versa for 2-1 transition. Similar results are given in Figures 3.3a and 3.3b with populations density difference $\Delta N = \pm 1.0 \times 10^{11} cm^{-2}$. Finally, the parameters ω_1 , Λ and δ in Equation 3.11 are numerically computed and are used as the input to the optical dielectric function. In Appendix A.1, we show how the fitting parameters are obtained by using the Lorentzian formula with rotating wave approximation (RWA) only (Equation 3.11). For comparison, in Appendix A.2, similar equation for Λ is presented, if the full Lorentzian formula is used. In both cases, the resultant optical susceptibilities obtained are compared(See Appendix A) with those from NEGF numerical data.

In order to justify our approximation (i.e. using Eq. 3.11), we compare in Table 3.1, the numerical values of the fitting parameters obtained using the RWA only and those obtained with full Lorentzian fit formula. One may notice that, the numerical values in Table 3.1 computed using the two formulas are almost the same. However a small discrepancy is shown for the numerical value of Λ which is

due to the unsymmetrical nature of the optical susceptibilities from the numerical calculations and the small differences in dephasing as well. This has no significant effect in the expression used in our approximation.

Table 3.1: *Comparison of Input parameters extracted using Lorentzian fit with rotating wave approximation (RWA) part only compared with those obtained using full Lorentzian formula (i.e including the non rotating part) for different carrier density,* $\Delta N(\times 10^{11} cm^{-2})$*, between the coupled subbands.*

ΔN	Parameter	Lortz. fit RWA only	Full Lortz. Fit
0.2	Λ	10.0624	9.8840
	ω_o	10.2628	10.2628
	δ	4.7559	4.2553
1.0	Λ	5.3710	4.8136
	ω_o	10.0125	10.2628
	δ	5.5068	5.5062
-0.2	Λ	-12.7535	-11.5033
	ω_o	8.7609	8.7609
	δ	4.7559	4.0050
-0.1	Λ	-6.4618	-5.4176
	ω_o	9.2615	9.2615
	δ	5.2565	4.5056

Furthermore, one may notice from both Figures 3.2 and 3.3 that, the two curves obtained with the Lorentzian fits (RWA fit (dot dot black) and full fit (dash blue) lines) all fit the curve resulting from the full NEGF-solution (dash green). However, on careful observation, a better fit is obtained using the Lorentzian fit with RWA only (compare dot dot black and the dash green lines). In Appendix A the imaginary parts of the optical susceptibilities obtained by fitting with RWA (A.1) part only, and with full (RWA + NRWA) parts are compared with those generated from the numerical (NEGF) solutions for different densities, further validating our approximation.

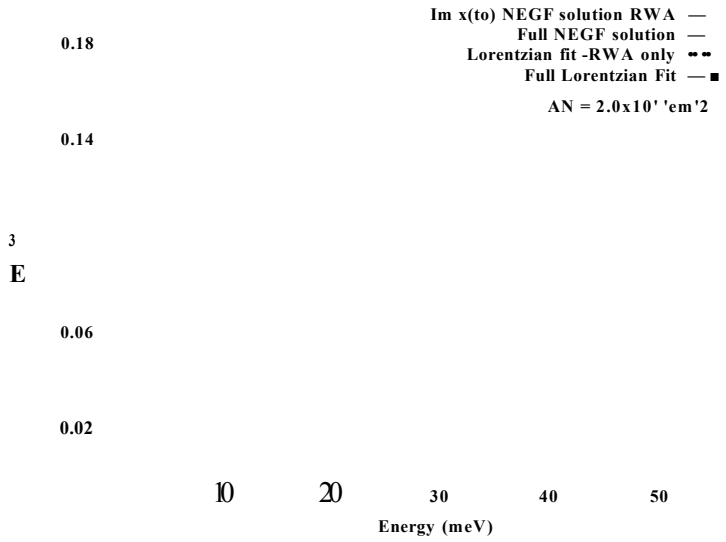

(a)

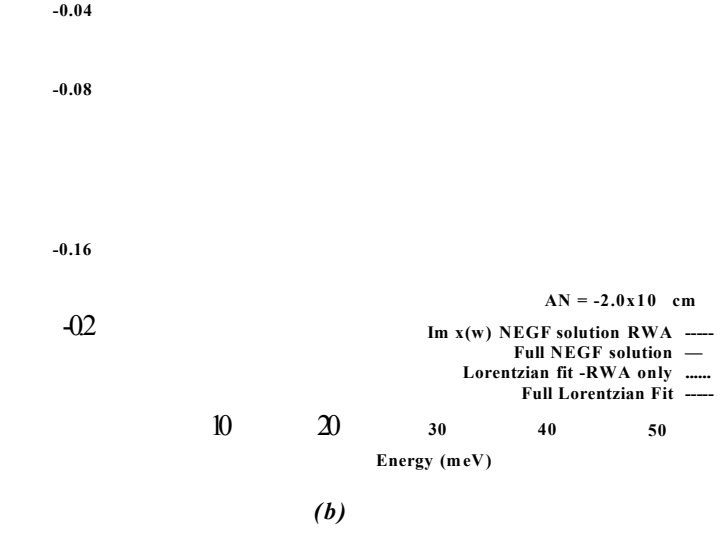

(b)

Figure 3.2: Imaginary part of the optical susceptibility generated self-consistently using nonequilibrium many body Green's functions (NEGF) (red and green) with a Lorentzian fit including both rotating and non rotating terms. The population density is assumed to be thermalized at $T = 300K$*, with (a) second subband population* $N = 2.0 \times 10$ *and first subband unoccupied and (b) first subband population* $N = 2.0 \times 10^{11}\,\mathrm{cm}^{-1}$.

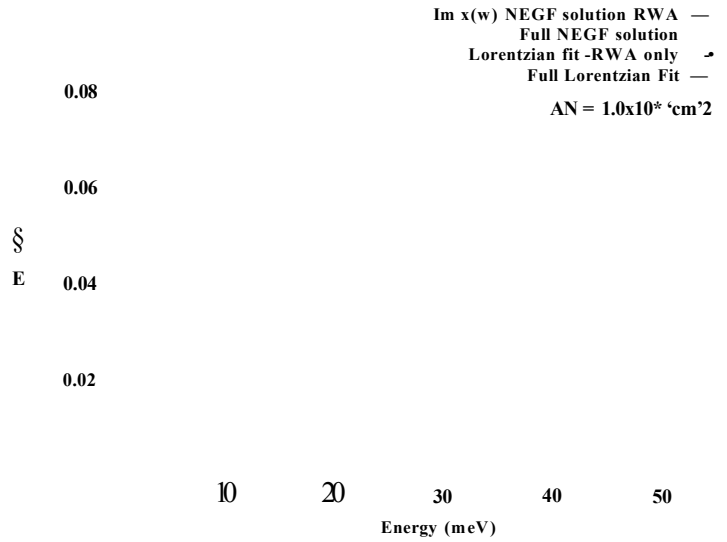

(a)

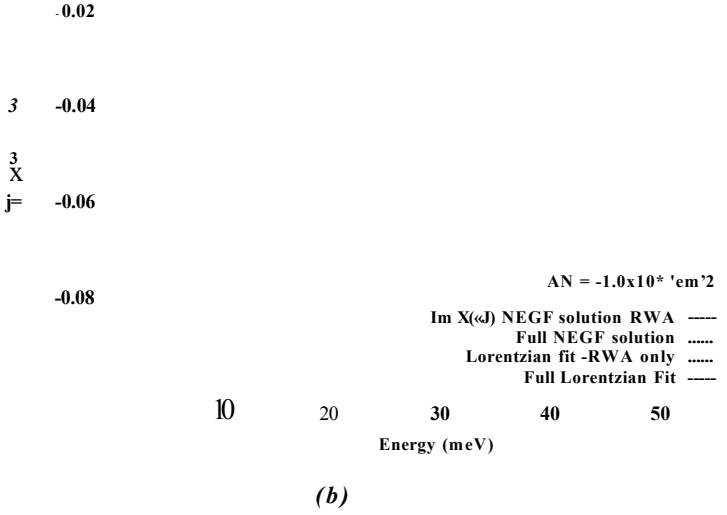

(b)

Figure 3.3: Imaginary part of the optical susceptibility generated self-consistently using nonequilibrium many body Green's functions (NEGF)(red) compared with a Lorentzian fit including both rotating and non rotating terms. The population density is assumed to be thermalized at T = 300K, with (a) second subband population N = 1.0 x 10n cm_1 and first subband unoccupied and (b) first subband population N — 1.0 x 10n cm~1.

3.3.1 Modelling the optical dielectric function

The dielectric constant is obtained in an approach used upon its connection with the optical susceptibility as shown in Eq. 3.12 below.

$$\varepsilon(\omega) = \varepsilon_b + 4\pi\lambda\chi(\omega), \tag{3.12}$$

where $\chi(\omega) = \chi^{'}(\omega) + i\chi^{''}(\omega)$. The Lorentzian fit to the optical susceptibility with both rotating and non-rotating terms for a transition between two valence subbands $(\mu = 2, \nu = 1)$ is given as;

$$\chi(\omega) = -\frac{1}{4\pi}\left[\frac{\Lambda_{\mu,\nu}}{\omega - \omega_{\mu,\nu} + i\delta_{\mu,\nu}} - \frac{\Lambda_{\mu,\nu}}{\omega + \omega_{\mu,\nu} + i\delta_{\mu,\nu}}\right], \tag{3.13}$$

where ω , $\omega_{\mu\nu}$ are the photons and transition energy between the coupled subbands $(\mu \neq \nu)$ respectively. Lambda '$\Lambda_{\mu,\nu}$' is related to the oscillator strength of the transition. and $\delta_{\mu,\nu}$ is the Lorentzian line shape or broadening (dephasing) term. Substituting the real and imaginary parts of Equation (3.13) in 3.12, the real part of the dielectric constant[1] $\varepsilon^{'}(\omega)$ can be written as

$$\varepsilon^{'}(\omega) = \varepsilon_b\left[1 - \frac{\lambda\Lambda_{\mu,\nu}}{\varepsilon_b}\left(\frac{\omega - \omega_{\mu,\nu}}{(\omega - \omega_{\mu,\nu})^2 + \delta^2} - \frac{\omega + \omega_{\mu,\nu}}{(\omega + \omega_{\mu,\nu})^2 + \delta^2}\right)\right] \tag{3.14}$$

and the imaginary part[2] $\varepsilon^{''}(\omega)$ as;

$$\varepsilon^{''}(\omega) = \lambda\Lambda_{\mu,nu}\left[\frac{\delta_{\mu,\nu}}{(\omega - \omega_{\mu,\nu})^2 + \delta^2} - \frac{\delta_{\mu,\nu}}{(\omega + \omega_{\mu,\nu})^2}\right]. \tag{3.15}$$

Here ε_b is the background dielectric constant of the core cavity due well and barrier materials, $\lambda = \frac{NwLw}{Lc}$ is an anisotropic medium parameter [83] that arises in the cavity and finally N_ω , L_ω and L_c are respectively: the number of quantum wells in the cavity, quantum well width and the cavity thickness.

[1]The real part lead to the energy dispersion

[2]The imaginary part define the absorption peak

3.3.2 Photon confinement

In order to enhance the coupling of the electromagnetic fields and induced inter-subband excitations in the medium, we propose a simple geometric structure where photon confinement is achieved through total internal reflection at the interfaces between the cavity core and low refractive index AlAs-layers placed at the top and bottom of the structure. The core cavity has GaAs/AlGaAs multiple quantum wells (MQWs) layers forming the background refractive index (n_b). The schematic geometry is presented in Figure 3.1.

For TE-mode coupling, the component of the electric fields is polarized along the Y-axis and is given by $E_{\mathrm{y}} = E_{o\mathrm{y}} e^{i(k_{\mathrm{y}}\mathrm{y})} e^{i(k_z z)}$ with propagating fields along the growth-direction (z-axis), so that the in-plane wave vector $k_{\parallel} = k_{\mathrm{y}} = \frac{\omega}{c} n_b sin\theta_b$ and the perpendicular wave vector $k_{\perp} = k_z$ describe the propagating fields in the medium. Furthermore, if we assume total reflection at the cavity and semiconductor mirrors interfaces, then the Z component of the propagating wave vector, k_z can be approximated as $k_z = \frac{\pi}{L_c}$.

The microcavity modes are obtained from the wave Equation;

$$\frac{\omega^2}{c^2} n_b^2 \sin^2\theta_b + \frac{\pi^2}{L_c^2} = \frac{\omega^2}{c^2}\varepsilon(\omega), \tag{3.16}$$

where n_b is the background refractive index of the cavity core, ${\theta_b}^3$ is the angle inside the core cavity, which is related to the incident angle (θ) by Snell's law .

3.3.3 Energy dispersion relations

The polaritons/antipolaritons energy dispersions are finally deduced by substituting the real part of Equation (3.16) into Equation (3.14). Considering a simple case for single transition, by suppressing the dephasing term, that is letting $\delta_{\mu,\nu} = 0$.

[3] due to total internal reflection inside the core cavity, θ_b may be complex

Equation (3.16) can be written as;

$$\frac{\omega^2}{c^2}\frac{\varepsilon_s}{\varepsilon_b}\sin^2\theta + \frac{\pi^2}{\varepsilon_b L_b^2} = \frac{\omega^2}{c^2}\frac{\varepsilon'}{\varepsilon_b}. \tag{3.17}$$

Using Equation 3.14, re-arranging and neglecting the contribution of imaginary part as stated above, we finally obtained

$$\omega^2\beta^2 + \omega_c^2 = \omega^2\left\{1 - \lambda\Delta\left(\frac{2\omega_{\mu,\nu}}{\omega^2 - \omega_o}\right)\right\}. \tag{3.18}$$

In Equation 3.17 and 3.18, we introduced new variables to simplify the expression which includes: $\beta^2 = \frac{\varepsilon_s}{\varepsilon_b}\sin^2\theta$ where θ is the incident angle and ε_s is the dielectric constant of the substrate material which is used as prism to enable the incident beam reaches the cavity core. The term $\omega_c = \sqrt{\frac{\pi^2 c^2}{\varepsilon_b L_c^2}}$ represents the cavity resonance frequency, ω_o is a chosen resonance frequency equal to the intersubband transition frequency $\omega_{\mu,\nu} = \omega_\mu - \omega_\nu$ at resonance and $\Delta = \frac{\Lambda_{\mu,\nu}}{\varepsilon_b}$ is called the Longitudinal transverse splitting. Furthermore, we have some normalization in the former equation and thus it becomes;

$$\begin{aligned}
\mathrm{y}^2\beta^2 + \Omega_c^2 &= \mathrm{y}^2\left\{1 - 2\lambda\Delta'\left(\frac{1}{\mathrm{y}^2 - 1}\right)\right\} \\
&= \mathrm{y}^2 - 2\lambda\Delta'\left(\frac{\mathrm{y}^2}{\mathrm{y}^2 - 1}\right) \\
\left(\mathrm{y}^2 - 1\right)\left[\mathrm{y}^2\beta^2 + \Omega_c^2\right] &= \mathrm{y}^2\left(\mathrm{y}^2 - 1\right) - 2\mathrm{y}^2\lambda\Delta' \\
&= \mathrm{y}^4 - \mathrm{y}^2 - 2\mathrm{y}^2\lambda\Delta',
\end{aligned} \tag{3.19}$$

where $\mathrm{y} = \omega/\omega_o$, $\Omega_c = \omega_c/\omega_o$ and $\Delta' = \Delta/\omega_o$ are introduced. Furthermore Equations (3.19), can be rearranged, substituting the parameter $\mathrm{y} = \hbar\omega$ and finally we obtain the following analytical expression for the THz polaritons/antipolaritons energy dispersion relations.

$$\hbar\omega = \hbar\omega_o\sqrt{\frac{1 - \beta^2 + \Omega_c^2 + 2\lambda\Delta' \pm \sqrt{\left(1 - \beta^2 + \Omega_c^2 + 2\lambda\Delta'\right)^2 - 4\left(1 - \beta^2\right)\Omega_c^2}}{2\left(1 - \beta^2\right)}} \tag{3.20}$$

3.4 Numerical results and discussions

Before the numerical results are presented, we summarized in table 3.2 relevant parameters used as inputs. These are obtained numerically by adjusting our nonequilibrium many body solution for the optical response and other input data extracted from previous literature for the chosen materials in the active region(GaAs/AlGaAs) and cladding (AlAs).

Table 3.2: *Relevant parameters used as input to deliver simulations for the structure shown in Fig. 3.1 leading to the THz polaritons and antipolaritons depicted in Figs. 3.5 and 3.6 respectively.*

Parameter	Discription	Numerical value	
	Medium	Absorption	Gain
L_b	Barrier length (nm)	220.0	220.0
L_w	Quantum well width (nm)	10.0	10.0
λ	Cavity factor	0.0432	0.0432
L_c	Microcavity Length (μm)	38.1699	38.1699
$\Lambda_{\mu,\nu}$	Coupling coefficient (meV)	9.4696	-12.7535
$\omega_{\mu,\nu}$	Transition Energy (meV)	10. 3960	8.7609
ε_b	Background Diel Constant	10.1066	10.1066
ε_s [91]	GaAs High Freq. Diel. Const.	10.89	10.89
ε_{br}	$(Al_xGa_{1-x}As)$ Diel. Const.	10.0710	10.0710
ω_c	Cavity Resonance Freq. (meV)	5.02	5.02

The simulation results presented below are for 165 $GaAs/Al_{0.3}Ga_{0.7}As$ MQWs embedded in the cavity core following our sample geometry. The well and the potential barrier widths are respectively chosen to be 10nm and 220nm in order to ensure strong coupling with the confined cavity modes. The choice of the materials is due to its practical applications so far reported in quantum devices. For strong interaction, the cavity width plays an important role. It is clear that the resonance

frequency of the core cavity, which determines the coupling strength, can be controlled by adjusting the cavity length $Lc = Nu\,(Lw + Lb) + L5$. Nu is the number of quantum wells in the cavity. Figure 3.4 clearly show that the cavity resonance Qc increases with decreasing the quantum well thickness. For our lOnm quantum well, we found the resonance frequency to be approximately $5.02meV$ (shown with arrow).

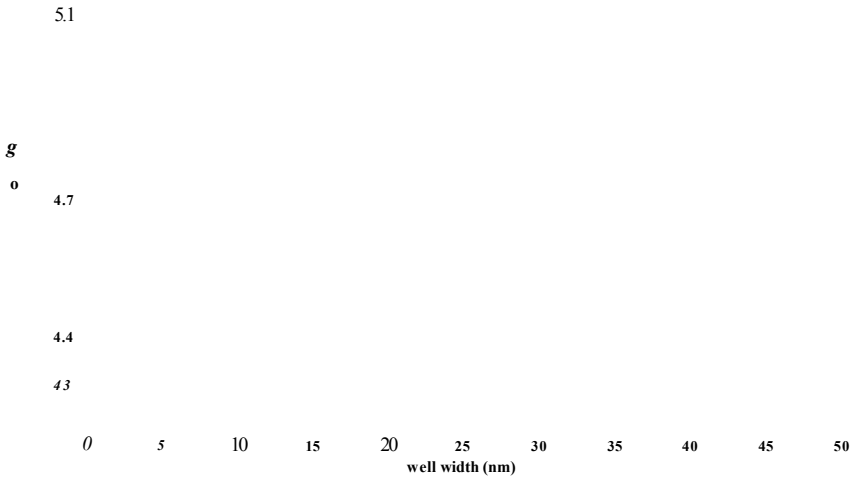

Figure 3.4' Variation of the cavity resonance with quantum well width. The arrow indicates the chosen well width and the corresponding cavity resonance for a 165 quantum wells embedded in microcavity.

To complete our sample, the AlAs layers forming the upper and lower cladding are taken 985nm and the top GaAs-layer has thickness of 5nm. In each subband of the quantum well structure, we assumed the carrier density to be independently thermalized at 300K, with population difference between initial and final subbands $AN = 2.0 \times 10^{11}\text{cm}^{2}$ for the case of an absorption (leading to a polariton) and $AN = -2.0 \times 10^{llcm^{2}}$ for inverted media (giving rise to antipolaritons). A clear anticrossing with a cavity resonance frequency at approximately 5.02 meV which is a fraction of the transition frequency (10.0 meV) is obtained, defining clearly the mixed cavity modes and material excitations. Furthermore $AflM$ reads 0.9369 and —1.2619 for the case of polaritons and antipolaritons respectively.

The energy dispersion relation as a function of incident angle *9* in the case of absorption regime is depicted in Figure 3.5 . As can be seen clearly the two branches defining the upper and lower polaritons are separated by a significant amount of energy often called vacuum Rabi-splitting [77] (« *2m,eV* in this case). The anticrossing between the two branches is clearly defined when *6* = *6res* = 57.9° (resonance angle).

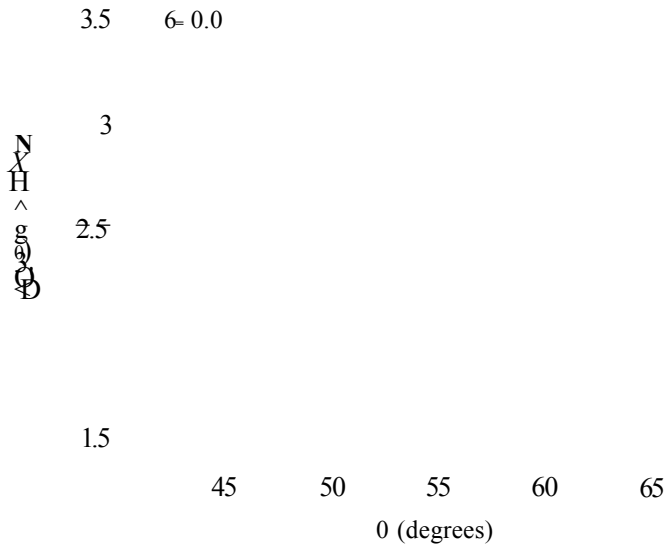

Figure 3.5: THz intervalence band polaritons obtained for the microcavity shown in Figure 3.1. In this case the first (top) valence subband is assumed to be occupied while the second (lower) subband is empty. The population density difference between the two subbands is A N —2.0 x 10n cra~2. *6 is the incident angle.*

Similar result is shown in Figure 3.6 for TE-mode THz antipolariton dispersion for the case of an inverted (gain) medium. Unlike the case of polariton, the anticrossing appeared in this case below the intersubband resonance (10.3960 meV) for for *9 < 9res* and above the resonance for *6 > 9res.*

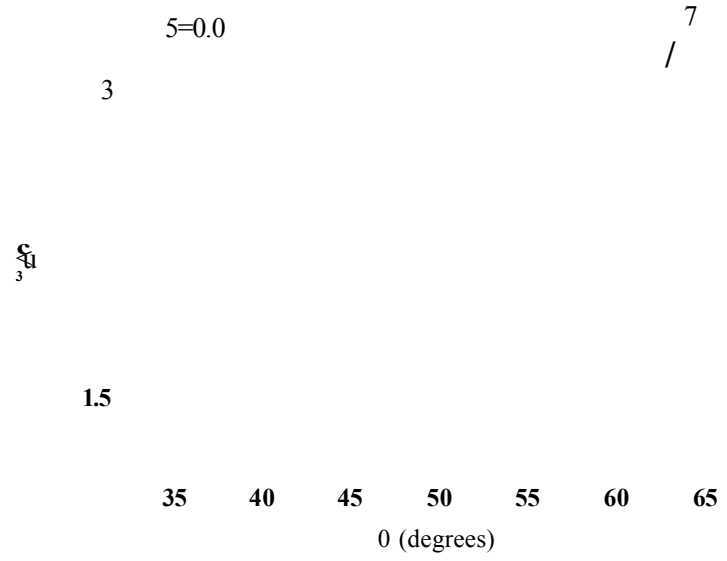

Figure 3.6: THz intervalence band antipolaritons obtained for the microcavity shown in Figure 3.1. In this case the second (lower) subband is assumed to be occupied while the first (top) subband is empty. The population difference between the two subbandds is AN = -1.0 x 10x cm-2. 9 is the incident angle.

3.5 Influence of dephasing on a single resonance

The analytical expression for the quasi-particles dispersion can be modelled to include the dephasing term *5.* The effects of dephasing has been previously investigated [93] for polaritons/antipolaritons problem in the case of electronic transitions in conduction bands for the mid infrared region. Here we applied similar techniques for holes in the valence bands extended to THz-region that allows TE-modes couplings with the intervalence band transitions.

The microcavity modes originated from the wave equation (Eq. 3.21) that is obtained from Maxwell's equation

(3.21)

For TE mode polarization, the electric field lies on the plane of incidence and an ansatz solution to Equation 3.21 can be taken as *E(r,u)* — E+(r, *oj)eL≪kr~ut'>+*

$E_o^-(r,\omega)e^{-i(\vec{k}\cdot\vec{r}-\omega t)}$. Upon substituting the electric field into the wave equation and doing some arithmetic, we arrived at the following secular equation for the coupled oscillators,

$$\begin{aligned} k_y^2 + k_z^2 &= \frac{\omega^2}{c^2}\varepsilon(\omega) \\ &= \frac{\omega^2}{c^2}\left[\varepsilon^{'}(\omega) + \varepsilon^{''}(\omega)\right], \end{aligned} \tag{3.22}$$

where k_y and k_z are the in-plane and perpendicular waves vectors, c is the speed of light in vacuum $\varepsilon'(\omega)$ and $\varepsilon''(\omega)$ are the real and imaginary parts of the dielectric function given by Equations 3.14 and 3.15 respectively. Using Equations (3.14) and 3.15 in Equation 3.22 and taking all the parameters to retain their usual meaning, Eq. (3.22) becomes;

$$\begin{aligned} \mathrm{y}^2\beta^2 + \Omega_c^2 - \frac{\mathrm{y}^4}{\Omega_c^2}\frac{1}{4}\left(\frac{\varepsilon^{''}}{\varepsilon_b}\right)^2 &= \mathrm{y}^2\left(\frac{\varepsilon^{'}}{\varepsilon_b}\right) \\ \mathrm{y}^2\beta^2 + \Omega_c^2 &= \mathrm{y}^2\left\{1 - \lambda\Delta^{'}\rho\right\}. \end{aligned} \tag{3.23}$$

On comparison, the contributions of imaginary to the real components of the dielectric function is usually small and therefore can be neglected in Equation 3.23. Finally, the polariton and antipolariton dispersion, in terms of incident angle θ, taking account the dephasing term is obtained to be;

$$\sin\theta = \left(\frac{\varepsilon_b}{\varepsilon_s}\right)^{1/2}\sqrt{1 - \lambda\rho\Delta' - \frac{\Omega_c^2}{\mathrm{y}^2}} \tag{3.24}$$

with

$$\rho = \left[\frac{\mathrm{y}-1}{(\mathrm{y}-1)^2 + \Gamma^2} - \frac{\mathrm{y}+1}{(\mathrm{y}+1)^2 + \Gamma^2}\right]$$

where we introduce $\Gamma = \frac{\delta}{\omega_o}$. Ω_c, y and Δ' as defined in the previous sections.

Figure 3.7 depicts the energy dispersion relations of polaritons for different dephasing as a function of incident angle θ. The dephasing considered is $\delta = 0.0, 0.2, 0.4, 0.6$ and 0.8 meV, which small fraction of the actual $\delta(\approx 4.5meV)$ obtained with the Lorentzian fit. The increasing dephasing tends to shrink the po-

lariton and antipolariton dispersions, as can be seen clearly with the blue color lines through the centres of both Figures 3.7 and 3.8. This effect can be reduced through the control of cavity length and carrier densities in the subbands of interest.

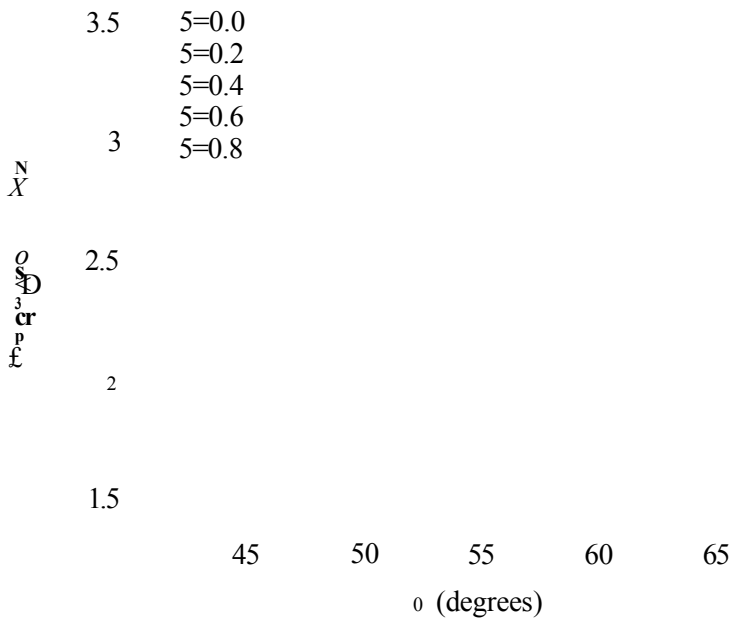

Figure 3.7: TE-mode THz Valence band polariton dispersion showing the influence of dephasing for the cavity in Fig. 3.1. As indicated, the dephasing is increased from the outer curves (pair of red lines) towards the center (single blue at the center) for δ — 0.0,0.2,0.4,0.6 *and* 0.8 *meV respectively. All curves are generated with population difference between the coupled subbands* ΔN = 2.0 x 10u cm2.

From Figures 3.7 and 3.8, we may notice that, when the dephasing increases, the polariton splitting and the non-zero detuning angle (A#) decrease. Hence, the branches are narrowed toward zero detuning (i.e resonance angle). Thus, analogously to the interband (exciton polariton) case [92], there is a critical value of the dephasing, after which the intersubband transition resonance disappears only the photon dispersion remains [93,95]. Further evidence of this effect is also reported theoretically in Ref. [96] and its experimental verification can be found in Refs. [97, 100] based on transmission, reflectivity or photoluminescence intensity measurements, where the emission intensity only appears at the cavity resonance with a single peak at large dephasing tuning.

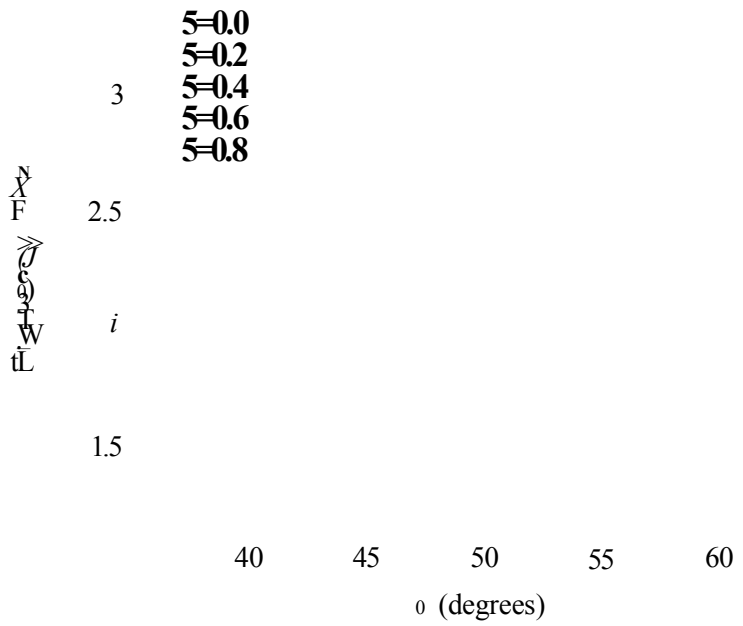

Figure 3.8: TE-mode THz Valence band antipolariton dispersion showing the influence of dephasing in the coupling of THz TE-polarized cavity modes with intervalence band excitation for the cavity described in Fig. 3.1. As indicated, the dephasing is increased from the outer curves (pair of red lines) towards the center (single blue at the center) for $S = 0.0, 0.2, 0.4, 0.6$ *and* 0.8 *meV respectively. All curves are generated with population difference between the coupled subbands* $\Delta N = 2.0 \times 10^{11} cm^2$.

3.6 Interplay between dephasing, well width and carrier density

Further application of our model Equation 3.24 derived for the polaritons and antipolaritons was achieved by considering two different samples: one containing 100A QWs and the other 50A QWs. For each sample we investigated the interplay of the carrier density in the fundamental subband and dephasing mechanism on both absorption and gain regimes.

In Figure 3.9 and 3.10, the dispersion relations of THz polaritons and antipolaritons with increasing population density are presented. In both cases, we consider an active region with 180 $GaAs/Al_{0.3}Ga_{0.7}As$ multiple quantum wells . The well and the barrier widths are lOnm and 220nm respectively, giving a total cavity length of

41.65μm including 250nm as the last barrier width. A comparison of the relevant parameters that characterize the cavities in the case of absorption regime that leads to THz valence band polaritons and inverted (gain) regime leading to THz antipolaritons are given in Tables 3.3 and 3.4 respectively for different population density (ΔN), between the coupled subbands ($\mu, \nu = 2, 1$).

Table 3.3: *Comparison of numerical values for the input/generated parameters leading to the THz polariton dispersions shown in Fig. 3.9 with increasing population density ΔN as indicated.*

Density ΔN ($\times 10^{11} cm^{-2}$)	1.0	2.0	10.0	20.0
Cavity factor λ	0.0432	0.0432	0.0432	0.0432
Background diec. constant ε_b	9.9591	9.9591	9.9591	9.9591
Cavity resonance ω_c (meV)	4.7116	4.7116	4.7116	4.7116
Resonance angle θ_{res} (^{o})	57.58	58.35	61.56	64.30
L-T Splitting Δ (meV)	0.5393	1.0103	3.7035	6.6238
ISBT-Energy $\omega_{\mu,\nu}$ (meV)	10.0125	10.2628	11.7647	13.5168
$\Lambda_{\mu,\nu}$ (meV)	5.3710	10.0624	36.8837	65.5168

The increase in carrier density compensates the effects of the dephasing as can be seen in Figures 3.10(d) and 3.11(d) for both polaritons and antipolaritons cases. In other words, the tendency to recover the polaritons and antipolaritons features is more pronounced if the dephasing is kept minimal for a given carrier density. Moreover, the polariton and antipolariton splitting increases with the increasing the carrier density as in Figure 3.9 (a) to (d) for constant value of dephasing, which implied that dephasing can be reduced by injecting more carriers. However we may notice from Figure 3.9 (d) that the polariton character can only be maintained for a reasonable doping concentration.

To move further, we studied the effect of changing the quantum well thickness in the polaritons and antipolaritons dispersion relations. We performed simulations with two different samples in the core cavity of the proposed geometry shown in the previous sections: First we consider the sample to have 100Å QWs width and the

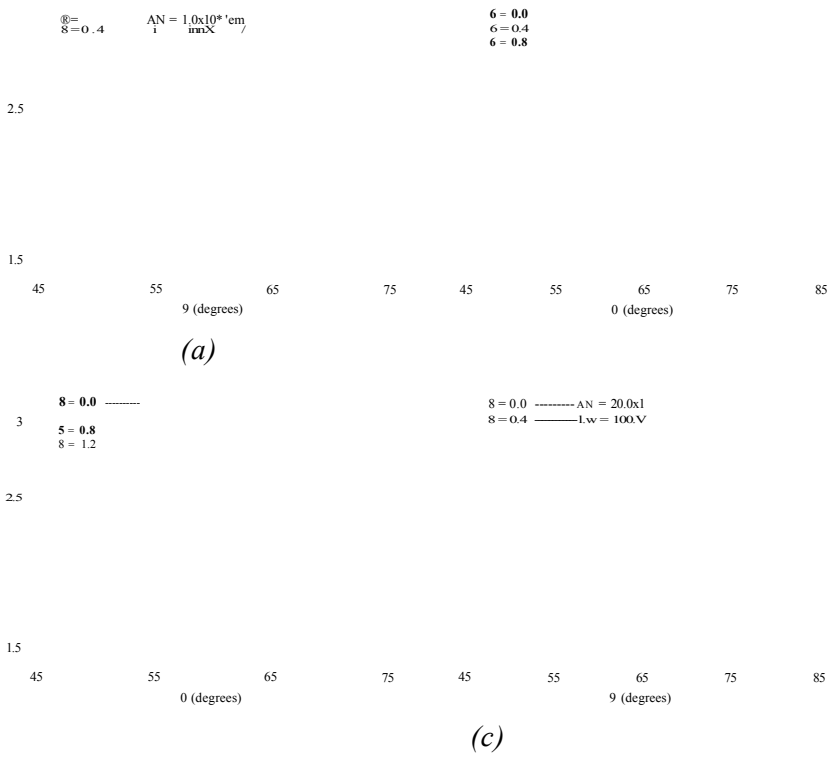

Figure 3.9: THz valence band polariton dispersions for a lOOAQW as a function of incident angle 9 for different population densities A N as indicated from (a) to (d). The effect of dephasing on the polariton dispersions is compensated by increasing the occupation of the subbands. The polariton character is maintained even at high value of dephasing with high doping concentrations as can be seen in (d).

second having 50A QWs. In same manner as presented above, we summarized the numerical values of the input and other relevant parameters that are obtained from the simulation results in tables 3.5 for the case of absorption and 3.6 for the case of gain regime. In the case of polaritons, the decrease in the quantum well thickness increases the cavity resonance and likewise the coupling strength becomes stronger which leads to large polaritons splitting (A T h i s is expected due to quantum confinement as the barrier widths are kept constant for the two different samples.

For the case of antipolaritons (gain medium), A^M becomes more negative for Lu = 50A and continues to increase negatively with increasing the density (see table 3.6). The polariton and antipolariton dispersions resulting from the simulations of these cavities are presented in Figures 3.11 and 3.12 respectively, showing the

Table 3.4-' Comparison of numerical values for the input/generated parameters leading to the THz antipolariton dispersions shown in Figure 3.10 with increasing population density AN as indicated.

Density AN (x1O*n cm~2)*	-1.0	-2.0	-4.0	-6.0
Cavity factor A	0.0432	0.0432	0.0432	0.0432
Background diec. constant	9.9591	9.9591	9.9591	9.9591
Cavity resonance *OIC* (meV)	4.7116	4.7116	4.7116	4.7116
Resonance angle *0res (°)*	55.25	53.45	49.14	42.42
L-T Splitting A (meV)	-0.6585	-1.2730	-2.5699	-3.7308
ISBT-Energy *C J* (meV)	9.2615	8.7609	7.7596	6.7584
N^v (meV)	-6.5583	-12.6784	-25.5945	-37.1557

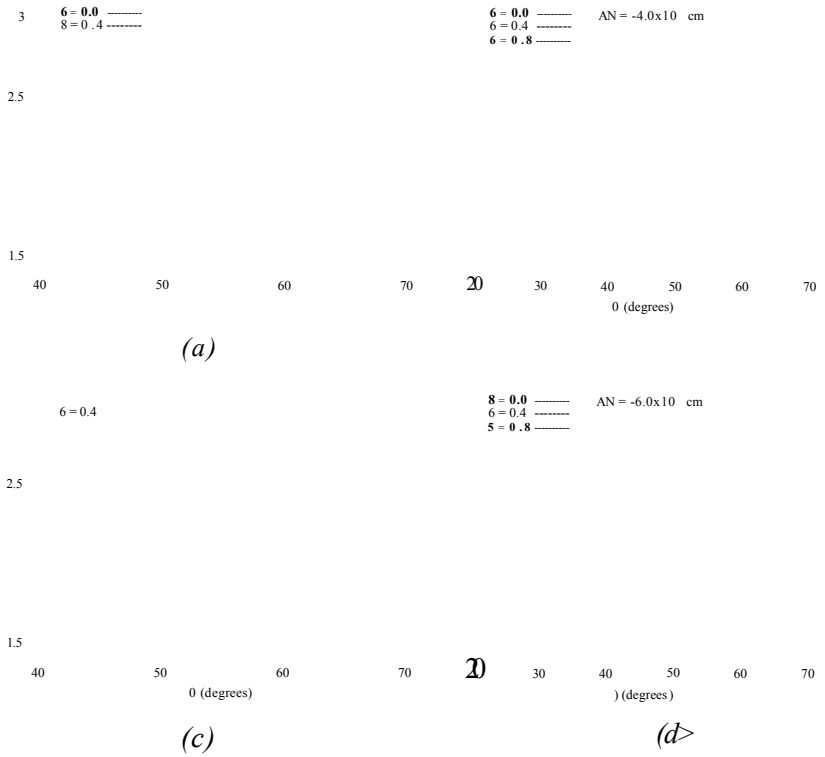

Figure 3.10: THz valence band antipolariton dispersions for a 100A QWs as a function of incident angle 0 for different carrier density AN as indicated from (a) to (d). The effect of dephasing on the polariton dispersion is compensated by increasing the occupation of the subbands.

Table 3.5: *Parameters used in the simulations delivered in Fig. 3.11 for two different well widths ($L_\omega = 100Å$ and $L_\omega = 50Å$) at different occupancy ΔN for the case of an absorption.*

Quantum well width(Å)	100		50	
Density ΔN ($\times 10^{11} cm^{-2}$)	1.0	2.0	1.0	2.0
Cavity factor λ	0.0432	0.0432	0.0220	0.0220
Background diec. constant ε_b	9.9591	9.9591	9.9384	9.9384
Cavity resonance ω_c (meV)	4.7116	4.7116	4.8206	4.8206
Resonance angle θ_{res} (^{o})	57.58	58.23	68.63	68.68
L-T Splitting Δ (meV)	0.5393	1.0103	0.6439	1.2532
ISBT-Energy $\omega_{\mu,\nu}$ (meV)	10.0125	10.2628	21.5269	21.7722
$\Lambda_{\mu,\nu}$ (meV)	5.3710	10.0624	6.3998	12.4554

Table 3.6: *Parameters used in the simulations delivered in Fig. 3.12 for two different well widths ($L_\omega = 100Å$ and $L_\omega = 50Å$) at different occupancy ΔN for the case of gain*

Quantum well width(Å)	100		50	
Density ΔN ($\times 10^{11} cm^{-2}$)	-1.0	-2.0	-1.0	-2.0
Cavity factor λ	0.0432	0.0432	0.0220	0.0220
Background diec. constant ε_b	9.9591	9.9591	9.9384	9.9384
Cavity resonance ω_c (meV)	4.7116	4.7116	4.8206	4.8206
Resonance angle θ_{res} (^{o})	55.25	53.45	68.04	67.68
L-T Splitting Δ (meV)	-0.6585	-1.2730	-0.8515	-1.6303
ISBT-Energy $\omega_{\mu,\nu}$ (meV)	9.2615	8.7609	20.2753	19.5244
$\Lambda_{\mu,\nu}$ (meV)	-6.5583	-12.6784	-8.4634	-16.20394

variations of frequency in THz with the incidents angle θ. Nevertheless, it was noticed that, the resonance angle θ_{res} (corresponding angle of incidence at which the cavity resonance and material's excitations interact) is shifted to a higher value as the quantum well thickness is reduced. However, increasing the population density reduces the resonance angle (see Tables 3.5 and 3.6). This is true for both polaritons and antipolaritons.

As can be seen from left to right of Figure 3.11, at constant dephasing and

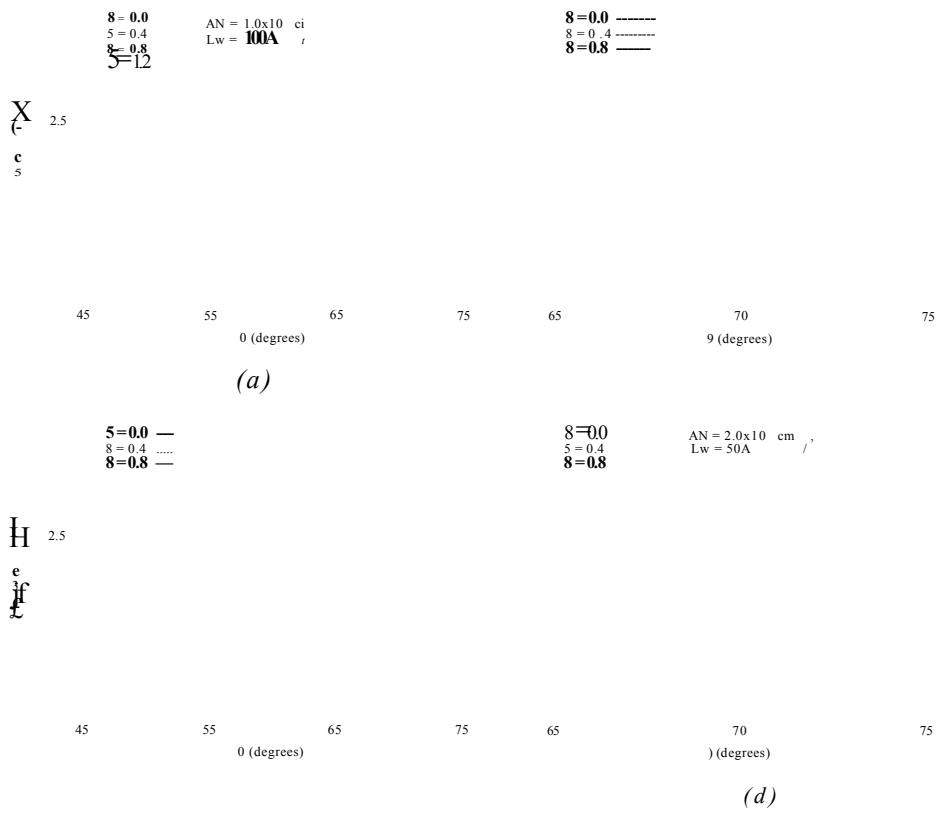

Figure 3.11: THz intervalence band polaritons due to coupling of TE polarized cavity modes and intervalence band excitations for 100A MQWs ((a) and (c)) compared with 50A MQWs ((b) and (d))showing the interplay between dephasing for a given a quantum well width and population difference for the case of single transition (fi, v = 1,2).

population density, the polaritons features are more pronounced when the quantum well width is small(i. e. with = 50A in this case). The same effect can be notice for the case of antipolaritons presented in Figure 3.12.

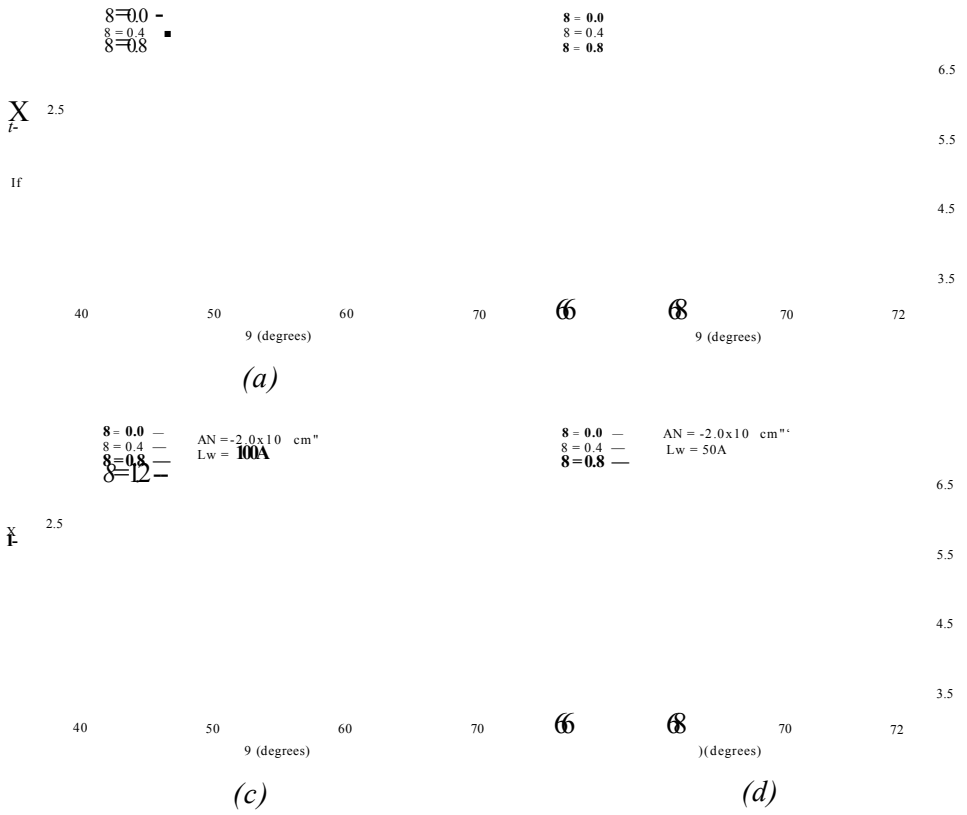

Figure 3.12: THz intervalence band antipolaritons due to coupling of TE polarized cavity modes and intervalence band excitations for 100A MQWs ((a) and (c)) compared with 50A MQWs ((b) and (d)) showing the interplay between dephasing for a given a quantum well width and population difference between coupled subbands for the case of single transition (li,v = 1,2).

3.7 Relevance of controlling the cavity length

The results presented in this section indicate the significance of controlling the cavity for achieving better defined inter-valence band THz polariton and antipolariton features. In this approach, we consider a cavity with 50A MQws having the population density difference between the coupled subbands $\Delta N = \pm 1.0 \times 10^{n}\ cm^{-2}$ (in case of absorption or gain regimes). We play with the cavity length by varying the number of quantum wells in the core region and kept dephasing constant and compared it influences. For the numerical values of the input parameters see Tables 3.7 and 3.8 which leads to delivering of the THz polaritons and antipolaritons dispersion presented in figures 3.13 and 3.14 respectively.

Table 3.7: *Parameters for cavities with 50Å QWs in the core cavity and fixed carrier density* $\Delta N = 1.0 \times 10^{11} cm^{-2}$ *for various cavity length due to the variation in number of quantum wells in the cavity for the case of polaritons.*

Number of quantum wells	90	130	170
Cavity length (μm)	14.2	20.4	26.6
Cavity factor λ	0.0316	0.0318	0.0319
Background diec. constant ε_b	10.09	10.09	10.09
Cavity resonance ω_c (meV)	13.72	9.55	7.30
Resonance angle θ_{res} (^{o})	47.90	59.60	64.80
L-T Splitting Δ (meV)	0.64554	0.64554	0.63417
ISBT-Energy $\omega_{\mu,\nu}$ (meV)	21.5269	21.5269	21.5269
$\Lambda_{\mu,\nu}$ (meV)	6.3998	6.3998	6.3998

From both Figures. 3.13 and 3.14, we can see that increasing the cavity width (from (a) to (c)) shifts the resonance angle to higher values (see tables 3.7 and 3.8). The polariton splitting also increases with increasing cavity length. Furthermore, more quantum wells increase the effective total oscillator strength and thus increase the polariton splitting.

Table 3.8: *Parameters for cavities with 50Å QWs in the core and fixed carrier density* $\Delta N = 1.0 \times 10^{11} cm^{-2}$ *for various cavity length due to the variation in number of quantum wells in the cavity for the case of antipolaritons.*

Number of quantum wells	90	130	170
Cavity length (μm)	14.20	20.40	26.60
Cavity factor λ	0.0316	0.0318	0.0319
Background diec. constant ε_b	10.09	10.09	10.09
Cavity resonance ω_c (meV)	13.72	9.55	7.30
Resonance angle θ_{res} (^{o})	45.09	58.04	64.95
L-T Splitting Δ (meV)	-0.8386	-0.8386	-0.8386
ISBT-Energy $\omega_{\mu,\nu}$ (meV)	20.2753	20.2753	20.2753
$\Lambda_{\mu,\nu}$ (meV)	-8.4634	-8.4634	-8.4634

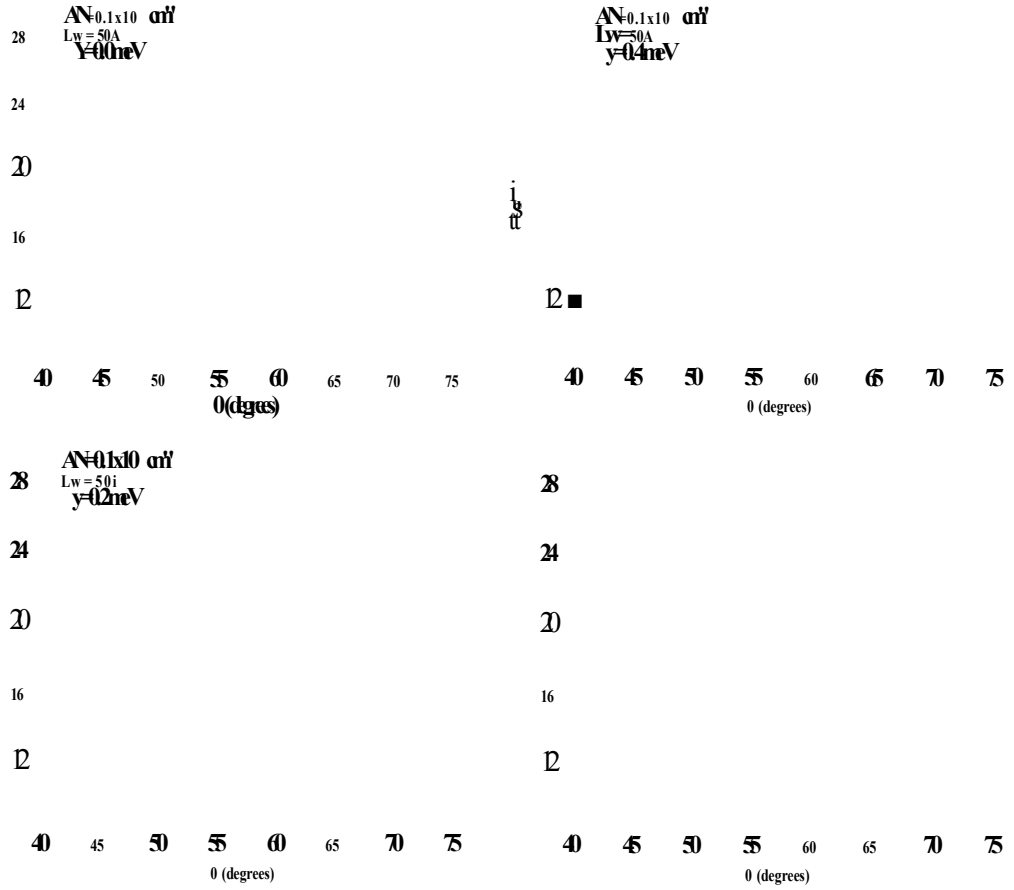

Figure 3.13: THz intervalence band polariton dispersion relations for 50A QWs and fixed carrier population difference AN— 1.0 x 10n cm~2 with changing cavity width and dephasing in each case. As can be seen the larger cavity with more quantum wells accommodates more dephasing.

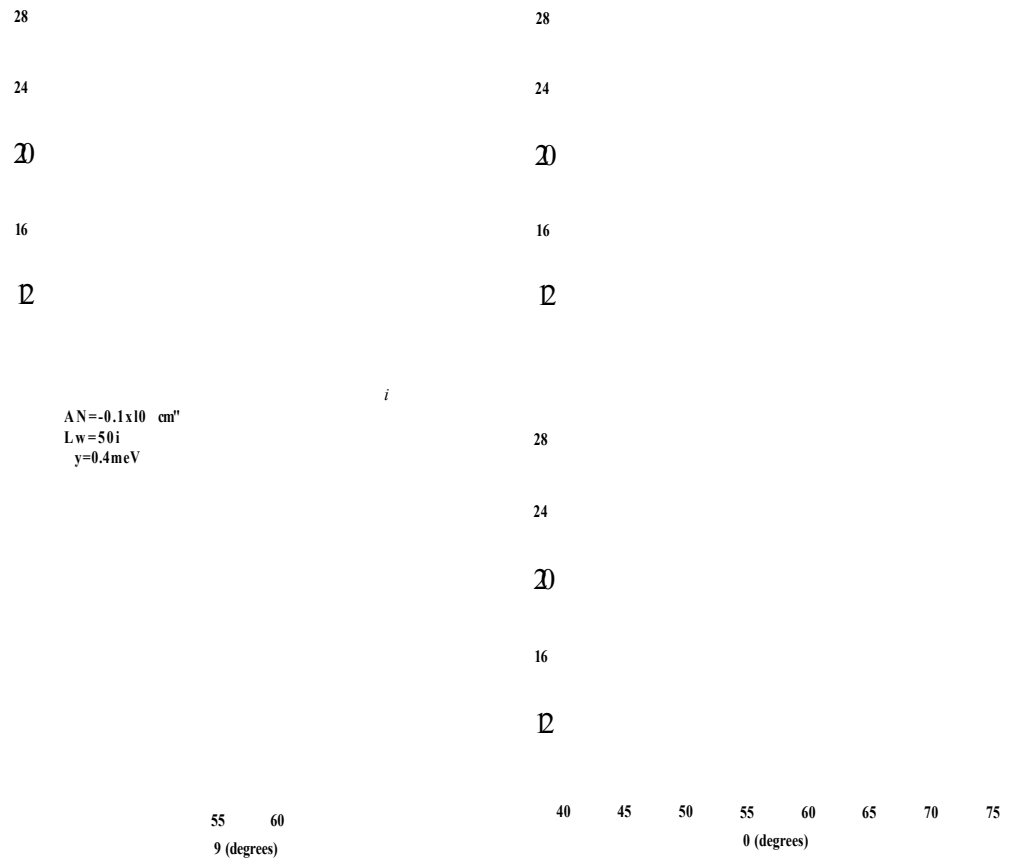

Figure 3.14: THz intervalence bands antipolariton dispersion relations for 50A QWs and and fixed carrier population difference AN— —1.0 x 10n cm~2 with changing cavity width and dephasing in each case. As can be seen the larger cavity with more quantum wells accommodates more dephasing.

3.8 Conclusion

To conclude this chapter, analytical expressions for the energy dispersion relations of polaritons and antipolaritons have been derived. For a given geometric structure and using a simple formula based on the dielectric function formalism, the interaction of valence bands excitations with TE THz cavity modes was investigated. The relevance of valence band based designed to study light-matter interactions and possibilities of THz emission to be realized is shown. By considering single transitions due to absorption and inverted medium polaritons and antipolaritons can be measured by controlling the dephasing to certain limits. On further increase, the materials excitations are no longer visible, Only the photons branch remain. This is analogous to the case of interband excitons polaritons.

The effects of dephasing and increasing carrier densities as well as the interplay between quantum well width and the cavity length were also investigated. The resulting TE-mode THz polariton and antipolariton dispersions shows that, the contrast of the polaritons and antipolaritons can be controlled even at high dephasing by increasing the density of populated subbands, or reducing the quantum well width or increasing the number of quantum wells in the core cavity, thereby increasing the coupling strength.

The approach presented also has the potential to to deliver THz polaritons and antipolaritons using simple design based on coupling TE-modes THz radiation and valence band excitations, unlike the conduction band case which require complex geometric and TM-mode cavity resonances. A nonequilibrium optical many body approach of the optical response beyond the Hartree Fock approximation is used as input to the effective dielectric formalism.

CHAPTER 4
POLARITONS AND ANTIPOLARITONS DUE TO MULTIPLE RESONANCE

4.1 Introduction

In the previous chapter, we investigated the coupling of intervalence band excitations and TE-mode polarized cavity modes, by considering only one possible transition among the valence-subbands. In the present chapter the formalism is extended to cover multiple transitions where optical gain and cross-absorptions to higher subbands are possible due to hole transitions to higher subbands. Our proposed geometric structure described in the previous chapter is also maintained in this case.

4.2 Input parameters/optical constants

We have computed the relevant parameters used as input, similar to the single transition case presented in the previous chapter. The full optical susceptibility given by Equation (4.1) is approximated to a Lorentzian fit each for **N** number of individual optical transitions, where $\mathbf{N} = 3$ in this case. Table 4.1 below summarizes the input parameters extracted in this method for each individual transition,

$$\chi(\omega) = 2 \sum_{q \neq q', \vec{k}} d_{q,q'} \chi_{q \neq q'}(k, \omega), \tag{4.1}$$

where $d_{q,q'}$ is the intersubband transition dipole moment between subbands $q = 2$ and $q' = 1, 3, 4$. Thus for $q = 2, q' = 1$, we have one single transition named (2-1) transition. Likewise we have (2-3) and (2-4) transitions.

The susceptibility function on the right side of Equation 4.1 is numerically evaluated through Keldysh nonequilibrium many body Green's function as for the case of a

Table 4.1: Parameters used as input to deliver simulations leading to THz polariton/antipolaritons due to multiple transitions.

Parameter	Transition Type		
	2-1 (Gain)	2-3 (Abs)	2-4 (Abs)
Well width (nm)	10.0		
Barrier width 1/2 (nm)	200/250.0		
No. of quantum well	150.0		
Top-layer (nm)	5.0		
AlAs-Cladding (nm)	2300.0		
ISBT-Energy $\omega_{q,q'}$ (meV)	8.7609	25.2816	41.8022
Coupling factor Λ (meV)	-12.7535	8.0303	3.6546

single transition with the only difference here being that three different transitions are considered between the chosen four valence subbands.

4.2.1 The optical susceptibility

The full numerical solution of the nonequilibrium optical susceptibility for each transition is adjusted to the Lorentzian fit approximation for all transitions given by [94] ;

$$\chi(\omega) = -\frac{1}{4\pi}\sum_{q\neq q'}\left\{\frac{\Lambda_{q,q'}}{\omega-\omega_{q,q'}+\delta_{q,q'}} - \frac{\Lambda_{q,q'}}{\omega+\omega_{q,q'}+\delta_{q,q'}}\right\}, \tag{4.2}$$

where $\Lambda_{q,q'}$ can be positive or negative depending on whether absorption or gain regime is being considered. $q = 2, q' = 1, 3, 4$ are the chosen subbands while ω and $\omega_{q,q'}$ are the photons and adjusted transitions energy between q, q' respectively. In Fig. 4.1 the the combined optical susceptibility for all relevant transition and for each individual contribution are compared.

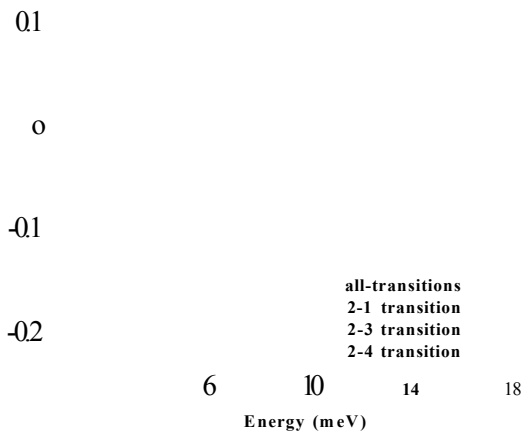

(a) NGF-calcultaion

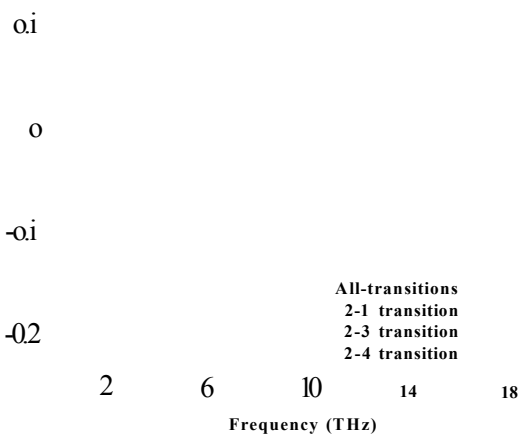

***(b)** BWA-Lorentzian fit*

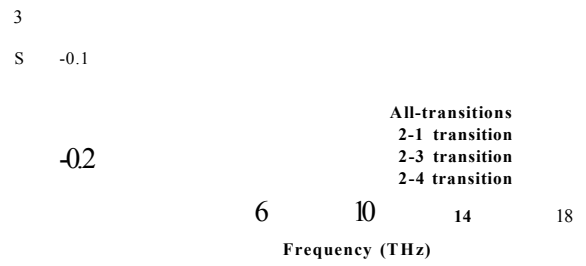

(c) Full-calculation

Figure 4-1• Combined optical susceptibility for all relevant transitions (solid, red) and each individual contribution: 2-1 (dotted blue line) gain, 2-3 (green dot-dashed) absorption and 2-4 (black double-dotted-dash) absorption in which the second subband is occupied with $N = 2.0 \times 10^{11} cm^2$ and all other subbands are empty, (a) NGF-Calculation, (b) Lorentzian Fit approximation and (c) Full Lorentzian including both rotating and non rotating terms.

4.2.2 Energy dispersion relations and mathematical models

Within the dielectric medium approach, the dispersion relations are derived from the wave equation which resulted from Maxwell's equation as in the previous chapter(chapter 3). The dielectric constant of the medium $\varepsilon(\omega)$ and the susceptibility function described above are connected through the equation ;

$$\varepsilon(\omega) = \varepsilon_b + 4\pi\lambda\chi(\omega) \tag{4.3}$$

with ε_b and λ being the background dielectric function and cavity anisotropic factor defined in the previous chapter. Following the same approach as with single transition, the polaritons and antipolaritons dispersions is given by microcavity mode equation;

$$k_y^2 + k_z^2 = \frac{\omega^2}{c^2}\varepsilon(\omega) \tag{4.4}$$

with equation 4.3 and is given by;

$$\sin^2\theta = (\varepsilon_b/\varepsilon_s)\left(1 - 4\pi\lambda Re\left\{\chi(\omega)/\varepsilon_b\right\} - \omega_c^2/\omega^2\right), \tag{4.5}$$

where ω_c is the cavity resonance frequency and θ is the incident angle. Note that Re in 4.5 referred to real part.

4.3 Numerical results and discussion

We start by presenting the result without dephasing ($\delta = 0.0$ meV). Simulation are performed with 150 $GaAs/Al_{0.3}Ga_{0.7}As$ quantum wells in the cavity region of our proposed structure. As shown in Table 4.1, the cavity length used is 31.74μm and the cavity resonance is $\omega_c \approx 6.17$ meV (0.98 THz) for a chosen resonance frequency ω_o of 10.05 meV ($\approx$ 1.6THz). The background dielectric constant ε_b and the anisotropic constant λ are found to be 9.9631 and 0.0472 respectively. The upper and lower polariton splitting described by the absorptions regimes are characterized with L-T splitting $\Delta \approx 0.8060$ and 0.3668 MeV (0.128 and 0.0584 THz) and it equivalent reads -1.2751 meV (0.2029 THz) for inverted medium.

Figure 4.2 dipicts the Energy dispersion relations for the TE-mode valence band THz polaritons and antipolaritons as function of incident angle due to multiple transition (3 in this case). The polariton/antipolaritons dispersion in the this case is totally different from the sum of individual transition (a) to (c), owing to the strong interaction and repulsion of the branches leading to an exciting scenario (d).

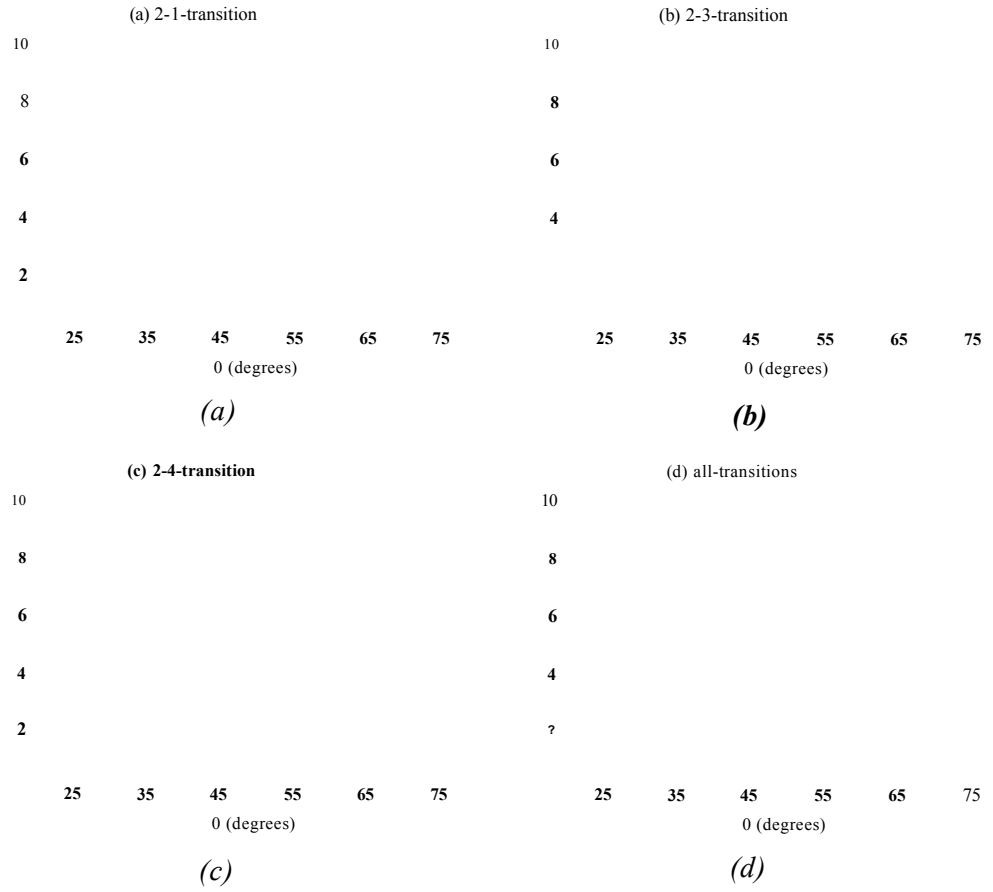

Figure J^.2: THz valence band polaritons/antipolaritons based on TE-mode coupling of THz radiation and intervalence band excitations corresponding to the transitions: 2-1 (a), 2-3 (b), 2-4 (c) and combination of all (d) using multiple transitions Equation 4-3. In all cases the carriers densities are independently thermalized at 300 K in the second subband with density $N = 2.0 \times 10^{n}\ cm^{-2}$ *and all other subbands are empty. The dephasing is neglected.* $S = 0.0\ meV$

4.4 Effects of dephasing and scattering mechanism on multiples transitions

In order to see the influence of the intersubbands broadening term (dephasing) on the polariton/antipolariton dispersions for the multiple transition case, we have performed simulations for different values of *5,* ranging from 0.0 to 1.2 meV. The energy dispersions are clearly visible on tuning the broadening until eventually it reaches a significant value, where the antipolaritons feature completely disappear [99] analogously to the case of single resonance and exciton polaritons [100] case.

Figure 4.3 shows the the coexisting and interacting polariton and antipolariton dispersions (a) - (f) for a lOnm MQWs with the same barriers width and inputs parameters listed in table 4.1 (in the previous section) above with dephasing *5* = 0.0, 0.2, 0.4, 0.6, 0.8 and 1.2 meV respectively. The chosen values of dephasing are quite small compared to the actual value obtained ~ 4.7, 4,8 and 8.7 meV, for 2-1, 2-3 and 2-4 transition respectively. Clearly the dephasing can be seen to effect the dispersions with lower resonance transition due to inverted (active) gain medium, as it seem to disappeared even with small dephasing (£ = 0.2 meV). This implies that scattering and dephasing mechanism are more likely to easily switch off the process if the medium is inverted. Thus, its experimentally more difficult to achieve strong population inversion in the THz range as in the case of quantum cascade lasers (QCLs) [101-103].

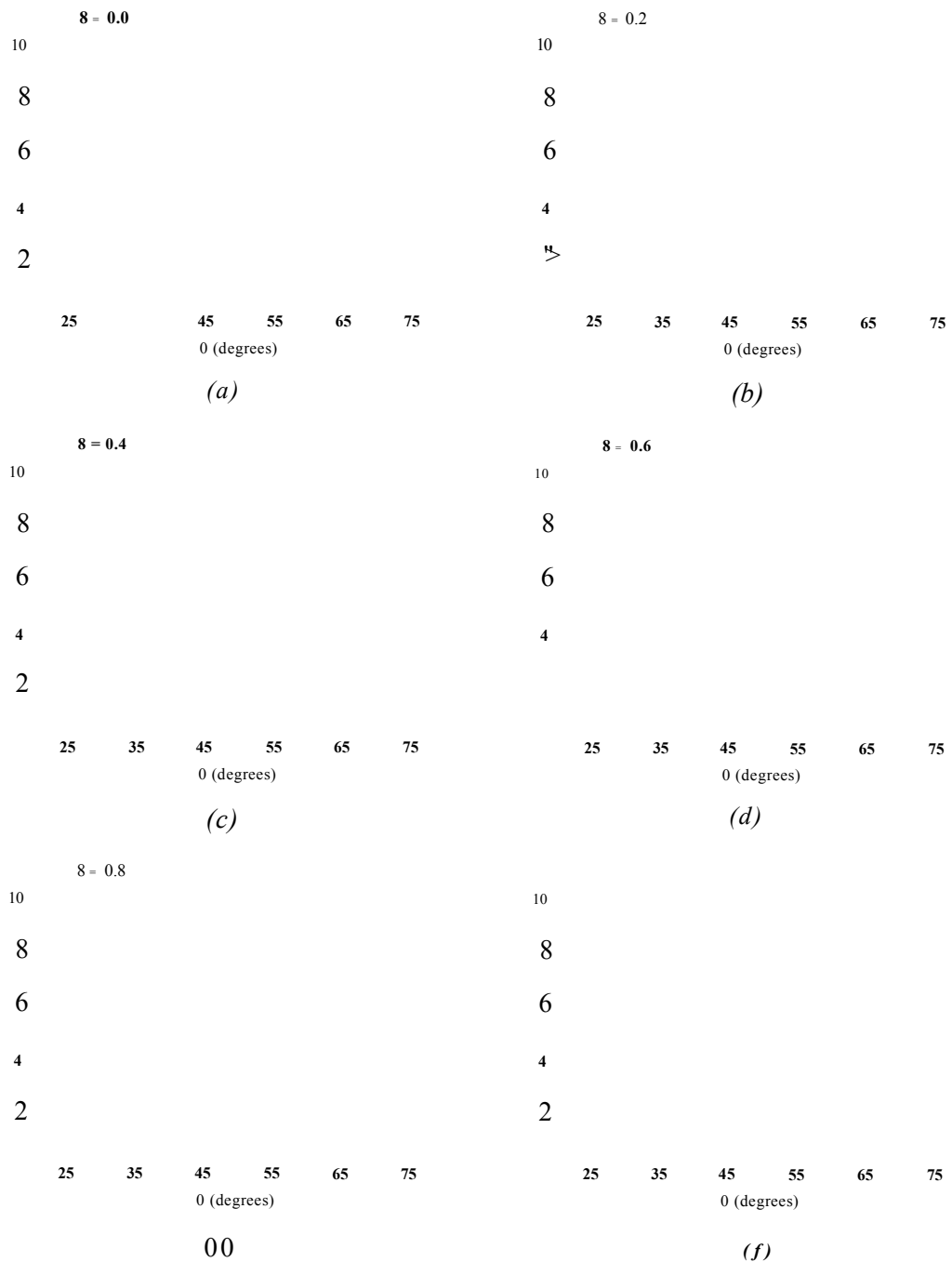

Figure 4-3: Interacting THz polaritons and antipolaritons resulting from coexisting gain and absortions to higher subbands, in a structure containing 10 nm GaAs/Alo^GaojAs quantum wells in the cavity core with increasing dephasing 5 (from (a) to (f))as indicated. The effect of dephasing can be clearly seen in (f) where large dephasing 5 = 1.2 meV strongly reduces the polariton and antipolariton dispersions.

In figure 4.5 and 4.5, we show the THz polariton and antipolaton dispersions of the $10nm$ MQWs with multiple transitions for different cavity lengths due to changing barrier width and number of quantum wells **N** in the cavity. To clearly see the effects of cavity, we have presented in both cases the energy dispersion relations verses the incident angle θ for $\delta = 0.0$ and 0.2 meV. Table 4.2, 4.3 and 4.4 below compare the input and relevant parameters computed in simulating the structure with 150, 170 and 200 MQWs in the core cavity and varying barrier thickness.

Table 4.2: *Parameters for the multiple transition problem with increasing cavity using 150 MQWs and varying barrier width*

Parameter	Numerical Value		
Barrier width L_b (nm)	175	200	225
Cavity length (μm)	27.99	31.74	35.49
Cavity Res. ω_c (meV)	7.0048	6.11794	5.5280
Cavity factor λ	0.05357	0.04724	0.04225
Background Die. const. ε_b	9.9694	9.9631	9.9582
L-T splitting $\Delta_{\mu,\nu}$ (meV)	-1.2792	-1.2800	-1.2807
	0.8056	0.8060	0.8064
	0.3665	0.3668	0.3670

We notice from Figure 4.4a that, increasing the cavity by increasing the number of quantum well and barrier width constant, there is shift in resonance angle θ_res to higher values and slightly increases the polaritons and antipolaritons splitting, which can be verified in Table 4.2 . A similar effect is obtained by changing the barrier width, since in both cases, the total effective cavity length is changed (compare $\Delta_{\mu,\nu}$ values for the same colons in Table 4.2 - 4.4 . Next a comparison between TE and TM modes valence band polariton and antipolariton is considered.

Table 4.3: *Parameters for the multiple transition problem with increasing cavity using 170 MQWs and varying barrier width*

Parameter	Numerical Value		
Barrier width L_b (nm)	175	200	225
Cavity length (μm)	31.69	35.94	40.19
Cavity Res. ω_c (meV)	6.1872	5.4575	4.8817
Cavity factor λ	0.05367	0.04728	0.04228
Background Die. const. ε_b	9.9694	9.9631	9.9582
L-T splitting $\Delta_{\mu,\nu}$ (meV)	-1.2792	-1.2800	-1.2807
	0.8056	0.8060	0.8064
	0.3665	0.3668	0.3670

Table 4.4: *Parameters for the multiple transition problem with increasing cavity using 200 MQWs and varying barrier width*

Parameter	Numerical Value		
Barrier width L_b (nm)	175	200	225
Cavity length (μm)	37.24	42.24	47.24
Cavity Res. ω_c (meV)	5.2654	4.637	4.1533
Cavity factor λ	0.05369	0.04733	0.04232
Background Die. const. ε_b	9.9694	9.9631	9.9582
L-T splitting $\Delta_{\mu,\nu}$ (meV)	-1.2792	-1.2800	-1.2807
	0.8056	0.8060	0.8064
	0.3665	0.3668	0.3670

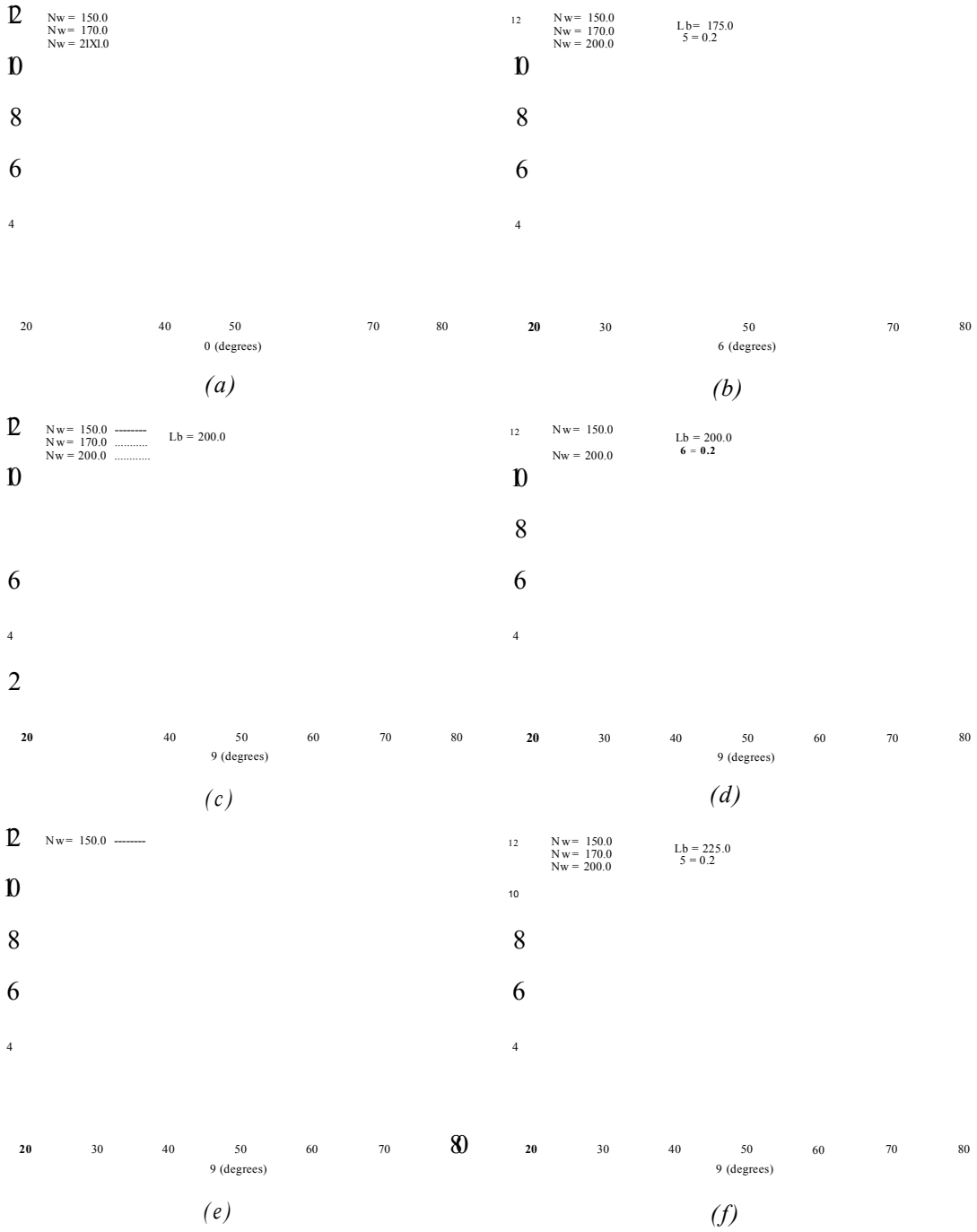

Figure 4'4: Valence band polaritons/antipolaritons due to multiple transitions with increasing cavity due to the constant barriers and varying number of quantum wells. Figures on the left hand side are obtained with zero dephasing $S = 0.0meV$ *while those on the right hand side with small dephasing* $5 — 0.2\ meV$ *for comparison.*

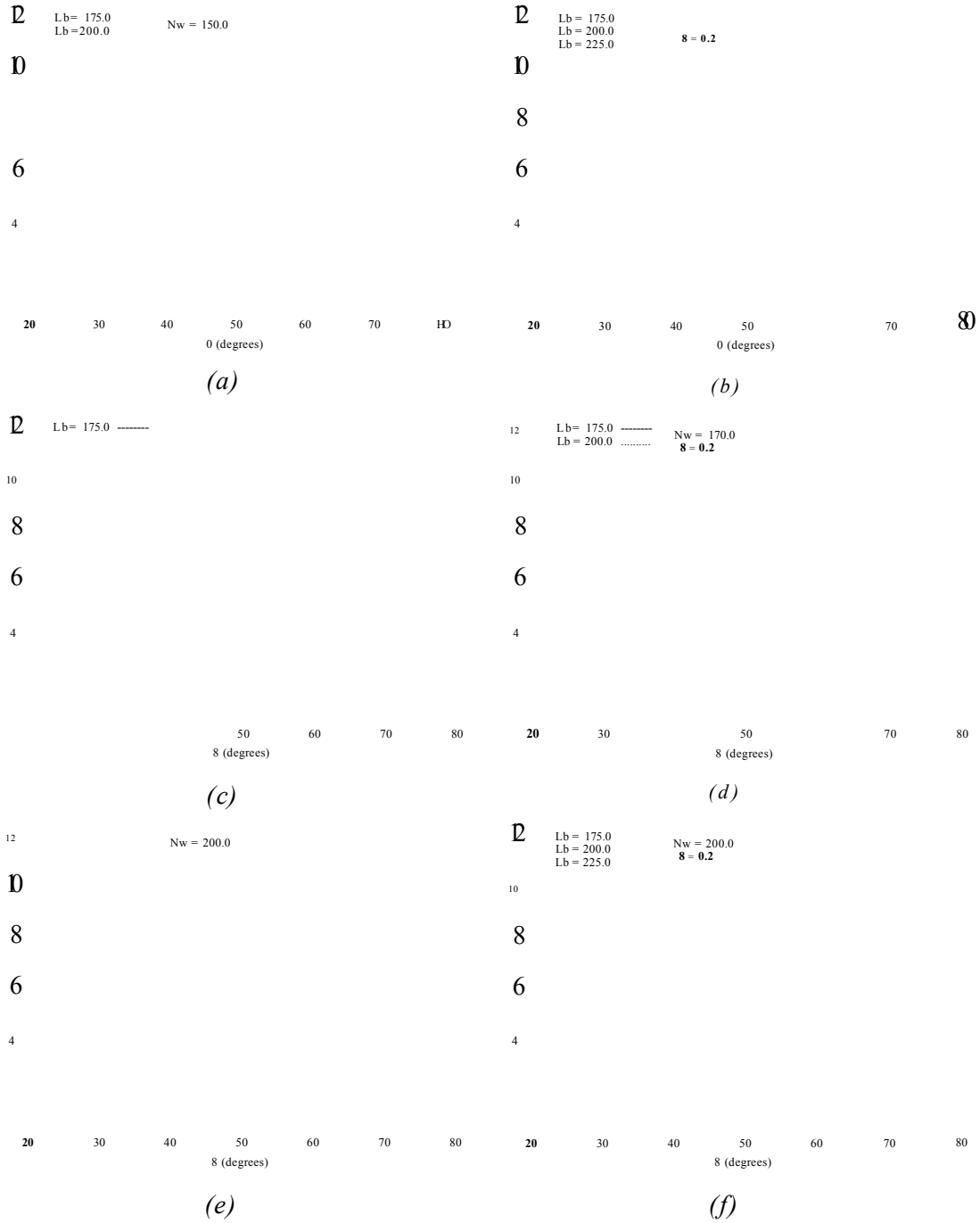

Figure 4-&: Valence band polaritons/ antipolaritons due to multiple transitions with increasing cavity by keeping the number of quantum well in the core cavity constant and varying the barrier width. Figures on left hand side are obtained with zero dephasingd = 0.0 meV while those on the right hand side with small dephasing 6 = 0.1 meV for comparison

4.5 Comparison of TE and TM modes for valence band THz polaritons and antipolaritons

The fact that valence subband transitions can be coupled with both TE and TM modes polarized cavity modes, stimulates to extend our studies by comparing results obtained for THz polaritons and antipolaritons for the two possible modes. The energy dispersions are obtained as described in the the previous sections of this chapter. However due to dipole dependent on k vector, the dipole moment matrix element for the cases are not the same. Note also that, the projection of the electric field also changes from TE to TM. To make it clear, we recall Eq. 3.10 for the TE case which read

$$\chi(\omega) = -\frac{1}{4\pi}\frac{\Lambda}{\omega - \omega_1 + i\delta} \tag{4.6}$$

and for TM case we have Λ replace by $\Lambda\ sin^2\theta_b$. Therefore

$$\chi(\omega) = -\frac{1}{4\pi}\frac{\Lambda sin^2\theta_b}{\omega - \omega_1 + i\delta}, \tag{4.7}$$

where θ_b is propagation angle inside the cavity.

We compare below, the optical susceptibilities obtained with full Lorentzian formula, by adjusting the NEGF-solution using the Lorentzian approximation (RWA-only) for the TE and TM modes. In Figure 4.7a the population density difference is, $\Delta N = 1.0 \times 10^{11} cm^{-2}$ corresponding to absorption and in Figure 4.7b $\Delta N = -1.0 \times 10^{11} cm^{-2}$ corresponding to gain respectively. Similar results are displaced in Figure 4.7a with $\Delta = 2.0 \times 10^{11} cm^{-2}$ and in Figure 4.7a with $\Delta = -2.0 \times 10^{11} cm^{-2}$. It is clear from both figures that there is shift in resonance position (corresponding frequency at maximum peak) in the TM case. This is due to the strong k-dependence on the dipole moment, which samples different region of k-space for TE and TM [85,98].

Next we compare and contrast the corresponding polariton and antipolariton dispersions.

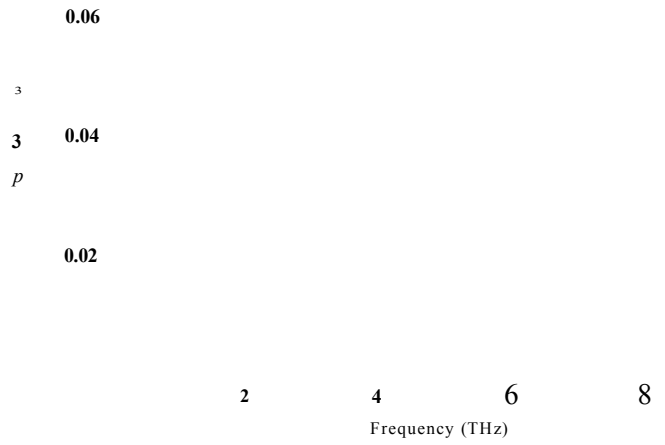

(a)

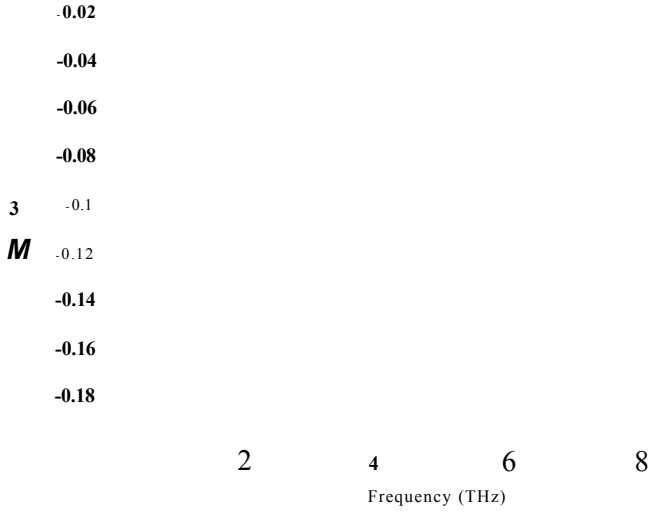

(b)

Figure 4-6: Full Lorentzian Fit including rotating and counter-rotating wave terms for a 100A GaAs/AlGaAs quatum well. The population difference between the subbads in (a) is A N = 1.0 x 10n cm~2 and (b) is A N = —1.0 x 10n cm~2

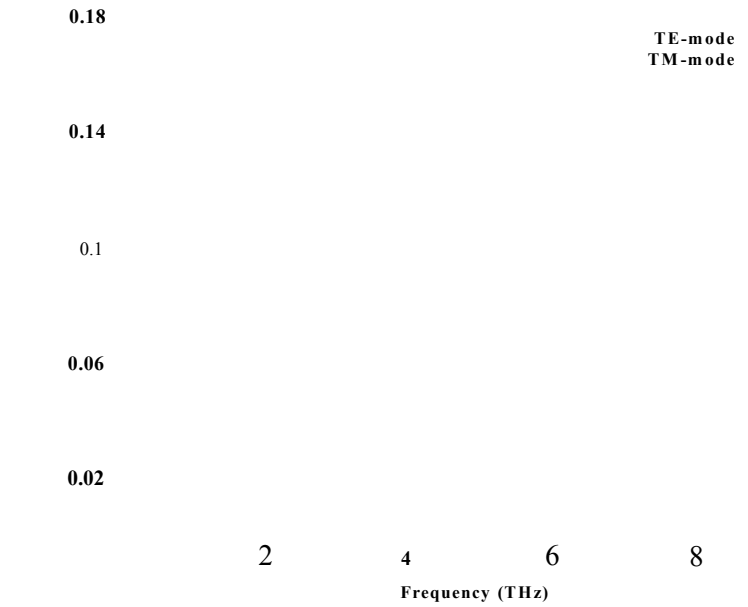

(a)

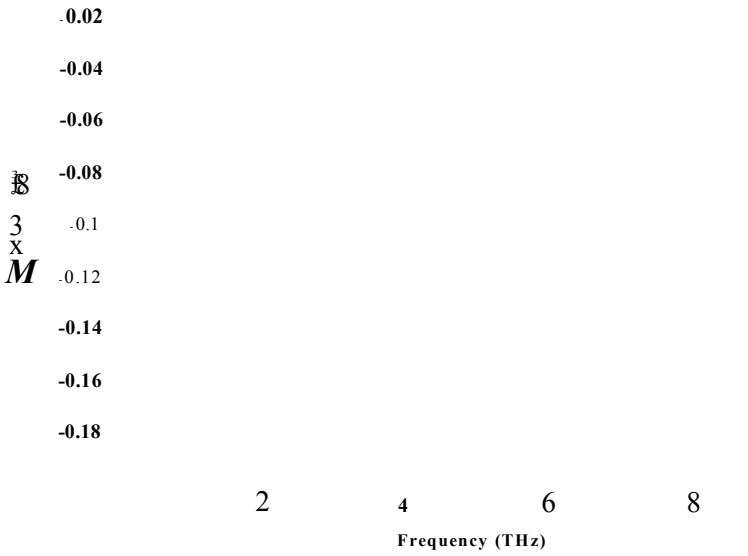

(b)

Figure f.7: Full Lorentzian Fit including rotating and counter-rotating wave terms for a 100A GaAs/AlGaAs quatum well. The population difference between the subbads in (a) is ΔN —2.0 x 10u cm~2 and (b) is ΔN ——2.0 x 10n cm-2.

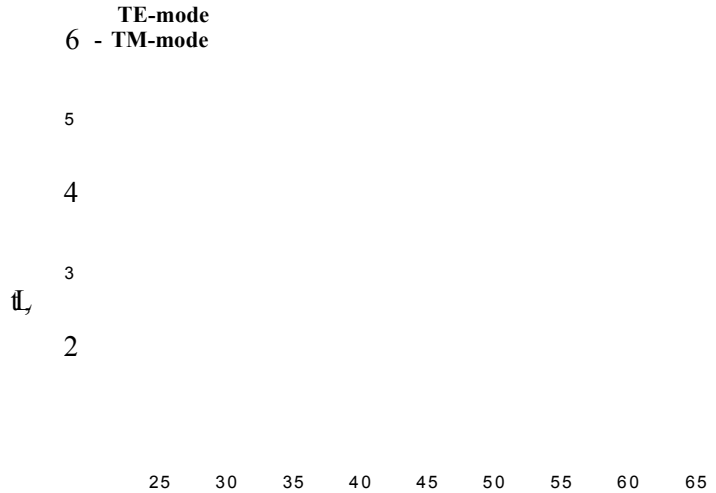

(a)

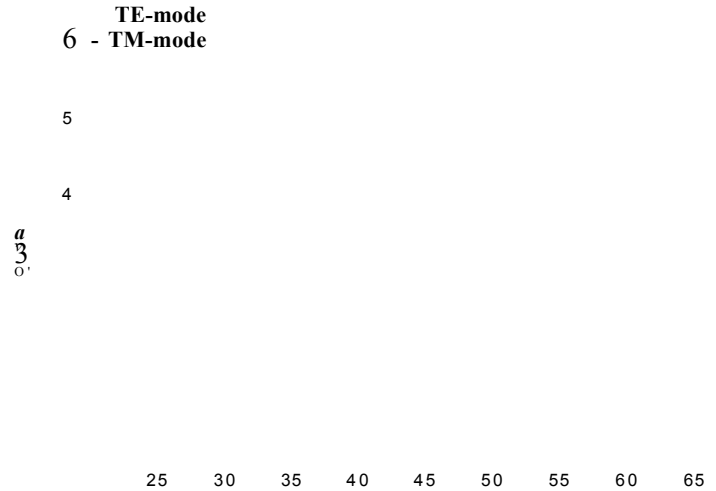

(b

Figure 4-8: Comparison of TE and TM THz valence band polaritons/antipolaritons due to absorption and gain for transition between the first two subbands. The population density differences between the subbands are (a) AN = 1.0x10n cm~2 (b) AN —1.0x10ll cm~2. The dephasing is neglected, 7 = 0.0 meV.

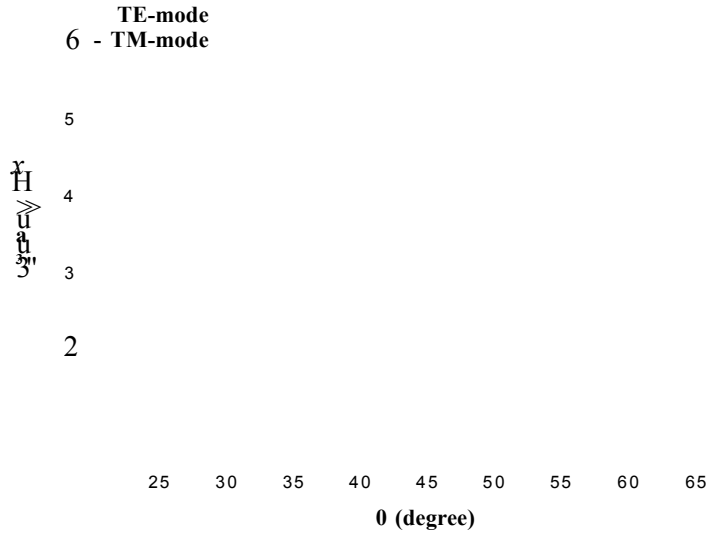

(a)

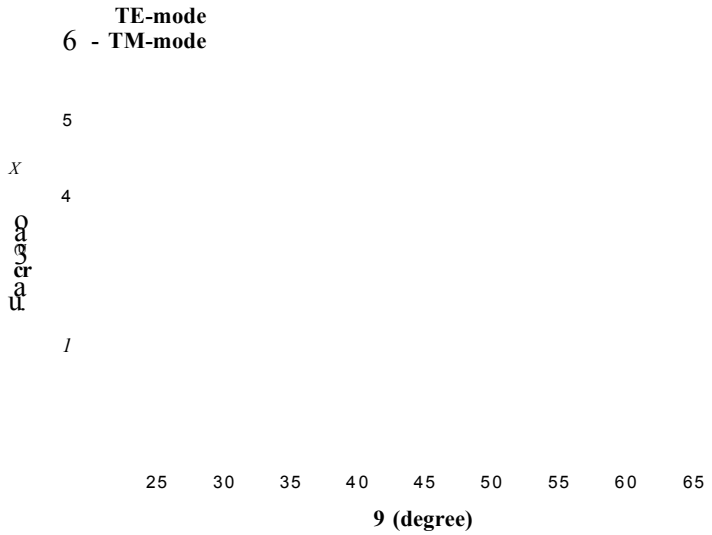

(b)

Figure ^.9: Comparison of TE and TM THz valence band polaritons/antipolaritons due to absortion and gain for transition between the first two subband. The population density differences between the subbands are (a) $\Delta N = 2.0 \times 10^{11}\ cm^{-2}$ *(b)* $\Delta N = -2.0 \times 10^{11}\ cm^{-2}$. *The dephasing is neglected.* $\gamma = 0.0$ *meV.*

We notice from Figures 4.1 to 4.11 that, since the effective resonance frequencies (peak of the susceptibility function) are different, the resonance angle change correspondingly in TE and TM modes. Furthermore, due to the larger oscillator strength of the transition, the polariton and antipolariton splitting are larger in the TM case.

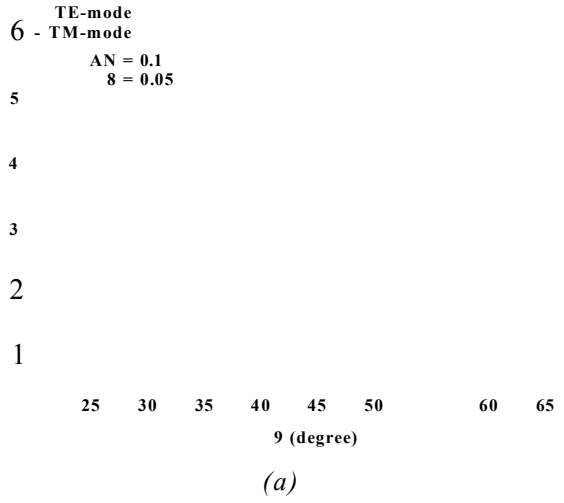

(a)

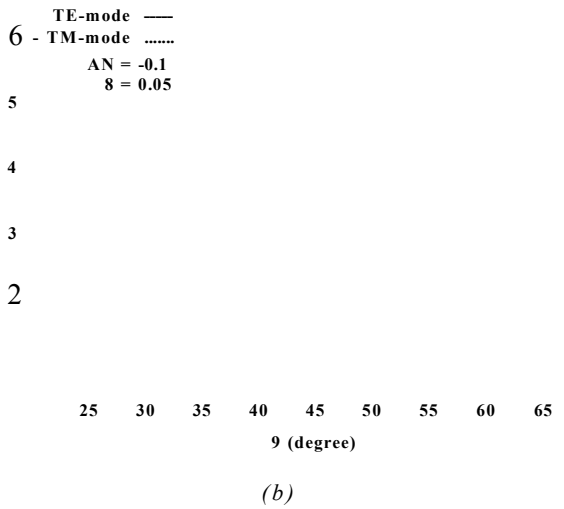

(b)

Figure 4-10: Comparison of TE and TM THz valence band polaritons and antipolaritons due to gain and absorption computed with $AN = 1.0 \times 10^{11}\,cm^{-2}$ *and* $AN = -1.0 \times 10^{11}\,cm^{-2}$. *The dephasing,* $\gamma \approx 0.008$ *THz.*

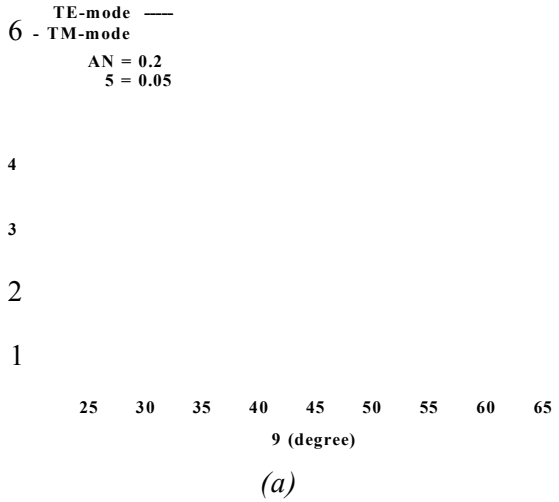

(a)

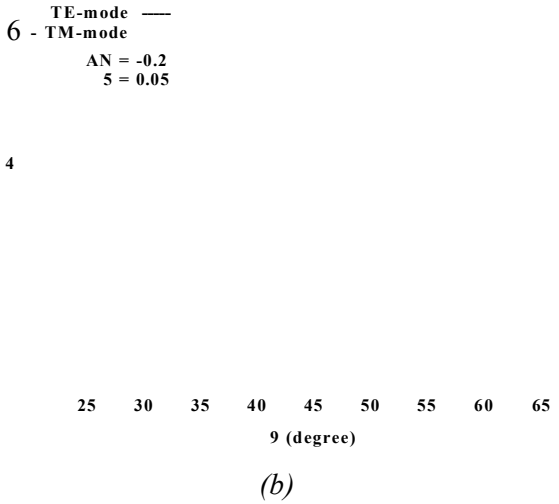

(b)

Figure 11: Comparison of TE and TM THz valence band polaritons/ antipolaritons due to gain and absorption computed with $AN = 2.0 \times 10^{11} cm^{-2}$ *and* $AN = -2.0 \times 10^{n} cm^{-2}$. *The dephasing,* $\gamma \ll 0.008$ *THz.*

4.6 Conclusion

In summary, this chapter described the coupling between TE-mode THz radiation and intervalence band transitions with multiple resonance where transitions are assumed to involve many valence subbands. The energy dispersions relations are derived and plotted. As in the case of a single transition presented in the previous chapter, the effects of dephasing are investigated and furthermore, the influences of

other parameters such as cavity length, barriers width and quantum wells thickness on the polariton dispersions are studied. The combination of non-parabolicity and many body effects were included in the input dielectric constant through the optical susceptibility which resulted from a nonequilibrium Green Function (NEGF).

The interaction of THz cavity modes with intervalence transitions can lead to further improved quantum efficiency of THz-polaritonics devices, even with simplified geometric designs. Moreover, polariton and antipolariton can be obtained for the case of multiple resonance and TE polarization of THz cavity mode which can eventually lead to THz emission normal to the surface. Finally a comparison of TE and TM modes THz polaritons and antipolaritons was presented. Thus, for an easy measurement of polariton and antipolariton based inter-valence band transition, TE-mode polarized cavity is recommeded because the system can be tune to resonance at low frequency compared to TM mode case.

CHAPTER 5
GENERAL CONCLUSION AND FUTURE WORKS

5.1 General conclusion

As a general conclusion, we have investigated the interaction of THz cavity modes with intervalence band excitations. The approach presented was based on the dielectric function formalism where the optical responses used as input was obtained from numerical solutions of many body nonequilibrium Green functions. The resulting optical susceptibility was adjusted using a Lorentzian fit. The dielectric constant and the cavity modes were combined together in a secular equation derived from the wave equation for propagating electric fields in a dielectric medium. The Energy dispersions for the polaritons and antipolaritons were obtained with our equations and applied to a simple geometric structure with $GaAs/Al_{0.3}Ga_{0.7}As$ quantum wells in the cavity core, shielded with AlAs on top and bottom to serve as dielectric mirrors.

$GaAs/Al_{0.3}Ga_{0.7}As$ was chosen because, it is a mature material which has been used in most optoelectronic devices operating in mid and far infrared regions. Thus we applied our theoretical model to this material and considered the THz gap for its potential in device applications. Terahertz devices such as THz emitters and detectors, and THz-quantum cascade lasers are among the successful applications. These devices show great prospects for application in THz imaging, spectroscopic and security screening among others.

In summary, the work presented shows the relevance of valence band based designs for studying the interaction of TE-mode polarized THz radiation and intervalence band transitions in a microcavity resonator based on a simple sample geometry. It paves way for further investigations in quantum electrodynamics and many other physical phenomena. The multiple transition problem leads to interesting scenarios showing repulsion between the different polariton and antipolariton branches leading to improved quantum efficiency of future THz polaritonic and an-

tipolaritons devices where lasing and THz emission may be possible. Moreover the approach allows us to combine predictive microscopic response calculations with a simple dielectric model presented in this thesis for the cavity, leading to a powerful design tool for THz polaritonic/antipolaritonic investigation.

5.2 Future works

We have shown the relevance of valence band based design to the study of the optical interactions of TE-mode THz radiation and intervalence band excitation in a microcavity. It is our hope that future studies on THz polaritonics using intersubband transitions can lead to the successful realization of more efficient, affordable and coherence THz sources.

Further studies will also include calculation of reflection and transmission coefficient for TE and TM modes, for direct comparison with experiment as well as polaritons/antipolaritons in emerging materials such as dilute nitrates, bismides and antimonides. Furthermore, as it was reported in a recent experimental study based on reflectivity measurement, electrical modulation of carrier density can tuned on polaritons states at THz frequency which lead to THz emission [12]. Thus, using a quantum mechanical approach and our simplified model, a simple analytical equation will be derive in the future, to investigate the possibility of THz emission based on intervalence band transition. These can be applied to both single and multiple resonance cases. Finally, electroluminescence experiments with applied bias on the structure will result in the carrier density modulation and controllable electroluminescence spectra can be obtained.

APPENDIX A
ADJUSTING THE MANY BODY NONEQUILIBRIUM SOLUTION INTO A LORENTZIAN FIT

In this appendix we derive a simple formula for adjusting the numerical data of the optical susceptibility obtained using a many body nonequilibrium green's function (NEGF) into a Lorentzian fit. The fitting parameters obtained and the Lorentzian fit with rotating wave approximation (RWA) only and with full (rotating plus non-rotating parts) are compared with the fulll numerical data.

A.1 Using the formula with rotating wave approximation only

The optical susceptibility with the rotating wave part only is given by;

$$\chi(\omega) = -\frac{1}{4\pi}\frac{\Lambda}{\omega - \omega_o + i\delta}, \tag{A.1}$$

where Λ is a dipole coupling term defined in chapter 2, ω_o is the transition frequency and δ is half width at half wave maximum (dephasing term). Separating the optical susceptibility into real and imaginary parts, we have for the imaginary part,

$$\chi''(\omega) = \frac{1}{4\pi}\frac{\Lambda\delta}{(\omega - \omega_o)^2 + \delta^2}. \tag{A.2}$$

Using the schematic diagram for the optical susceptibility shown in Figure A.1, at maximum peak, $\chi'' = \chi''_M$ and $\omega = \omega_o$. Therefore,

$$\chi''(\omega = \omega_o) = \frac{1}{4\pi}\frac{\Lambda}{\delta}. \tag{A.3}$$

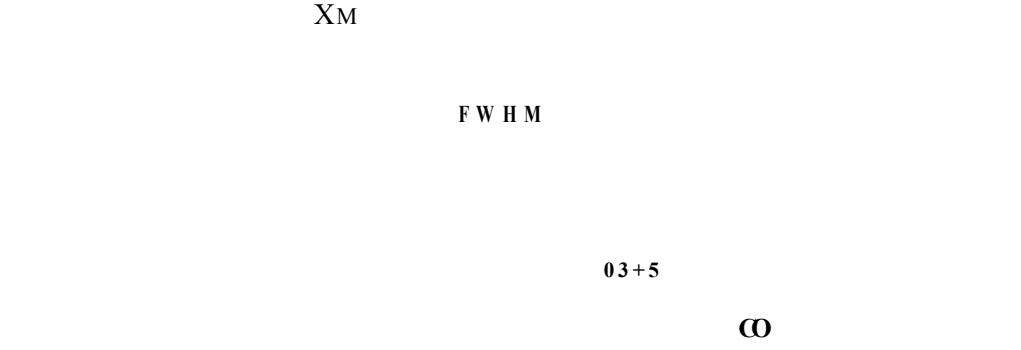

Figure A.1: Schematic diagram showing how the fit parameters are obtained.

Athalf of maximumpeak, $x\ (u) - Xm/2$, then $uo = u0 = F5)$. Here 2 x S is the full widthat half wavemaximum (FHWM). Thus, at $(co = co — <5)$, and using Equation A.2 we have

$$* > = " .- *) = \sim = XM/\wedge \quad \text{(A.4)}$$

with Equation A.3 in Equation A.4, then A can be evaluated as;

$$A = \wedge x\ m8 \quad \text{(A.5)}$$

and the dephasing

$$S = uj0 — uj \quad \text{(A-6)}$$

The values of $_{UJ}$ and $_{UJ0}$ can be read from the data.

A.2 Using full Lorentzin formula

Here we use the full Lorentzian formula for the optical susceptibility (i.e with rotating and counter rotating waves parts) which is given by;

$$\chi(\omega) = \frac{1}{4\pi}\left\{\frac{\Lambda}{\omega - \omega_o + i\delta} - \frac{\Lambda}{\omega + \omega_o + i\delta}\right\}. \tag{A.7}$$

Following the same procedure as in appendix A.1 above, we find the expression for Λ

$$\Lambda = 4\pi\chi''_M\delta\left\{\frac{4\omega_o^2 + \delta^2}{4\omega_o^2}\right\}, \tag{A.8}$$

, where ω_o and δ have their usual configuration as above.

Next, in Figures A.2 and A.3, the imaginary parts of the optical susceptibilities obtained by fitting with RWA (A.1) part only and with full (RWA + NRWA) parts are compared with those generated from the numerical (NEGF) solutions for different densities.

In both Figure A.2 and A.3, (a) and (c) are obtained by Lorentzian fit with RWA part only while (b) and (d) with full Lorentzian (i.e including non rotating part). In both cases, the maximum peak from the optical susceptibility generated with full Lorentzian formula coincide with that obtained with full non-equilibrium green's function (NEGF) calculation. Once more, the full numerical data is not symmetric and the Lorentzian is symmetric, so there is no way to fit at the same time: height, FWHM and the peak position exactly.

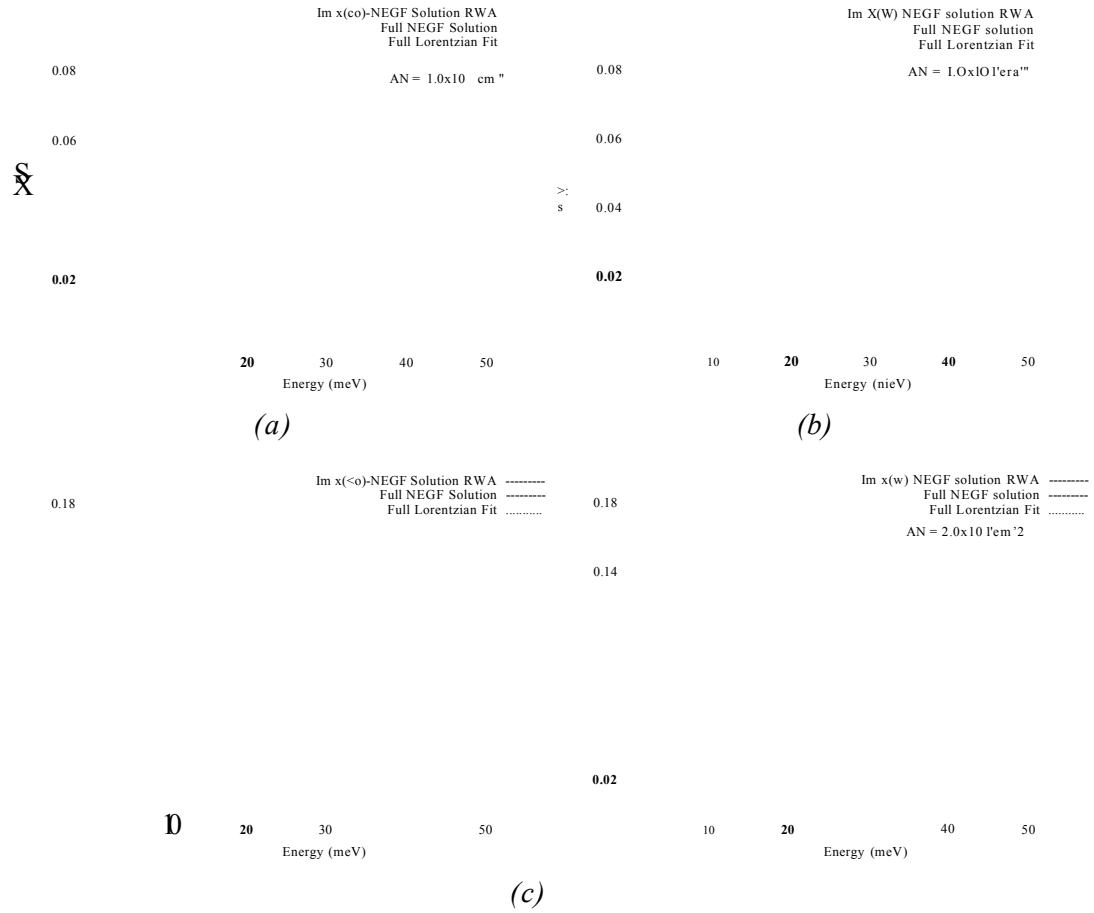

Figure A.2: Imaginary parts of optical susceptibilities from many body nonequilibrium solution (NEGF) compared with Lorentzian fit. (a) and (c) with RWA only, (b) and (d) full (RWA + NRWA) for absorption media with densities as indicated. This shows that, extracting the fitting parameters using the NEGF solution with only the RWA term leads to a better fit to the full NEGF solution, as both figures looked almost the same.

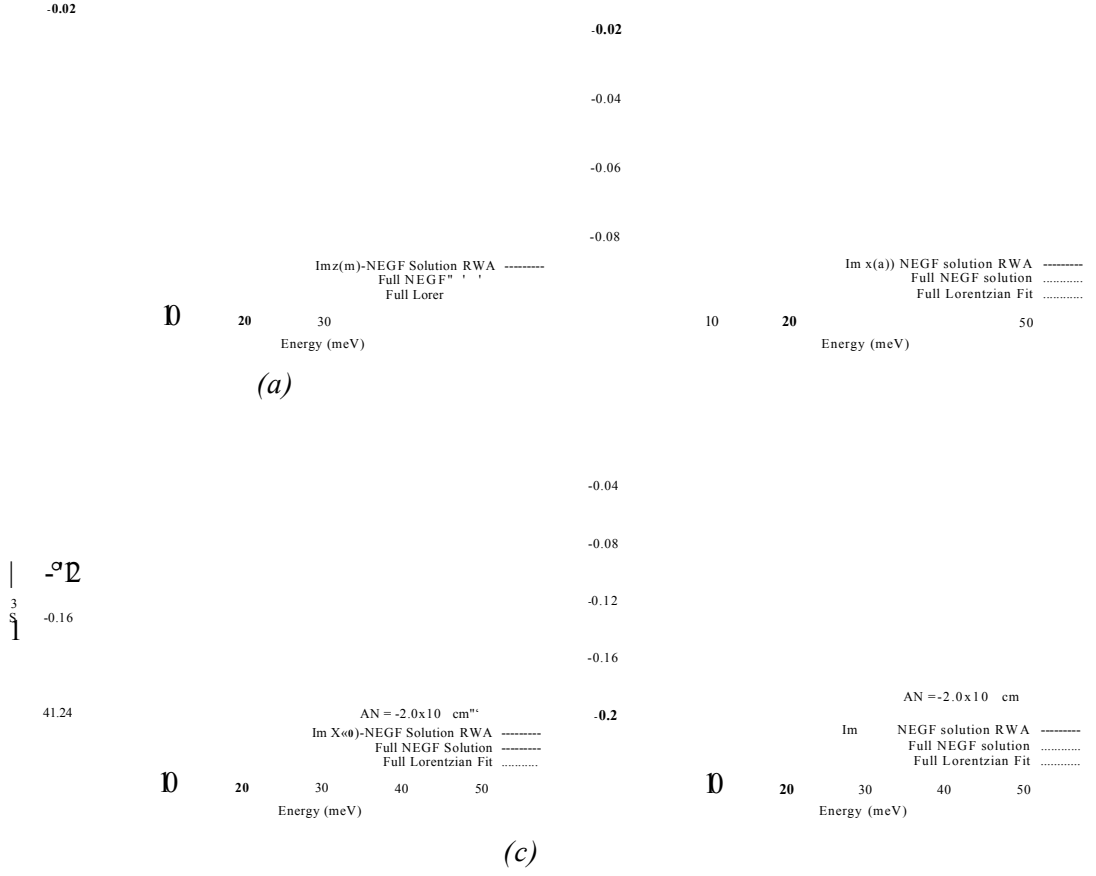

Figure A.3: Imaginary parts of optical susceptibilities from many body nonequilibrium solution (NEGF) compared with Lorentzian fit. (a) and (c) with RWA only, (b) and (d) with full (RWA + NRWA) for gain media with densities as indicated. This shows that, extracting the fitting parameters using the NEGF solution with only the RWA term leads to a better fit to the full NEGF solution, as both figure looked almost the same.

REFERENCES

[1] S Haroche and D. Kleppner, Cavity quantum electrodynamics, Phys. Today **42**, No. 1 24 (1989).

[2] D Dini, R Köhler, A Tredicucci, G Biasiol and L Sorber, Microcavity polaritons splitting of intersubband transitions, Phys. Rev. Lett. **90**, 116401 (2003).

[3] S Zanotto, G Biasol, R Degl'Innocenti L Sorber and A Tredicuccci, Intersubband polaritons in one dimensional plasmon photonic crystal, App. Phys. Lett. **97**, 231123 (2010).

[4] R Colombelli, C Ciuti, Y Chassagneux and C Sirtonic, Quantum cascade intersubband polariton light emitters, IOP-Publishing, semiconductor sci. Technology **20**, pp. 985-990 (2005).

[5] M F Pereira Jr, Intersubband antipolaritons: Microscopic approach, Phys. Rev. B **75**, 195301 (2007).

[6] M F Pereira, Intersubband vs interband light coupling in semiconductors, Opt. Quant. Electron., springer Vol. **40**, pp. 325-329 (2008).

[7] F Capassor. et al, Quantum cascade lasers: ultrahigh-speed operations, optical wireless communication, narrow linewidth, and far-infrared emission, IEEE J. Quantum Electron. **38**, 511 (2002).

[8] M I Amanti, A Bismuto, M Beck, L Isa, K. Kumar, E. Reimhult and J. Faist, Electrically driven nanopillars for THz quantum cascade lasers, Optics Express 10917, Vol. **21**, No. 9 (2013). DOI:10.1364/OE.21.010917.

[9] H C Liu, Quantum well infrared photodetectors, Intersubband transitions in Quantum Wells: Physics and Device applications 1 (semiconductor and semimetals vol 62) ed H C Liu and F Capasso (San Diego: Academic), P 126 (2000).

[10] S D Gunapala, S V Bandara, J K Liu, J M Mumolo, S B Rafol and D Z Ting, Quantum Well Infrared Photodetector Technology and Applications, IEEE J. of Selected Topics in Quant. Electron., Vol. **20**, NO. 6, 3802312, Nov./Dec. 2014 .

[11] M Geiser, G Scalari, F Castellano, M Beck and J Faist, Room temperature THz polariton emitter, Appl. Phys. Lett. **101**, 141118 (2012).

[12] M Geiser, M Beck, and J Faist, Terahertz intersubband polariton tuning by electrical gating, Optics Express, 2126, Vol. **22**, No. 2 Jan. 27, (2014). DOI:10.1364/OE.22.002126 .

[13] J Faist, F Capasso, D L Sivco, C Sirtori, A L Hutchinson, and A Y Cho " Quantum Cascade Laser", Science **264** (5158), 553-556, (1994).

[14] S Kumar, Recent Progress in Terahertz Quantum Cascade Lasers, IEEE J. of Selected Topics in Quant. Electro., Vol **17**, NO. 1, (2011).

[15] Köhler, R. et al. Terahertz semiconductor-heterostructure laser, Nature **417**, 156-159, (2002).

[16] B S Williams, Terahertz quantum cascade lasers, Nature photonics Vol. **1**, sept. 2007.

[17] V Bergert, Three level laser based on intersubband transitions in asymmetric quantum wells: a theoretical study, Sem. Sci. Tech., **9**, 1493-1499 (1994).

[18] C Sirtori, P Kruck, S Barbeiri, P Collot, J Nagle, M Beck, J Faist, and U Oesterle, GaAs/$Al_xGa_{1-x}As$ quantum cascade lasers, Appl. Phys. Lett. Vol. **73**, No. 24 (1998).

[19] G Scalari, M I Amanti, M Fischer, R Terazzi, C Walther, M Beck, and J Faist, Step well quantum cascade laser emitting at 3 THz, Appl. Phys. Lett., **94**, pp. 041114-1 - 041114-3, 2009.

[20] S Kumar, C W I Chan, Q Hu, and J L Reno, Two-well terahertz quantum-cascade laser with direct intrawell-phonon depopulation, Appl. Phys. Lett., **95**, pp. 141110-1 - 141110-3, 2009.

[21] T Liu, K E Lee, and Q J Wang, Microscopic density matrix model for optical gain of terahertz quantum cascade lasers: Many-body, nonparabolicity, and resonant tunneling effects, Phys. Rev. B **86**, 235306 (2012).

[22] H C Liu, C Y Song, A J SpringThorpe, et. al., Terahertz quantum-well photodetector, Appl. Phys. Lett., **84**, 4068 (2004).

[23] H C Liu, H Luo, C Y Song, et. al.,Terahertz Quantum Well Photodetectors, IEEE J. Select. Topics in Quant. Electron., **14**, 374 (2008).

[24] M Geiser, C Walther, G Scalari M Beck, M Fischer, L Nevou and J Faist, Strong light-matter coupling at terahertz frequencies at room temperature in electronic LC resonators, Appl. Phys. Lett. **97**, 191107 (2010).

[25] R Zhang, X G Guo, and J C Cao, Optical couplers for terahertz quantum well photodetectors, Terahertz Science and Technology, ISSN 1941-7411, Vol. **7**, No. 1 March 2014.

[26] K Ohtani, M Fischer, G Scalari, M Beck, and J Faist, Terahertz intersubband electroluminescence from InAs quantum cascade light emitting structures, Appl. Phys. Lett. **102**, 141113 (2013).

[27] F Sizov and A Rogalski, THz Detectors, Prog. in Quantum Electronics, **34**, (2010) 278-347.

[28] S Foteinopoulou, M Kafesaki, E N Economou and C M Soukoulis, Two dimensional polaritonic photonic crystals at terahertz uniaxial metamaterials, Phys. Rev. B **84**, 035128 (2011).

[29] M F Pereira Jr, Microscopic approach for intersubband-based thermovoltaic structures in the THz and Mid Infrared, JOSA B Vol. **28**, Iss. 8 2014 (2011).

[30] H Tao, E A Kadlee, A C Strikwerda, K Fan, W J Padilla, R D Averitt, E A Shaner and X Zhang, Microwave and terahertz wave sensing with metamaterials. Opt. Express Vol. **19** No. 22, 2162021626 (2011).

[31] W Kuehn et al. Two-color two-dimensional terahertz spectroscopy on intersubband transitions of coupled quantum wells. Optics Express, Quantum electronics and laser science conference paper. QFG3, 2010.

[32] Y Todorov et al., Polaritonic spectroscopy of intersubband transitions. Phys. Rev. B **86**, 125314 (2012).

[33] D Dragoman and M Dragoman, Terahertz fields and applications, Prog. in Quantum Electronics,**28**, (2004) 1-66.

[34] I A Faragai and M F Pereira, interactions of valence band excitations and terahertz TE-polarized cavity modes, Opt.and Quantum Electron. Vol. **46**, No. 4 527-531 (2014).

[35] M F Pereira Jr and I A Faragai, Coupling of THz radiation with intervalence band transitions in microcavities, Optics Express 3439 Vol. **22**, No. 3 (2014).

[36] http://www.britannica.com/EBchecked/topic/183228/electromagnetic-radiation/59190/The-electromagnetic-spectrum?anchor=ref273240.

[37] B S Williams, Terahertz quantum cascade lasers, Nature photonics Vol. **1**, sept. 2007.

[38] Q Y Lu, N Bandyopadhyay, S Slivken, Y Bai, and M Razeghi, Room temperature terahertz quantum cascade laser sources with 215 μW output power through epilayer-down mounting, Appl. Phys. Lett. **103**, 011101 (2013).

[39] P H Siegel, Terahertz technology, IEEE Trans. Microwave Theory and Tech., **50**, 910928 (2002).

[40] A Rogalski and F Sizov, Terahertz detectors and focal plane arrays, Opto-Electron. Rev., **19**, no. 3 (2011).

[41] M Tonouchi, Cutting-edge terahertz technology, Nature Photon **1**, 97105 (2007).

[42] Y-C Shen, P F Taday, D A Newnham, M C Kemp, and M Pepper, 3D chemical mapping using terahertz pulsed imaging, Terahertz and gigahertz electr. and photonics IV, Proceeding of SPIE, Vol. **5727** (2005).

[43] B Ferguson, and X-C Zhang, Materials for terahertz science and technology, Nature Mater, **1** 2633 (2002).

[44] D Mittleman, Sensing wit Terahertz Radiation, Springer, Berlin (2003).

[45] E R Mueller, Terahertz Radiation Source for Imaging and Sensing applications (Source: www.coherent.com) .

[46] http://www.homelandsecuritynewswire.com/njit-physicist-terahertz-imaging-ultimate-defense-against-terrorism.

[47] K Ishigaki, M Shiraishi, S Suzuki, M Asada, N Nishiyama and S Arai, Direct intensity modulation and wireless data transmission characteristics of terahertz-oscillating resonant tunnelling diodes, IEEE, Elect. Lett. Vol. **48**, No. 10 (2012).

[48] G Pavlovic, Exciton-polaritons in low dimensional structures, PhD thesis (2010).

[49] T Katsuyama, T Sato, Y Yammamoto and N Sagawa, Superlattices and Microstructures, Vol. **20**, No. 1 (1996).

[50] H Deng, H Haug and Y Yamamoto, Exciton-polariton Bose-Einstein condensation, Rev. Mod. Phys., Vol. **82**, No. 2 April/June (2010).

[51] D Bajoni, Corrigendum: Polariton lasers. Hybrid lightmatter lasers without inversion, J. Phys. D: Appl. Phys. **45**, 409501 (2012).

[52] A Liu, Rabi splitting of the optical intersubband absorption line of multiple quantum wells inside a Fabry-Perot microcavity, Phys. Rev. B **55**, No. 11 pp. 7101-7109, (1997).

[53] M F Pereira, Influence of dephasing in the coupling of light with intersubband transitions, Microelectronic Journal **40**, 841-843 (2009).

[54] M O Manasreh, Introduction to Nanomaterials and Devices 1st edition, J Wiley and Sons Inc., pp-202 (2012).

[55] C Weisbuch and B Vinter, Quantum semiconductor structures: Fundamental and Applications, Academic Press, (1991).

[56] M O Manasreh, Optoelectronic properties of semiconductors and superlattices, Vol. 6: Long wavelength infrared emitters based on quantum wells and superlattices, Gordon and Breach Science Publishers (2000).

[57] R Q Yang, Optical Intersubband transitions in conduction-band quantum wells, Phys. Rev. B Vol. **52**, No. 16, p 11958 - 11968, (1995).

[58] H C Liu, M Buchahan and R Z Wasilewski, How good is the polarization selection rule for intersubband transitions, Appl. Phys. Lett., Vol. **72**, No. 14, p 1682 - 1684, (1998).

[59] M F Pereira, Many body theory of THz intervalence gain in quantum wells, Opt. and Quant Electron, Vol. **40**, No. 14-15, pp. 10911095 (2008).

[60] M I Hossain, Z Ikonic, J Watson, J Shao, P Harrison, M J Manfra and O Malis, Strong heavy-to-light hole intersubband absortions in the valence band of carbon-doped GaAs/AlAs superlattices, J. Appl. Phys. **113**, 053103 (2013).

[61] H C Liu and F capasso, Intersubband transition in quantum wells, Physics and Device Application I and II, Vol. **62** and **86**, Academic Press (2000).

[62] A Harwit, Effect of electric fields on quantum well intersubband transition, PhD thesis, Stanford University, (1987.)

[63] H Haug and S W Koch, Quantum Theory of the Optical and Electronic Properties of semiconductors, Fourth Ed., World Scientific (2004).

[64] J Singh, Physics of semiconductors and their Heterostructures (McGraw-Hill, New York, (1993).

[65] U Rössler, Band-Offset and Effective-Mass Parameters in Quantum wells, Solid State communication, Vol. **65**, No.11, pp. 1279-1280 (1988).

[66] M Fox and R Ispasoiu, Quantum wells, Superlattices and Band Gap Engineering, Springer Handbook of Electronic and Photonic Materials, pp. 1021-1040 (2007).

[67] M Shen and W Cao, Electronic band-structure engineering of $GaAs/Al_xGa_{1-x}As$ quantum well superlattices with substructures, Elsevier; Materials and Engineering B **103**, pp. 122-127 (2003).

[68] M F Pereira, Jr., S C Lee and A wacker, Controlling many body effect in the midinfrared gain and terahertz absorption of quantum cascade lasers, Phys. Rev. B **69**, 205310 (2004).

[69] D Jena, k.p theory of semiconductors, EE 698D, Advanced Semiconductor Physics. (2004).

[70] R Eppenga, M F H Schuurmans, and S Colak, New k.p theory for $GaAs/Ga_{1-x}Al_xAs$-type quantum wells, Phys. Rev. B **36** 1554 (1987).

[71] T E Ostramek, Evaluation of matrix elements of the 8×8 k·p Hamiltonian with k-dependant spin-orbit contribution for zinc-blended structure og GaAs, Phys. Rev. B **54**, pp. 467-479 (1996).

[72] L C Lew yan Voon and M Willatzen, The k.p method: Electronic properties of semiconductors, ISBN 978-3-540-92871-3, Springer (2009).

[73] L Sirigu, R Terazzi, Maria. I. Amanti, Marcella Giovannini and J Faist, Terahertz Quantum Cascade Lasers based on two-dimensional photonic crystal resonators, Optics Express 5206, Vol. **16**, No. 8, April (2008).

[74] Y.-F Lao and A G Unil Perera, dielectric function model for p-type semiconductor intervalence band transitions, J. Appl. Phys. **109**, 103528 (2011).

[75] T Schmielau and M F Pereira, A dielectric theory for the coupling of light with multiples intersubband transitions, Journal of OPt-Electronics and advance materials Vol. **10**, NO. 1, pp. 55-57 Jan. (2008).

[76] I A Faragai and M F Pereira, Interaction of valence band excitations and teraherz TE-polarized cavity modes, Opt. and Quant. Electron. **46** pp. 527-531 (2014).

[77] D Dini, R Köhler, A Tredicucci, G Biasiol and L Sorber, Microcavity polaritons splitting of intersubband transitions, Phys. Rev. Lett. **90** 116401 (2003).

[78] S Zanotto, G Biasol, R Degl'Innocenti L Sorber and A Tredicuccci, Intersubband polaritons in one dimensional plasmon photonic crystal, App. Phys. Lett. **97** 231123 (2010).

[79] M F Pereira and S Tomić, Intersubband gain without global inversion through dilute nitride band engineering, Appl. Phys. Lett. **98**, 061101 (2011).

[80] M F Pereira, Intersubband vs interband light coupling in semiconductors, Optt. Quant. Electron, springer Vol. **40**, pp. 325-329 (2008).

[81] W W Chow, M.F. Pereira Jr., and S W Koch, Many-Body Treatment on the Modulation Response in a Strained Quantum Well Semiconductor Laser Medium, Appl. Phys. Lett. **61**, 758 (1992).

[82] M F Pereira Jr., Analytical solutions for the optical absorption of superlattices. Phys. Rev. B **52**, pp. 19781983 (1995).

[83] M F Pereira Jr, Intersubband antipolaritons: Microscopic approach, Phys. Rev. B **75**, 195301 (2007).

[84] M F Pereira, Jr. and H. Wenzel, Interplay of Coulomb and nonparabolicity effects in the intersubband absorption of electrons and holes in quantum wells, Phys. Rev. B **70**, 205331 (2004).

[85] M F Pereira, Jr., Intervalence transverse-electric mode terahertz lasing without population inversion, Phys. Rev. B **78**, 245305 (2008).

[86] M S Vitiello, R C Iotti, F Rossi, L Mahler, A Tredicucci, H E Beere, D A Ritchie, Q Hu, and G Scamarcio, Non-equilibrium longitudinal and transverse optical phonons in terahertz quantum cascade lasers, Appl. Phys. Lett. **100**, 091101 (2012).

[87] A Wacker, Semiconductor Superlattices: A model system for nonlinear transport, Phys. Rept. Vol. **357**, No. 1 pp. 1 - 111 (2002).

[88] T Schmielau and M F Pereira, Jr., Nonequilibrium many body theory for quantum transport in terahertz quantum cascade lasers, Appl. Phys. Lett. **95**, 231111 (2009).

[89] T Schmielau and M.F. Pereira Jr, Impact of momentum dependent matrix elements on scattering effects in quantum cascade lasers, Phys. Status Solidi B **246**, 329 (2009).

[90] M F Pereira and I A Faragai, Coupling of THz radiation with intervalence band transitions in microcavities, Opt. Express, Vol.**22**, No. 3 pp. 3439-3446 (2014).

[91] S Adachi, GaAs, AlAs, and $Al_xGa_{1-x}As$: material parameters for use in research and device applications, Journal of App. Phys., **58** (3), 1 August (1985).

[92] A Quattropani and W Czaja, Quantum theory of exciton-polariton with spatial dispersion, Physica Scripta. Vol. **T29** 162-166, (1989).

[93] M F Pereira, the influence of dephasing in the coupling of light with intersubband transitions, Microelectronics Journal **40** pp. 841843 (2009).

[94] M F Pereira Jr and I A Faragai, Coupling of THz radiations with intervalence band transitions in microcavities, Optics Express Vol.**22**, No. 3 pp. 3439-3446 (2014).

[95] A Naesby, T Suhr, P T Kristensen, and J Mork, Influence of pure dephasing on emmision spectra from single photon sources, Phys. Rev. A **78**, 045802 (2008).

[96] R Colombelli, C Ciuti, Y Chassagneux and C Sirtori, quantum cascade intersubband polariton light emmiters, IOP-publishing, J. of semicond. Sci. Technol. **20**, 985-990 (2005).

[97] A Laucht, N Hauke, J M Villas-Bôas, F Hofbauer, G Böhm, M Kaniber, and J J Finley, dephasing of excion polaritons in photoexcited InGaAs quantum dots in GaAs nanocavities, Phys. Rev. Lett. **103** 087405 (2009).

[98] M F Pereira Jr. and H Wenzel, Interplay of Coulomb and nonparabolicity effects in the intersubband absorption of electrons and holes in quantum wells, Phys. Rev. B **70** 205331 (2004).

[99] M F Pereira, The influence of dephasing in the coupling of light with intersubband transitions, Microelectronics journal **40** 841-843 (2009).

[100] C Weisbuch, M Nishioka, A Ishikawa and Y Arakawa, Observation of the coupled Exciton-Photon Mode splitting in a Semiconductor Quantum Microcavity, Phys. Rev. **69** No. 23 (1992).

[101] R Köhler, Rita C lotti, A Treddicucci and F Rossi, Design and simulation of terahertz quantum cascade lasers, App. Phys. Letts. Vol. **79** No. 24 (2001).

[102] S De Liberato, C ciuti and Chris C Phillips, Terahertz lasing from intersubband polariton-polariton scattering in asymmetric quantum wells, Phys. Rev. **87** 241304 (R) (2013).

[103] H Luo, S R Laframboise, Z R Wasilewski, G C Aers,H C Liu and J C Cao, Terahertz quantum cascade lasers based on a three-well active module, Appl. Phys. Lett. **90**, 041112 (2007).

[104] J Faist, Intersubband optoelectronics, ETH Zurich, Zürich, Sept. 17, (2009).

[105] M F Pereira Jr, R Nelander, A Wacker, D G Revin, M R Soulby, L R Wilson, J W Cockburn, A B Krysa, J S Roberts, and R J Airey, Characterization of Intersubband Devices Combining a Nonequilibrium Many Body Theory with Transmission Spectroscopy Experiments, Journal of Materials Science: Materials in Electronics **18**, 689 (2007).

[106] M F Pereira, The influence of dephasing in the coupling of light with intersubband transitions, Microelectronics Journal **40**, 841 (2009) .

[107] M F Pereira, Jr., S C Lee and A Wacker, Controlling many body effect in the midinfrared gain and terahertz absorption of quantum cascade laser structures, Phys. Rev. B **69**, 205310 (2004) .

[108] M F Pereira, Jr., S C Lee and A Wacker, Effects of coulom corrections and mean field on gain and absorption in quantum cascade lasers, Phys. Stat. sol. (c) **2**, 3027 (2005) .

[109] H C Liu, Intersubband transitions in quantum wells: Physics and device applications I, semeconductor and semimetal. Vol. **62**, Academic Press, (2000).

[110] V B Verma, V C Elarde and J J Coleman, Physics and Applications of Intersubband Transitions in Patterned Inverse Quantum Dot Arrays, IEE Lasers and Electro-Optics society, LEOS 21^{st} annual meeting proceeding, (2008).